
**First measurement of
the $t\bar{t}$ production cross section
in association with a Z boson
decaying into a quark pair
at the CMS Experiment**

Dissertation

ZUR ERLANGUNG DES DOKTORGRADES AN DER FAKULTÄT
FÜR MATHEMATIK, INFORMATIK UND NATURWISSENSCHAFTEN
FACHBEREICH PHYSIK
DER UNIVERSITÄT HAMBURG

vorgelegt von

Valerie Scheurer

aus

Oberhausen-Rheinhausen, Deutschland

Hamburg

2022

Eidesstattliche Versicherung / Declaration on oath

Hiermit versichere ich an Eides statt, dass ich die vorliegende Dissertationsschrift selbst verfasst und keine anderen als die angegebenen Hilfsmittel und Quellen benutzt habe.

Ich versichere, dass dieses gebundene Exemplar der Dissertation und das in elektronischer Form eingereichte Dissertationsexemplar (über den Docata-Upload) und das bei der Fakultät (zuständiges Studienbüro bzw. Promotionsbüro Physik) zur Archivierung eingereichte gedruckte gebundene Exemplar der Dissertationsschrift identisch sind.

Ich versichere, dass ich keine Dissertation mit dem gleichen Forschungsthema schon einmal in einem früheren Promotionsverfahren an einer wissenschaftlichen Hochschule eingereicht habe, die angenommen oder als ungenügend beurteilt worden ist.

I hereby declare, on oath, that I have written the present dissertation by my own and have not used any resources and aids other than those acknowledged.

I, the undersigned, declare that this bound copy of the dissertation and the dissertation submitted in electronic form (via the Docata upload) and the printed bound copy of the dissertation submitted to the faculty (responsible Academic Office or the Doctoral Office Physics) for archiving are identical.

I, the undersigned, hereby declare that I have not submitted a dissertation with the same research topic to an academic higher education institution that had been already accepted or evaluated as insufficient in an earlier doctoral procedure.

Hamburg, 27. Juli 2022

Valerie Scheurer

Gutachter der Dissertation:	Dr. Andreas Meyer
	Prof. Dr. Johannes Haller
Zusammensetzung der Prüfungskommission:	Prof. Dr. Sven-Olaf Moch
	Prof. Dr. Johannes Haller
	Dr. Andreas Meyer
	Prof. Dr. Elisabetta Gallo
	Dr. Maria Aldaya
Vorsitzender der Prüfungskommission:	Prof. Dr. Sven-Olaf Moch
Datum der Disputation:	13.09.2022
Vorsitzender des Fach-Promotionsausschusses Physik:	Prof. Dr. Wolfgang J. Parak
Leiter des Fachbereichs Physik:	Prof. Dr. Günter H. W. Sigl
Dekan der Fakultät MIN:	Prof. Dr. Norbert Ritter

ABSTRACT

In this thesis, data collected by the CMS Experiment at the CERN LHC is analysed. The data was collected during LHC Run 2 in the years 2016-2018 and corresponds to an integrated luminosity of 138 fb^{-1} . Using this data, the cross section of top quark pair production ($t\bar{t}$) in association with a Z boson is measured. The process is analysed for the first time in the decay channel with the $t\bar{t}$ pair decaying dileptonically and the Z boson decaying hadronically. Only Z bosons with a transverse momentum greater than 200 GeV are considered. In this regime, the two jets from the Z boson form one single boosted jet that is used to identify the Z boson. The cross section is measured to be $\sigma_{t\bar{t}Z_{\text{incl.}}} = 710^{+327}_{-299} \text{ fb}$.

In addition, the calibration of the BCM1F detector, one of the luminosity measurement systems of the CMS Experiment, is shown. In order to calibrate the measurement, several corrections are developed and applied. For the luminosity measurement for the year 2018, the ratio with respect to nominally the best luminosity ranges between 1 and 1.02 after the corrections are applied.

ZUSAMMENFASSUNG

In dieser Arbeit werden Daten analysiert, die vom CMS Experiment am LHC am CERN gesammelt wurden. Die Daten wurden während LHC Run 2 in den Jahren 2016-2018 gesammelt und entsprechen einer integrierten Luminosität von 138 fb^{-1} . Anhand dieser Daten wird der Wirkungsquerschnitt von Top-Quark-Paarproduktion ($t\bar{t}$) in Assoziation mit einem Z-Boson gemessen. Der analysierte Zerfallskanal enthält ein dileptonisch zerfallendes $t\bar{t}$ Paar, sowie ein hadronisch zerfallendes Z-Boson. Es werden nur Z-Bosonen mit einem Transversalimpuls größer als 200 GeV betrachtet. In diesem Regime bilden die beiden Jets des Z-Bosons einen einzigen geboosteten Jet, der zur Identifizierung des Z-Bosons verwendet wird. Der gemessene Wirkungsquerschnitt beträgt $\sigma_{t\bar{t}Z_{\text{incl.}}} = 710^{+327}_{-299} \text{ fb}$. Darüber hinaus wird die Kalibrierung des BCM1F-Detektors, eines der Luminositätsmesssysteme des CMS Experiments, gezeigt. Um die Messung zu kalibrieren, werden mehrere Korrekturen entwickelt und angewendet. Bei der Luminositätsmessung für das Jahr 2018 liegt das Verhältnis zur nominell besten Luminosität nach Anwendung der Korrekturen zwischen 1 und 1,02.

CONTENTS

1	Introduction	1
I	Theoretical and Experimental Basis	3
2	Theoretical Introduction	5
2.1	The Standard Model of Particle Physics	5
2.1.1	The Electroweak Interaction	7
2.1.2	The Strong Interaction	13
2.2	The Z Boson	14
2.3	The Top Quark	15
2.4	The $t\bar{t}Z$ Production Process	18
3	Experimental Setup	23
3.1	The Large Hadron Collider	23
3.2	Luminosity	26
3.2.1	Measurement of Luminosity	27
3.3	The CMS Experiment	28
3.3.1	Coordinate System	28
3.3.2	Detector Setup	31
3.4	Luminosity Detectors	34
3.4.1	BCM1F	36
4	Reconstruction Algorithms	41
4.1	Tracks and Vertices	41
4.2	Particle-flow	43
4.3	Jet Reconstruction	43
4.3.1	b tagging	46
4.3.2	Boosted jets	48
4.3.3	Boosted Jet Tagging	49
4.4	Lepton Identification	51
4.4.1	Electrons	51
4.4.2	Muons	54
4.5	Missing Transverse Momentum	56

4.6	Event Shape Variables	56
II	Luminosity Studies	59
5	Calibration of the BCM1F detector	61
5.1	Measurement of Instantaneous Luminosity with BCM1F	62
5.2	Corrections for Non-linear Response	63
5.2.1	Non-linearity in 2018	64
5.2.2	Dependency of the non-linearity correction on the number of bunches in a fill	66
5.2.3	Correction on the Van der Meer Scan measurement	70
5.2.4	Non-linearity in 2017	71
5.3	Radiation Damage and Annealing Effects	74
5.4	Final Calibration	76
III	Measurement of the $t\bar{t}Z$ Cross Section	81
6	Introduction	83
6.1	Motivation and Previous Results	84
6.2	Analysis Strategy	85
7	Definition of the Signal Region	89
7.1	Particles and Objects	89
7.1.1	Leptons	89
7.1.2	Jets	90
7.1.3	Boosted jets	90
7.2	Event Selection	91
7.2.1	Trigger selection	91
7.2.2	Leptons	92
7.2.3	Jets and b jets	92
7.2.4	Boosted jets	93
8	Processes and Simulated Samples	95
8.1	The Signal Process $t\bar{t}Z \rightarrow q\bar{q}$	95
8.2	Top Quark Pair Production	96
8.3	Other Top Quark Pair Processes	97
8.4	Other Backgrounds	98
8.4.1	The Drell-Yan process	98
8.4.2	Single top quark production	99
8.4.3	Diboson production	99

9	Classification with a Deep Neural Network	101
9.1	Training Samples	102
9.2	Input Variables	103
9.3	Hyperparameter Optimisation	112
9.4	Training Results	115
10	Systematic Uncertainties	119
10.1	Theoretical Uncertainties	119
10.2	Experimental Uncertainties	122
10.2.1	Trigger efficiency	122
10.2.2	Luminosity uncertainty	122
10.2.3	Scale factor uncertainties	122
10.2.4	Jet energy corrections	123
11	Comparison of Data and Simulation	127
11.1	Data Recorded in 2017 and 2018	127
11.2	Data Recorded in the First Part of 2016	128
11.3	Data Recorded in the Second Part of 2016	129
11.4	The Full Run 2 Dataset	131
12	Optimisation Studies using Simulated Events	135
12.1	Choice of the Minimum Transverse Momentum	135
12.2	Minimum Mass of the Boosted Jet	136
12.3	Categorisation	137
13	Results	141
13.1	Maximum Likelihood Fit	141
13.2	Impacts of Uncertainties	141
13.3	Cross Section Measurement	143
14	Outlook	149
15	Summary	151
	Bibliography	153

The standard model of particle physics is today's most successful theory of high energy physics. Based on gauge invariant quantum field theory, it can explain three out of the four known fundamental forces of nature – electromagnetism as well as the weak and the strong forces.

The standard model has been experimentally verified to describe nature in detail at energies that are accessible in experiments. The discovery of the W and Z bosons at the SPS collider [1], the precise measurement of the parameters of the CKM matrix at the b-factories (e.g. [2]) or the discovery of the Higgs boson at the LHC [3] are only three of many important successful verifications of standard model predictions.

However, many questions remain unanswered. The nature of dark matter, the origin of gravity or the connection between the quark and lepton sectors are just a small selection of the many unknowns. All of these shortcomings show, that the standard model cannot be the final answer, but simply a low-energy approximation to a more comprehensive theory.

One way of probing for this unknown law of nature is to search for small discrepancies between theoretical calculations and the experimental measurement in standard model processes at high energies.

The main topic of this thesis is one such measurement. The cross section of the $t\bar{t}Z$ process – where a top quark antiquark pair is produced in association with a Z boson – is measured using hadronically decaying Z bosons with a transverse momentum above 200 GeV. In this high phase space of high Z boson transverse momenta, possible deviations from the standard model are expected to be largest.

Physics analyses such as the one presented here would not be possible without the highly sophisticated contemporary particle physics experiments. The construction, operation and calibration of these systems make up a large and important part of the field of experimental particle physics. One of the many experimental tasks is the measurement of luminosity. Luminosity is a measure of the number of collisions in a collider – without knowledge of it, no cross section measurement could be performed.

In the CMS Experiment, the luminosity is measured using several independent systems.

One of these is the BCM1F detector, the calibration of which was done in the scope of this thesis.

The thesis consists of three parts. In part I, the theoretical and experimental basis is set, with a theoretical overview in chapter 2, a description of the CMS experiment, the measurement of luminosity and luminosity detectors in chapter 3, and an introduction to important analysis algorithms in CMS in chapter 4.

Part II focuses on the luminosity measurement, with the calibration of the BCM1F detector shown in chapter 5.

In part III, the main analysis of the thesis is shown. In chapter 6, the motivation for the measurement is discussed and previous measurements are presented. The definition of the signal region is explained in chapter 7. Chapter 8 discusses the most important background processes for the measurement. In chapter 9, the development of a deep neural network is shown. Using the events in the signal region, the network is trained to discriminate $t\bar{t}Z$ signal events from background events. It is described in detail which input variables are used, which hyperparameter settings were chosen, and it is analysed how different choices influence the separation power. In chapter 10 the estimation of the various systematic uncertainties included in the calculation of the cross section are shown. The agreement of simulation and data in the signal region is analysed in chapter 11. Sensitivity and optimisation studies using simulations are shown in chapter 12. The effects of changes in the boosted jet definition and the separation into two b jet categories are presented. The result of this analysis – the measurement of the $t\bar{t}Z$ production cross section – is discussed in chapter 13. The final chapter 14 presents possibilities for further studies, namely the analysis of different signal regions as well as opportunities at LHC Run 3.

Part I
Theoretical and Experimental Basis

THEORETICAL INTRODUCTION

2.1 The Standard Model of Particle Physics

The standard model of particle physics has long since become an irreplaceable part of modern day high energy physics. Developed in the 60s and 70s of the past century, its predictions and parameters have been precisely measured.

The standard model is a gauge field theory with the gauge symmetry group [4]

$$SU(3) \times SU(2) \times U(1). \quad (2.1)$$

This threefold symmetry is the result of the combination of the gauge field theories of three fundamental forces: electromagnetism (quantum electrodynamics, QED), the weak force, and the strong force (quantum chromodynamics, QCD). Electromagnetism and the weak force are further combined to form the electroweak interaction (described in section 2.1.1), while the strong force (described in section 2.1.2) remains separate.

The standard model predicts at least three generations of particles. The existence of three generations is experimentally well established while the existence of a fourth or higher generation is strongly discouraged, for example in measurements of the width at the Z peak by the Large Electron Positron Collider (LEP) [5]. Each generation of particles contains two leptons and two quarks, as well as their corresponding antiparticles. The lepton pairs consists of one electrically charged lepton (electron, muon, tau) and a corresponding electrically uncharged neutrino. The pair of quarks contains one up-type and one down-type quark with electrical charges $+\frac{2}{3}e$ and $-\frac{1}{3}e$. In addition to these twelve fermions, each of the three gauge field theories also includes mediator gauge bosons: the photon (γ) for QED, the W and Z bosons for the weak interaction and the gluon for QCD. Another bosonic particle is made necessary by the electroweak theory. Without an additional field, predicted cross sections diverge at high momentum transfer. Also, the masses of the W and Z bosons cannot be explained. Both problems can be resolved by the introduction of the Higgs mechanism, completing the standard model.

All elementary particles of the standard model, grouped by generations and interactions, can be seen in figure 2.1.

2.1.1 The Electroweak Interaction

At low energies, the electroweak force appears as two distinct forces: electromagnetism, responsible for a wide range of everyday phenomena, and the weak force, responsible for the β -decay of atomic nuclei but otherwise unobservable. Electromagnetism can be easily explained in a mathematically consistent way by QED. However, no quantum field theory for the weak force alone can be found. Phenomenological theories (like the V-A theory [7]) can only provide a low energy approximation.

A mathematically consistent gauge field theory was found by Glashow, Weinberg and Salam [8–10], by unifying the weak and electromagnetic interactions into the electroweak gauge field theory.

The Electromagnetic Interaction

QED was developed in the late 1920s and is thus the first of the quantum gauge field theories forming the standard model. Many of the necessary principles for describing quantum gauge field theories were initially developed for QED. The Lagrange density of QED is defined as [11]:

$$\mathcal{L}_{QED} = \bar{\psi}(i\gamma^\mu(\partial_\mu - ieA_\mu) - m)\psi - \frac{1}{4}F_{\mu\nu}F^{\mu\nu}, \quad (2.2)$$

with the fermion field ψ (for example an electron), the Dirac matrices γ^μ , the gauge field A_μ , and the field strength tensor $F_{\mu\nu}$:

$$F_{\mu\nu} = \partial_\mu A_\nu - \partial_\nu A_\mu. \quad (2.3)$$

\mathcal{L}_{QED} is invariant under U(1) transformation. It describes electrically charged spin-1/2 particles (ψ), the massless¹ spin-1 photon (by the vector field A_μ) and interactions between them.

The photon couples to all particles that carry electromagnetic charge, with the coupling strength proportional to the electromagnetic charge. The photon itself is uncharged. Thus, there is no direct self-interaction. Without electromagnetic charges present, the photon can propagate without interacting, and the range of the electromagnetic interaction is infinite.

There is no exact solution for the equations of motion of QED, or any other of the quantum field theories of the standard model. Approximate solutions can be found using perturbation theory. This can be visualised using Feynman diagrams. An example of Feynman diagrams for the basic process of QED in leading order and next-to-leading-order (NLO) can be seen in figure 2.2. All possible Feynman diagrams with the same in-going and out-going particles contribute to a process. At leading order, only those with the minimal

¹adding a mass term would destroy the U(1) invariance

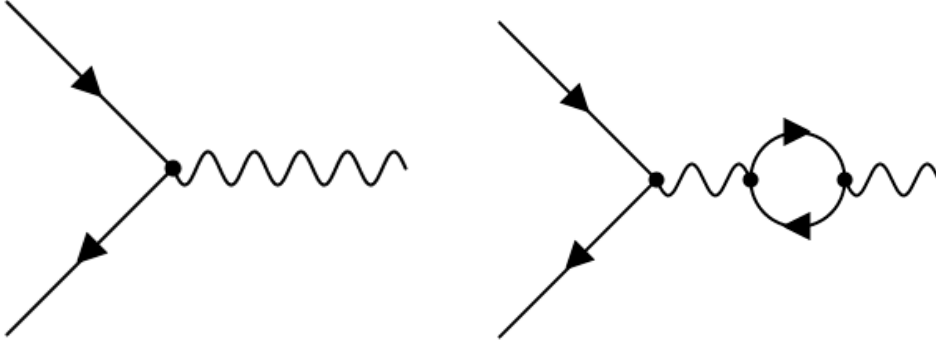


Figure 2.2: Feynman diagrams of QED. On the left, the basic QED vertex is shown, with a fermion-antifermion pair interacting with a photon. The right diagram is one of the next-to-leading-order diagrams of the same process, with two additional vertices in the loop.

number of vertices are considered. For higher orders, additional loops are added to the diagrams.

These loops, however, add diverging integrals to the cross section calculations. In order to circumvent these divergences and recover finite cross section values, a mathematical procedure known as renormalisation is used. This leads to a momentum-transfer dependent coupling. While this historically led many physicists to believe that QED must be wrong, 'running' coupling constants are an experimentally well established fact today [12].

The Weak Interaction

All standard model fermions are affected by the weak force. As it is the only flavour-changing interaction, it is responsible for all decays of elementary particles. There is no renormalisable gauge field theory describing the weak interaction on its own. However, a renormalisable theory combining the weak force and the electromagnetic force to the electroweak force is possible. In the standard model, the electroweak force is described by a gauge field theory with the combined symmetry group $SU(2) \times U(1)$. The Lagrangian is [11]:

$$\mathcal{L}_{EW} = \bar{\psi} i \gamma^\mu (\partial_\mu - ig B_\mu - ig' \frac{\sigma_i}{2} W_i^\mu) \psi - \frac{1}{4} \text{Tr}(W_{\mu\nu} W^{\mu\nu}) - \frac{1}{4} B_{\mu\nu} B^{\mu\nu}, \quad (2.4)$$

with

$$W_{\mu\nu} = \partial_\mu \frac{\sigma_i}{2} W_i^\nu - \partial_\nu \frac{\sigma_i}{2} W_i^\mu - ig \left[\frac{\sigma_i}{2} W_i^\mu, \frac{\sigma_i}{2} W_i^\nu \right]. \quad (2.5)$$

$B_{\mu\nu}$ and B_μ are identical to $F_{\mu\nu}$ and A_μ from QED. The W_i^μ is the triplet of spin 1 fields needed for $SU(2)$ invariance: W^+ , W^- , and W^0 . W^+ and W^- appear in nature as the charged vector bosons of the weak interaction. The W^0 mixes with the also uncharged B^0

from the U(1) symmetry to the weakly interacting Z boson and the electromagnetically interacting photon [4]:

$$\gamma = \cos \theta_W B^0 + \sin \theta_W W^0, \quad (2.6)$$

$$Z = -\sin \theta_W B^0 + \cos \theta_W W^0, \quad (2.7)$$

with the weak mixing angle $\theta_W = 15^\circ$. The electroweak constants g and g' are connected to the electromagnetic constant e [4]:

$$g = e \sin(\theta_W), \quad g' = g \tan(\theta_W) \quad (2.8)$$

Unlike the photon, the weak gauge bosons W and Z are not massless, but have a large mass of about 80.4 and 91.2 GeV, respectively [13]. As for QED, mass terms for the gauge bosons break the gauge invariance and therefore require an additional term in the Lagrangian. Due to the large mass of the gauge bosons, the weak interaction has a very low range of the order of 10^{-17} m.

The conserved charge-like quantum number of the weak interaction is called the weak isospin T . T acts like the spin of a particle. A particle with $T = 1/2$ has two possible states T_3 : $+1/2$ and $-1/2$, representing the flavour of the particle. Up-type quarks and neutrinos have positive T_3 , down-type quarks and charged leptons have negative T_3 .

Only left-handed particles and right-handed antiparticles carry weak isospin. Their right and left-handed counterparts do not take part in the weak interaction. For neutrinos, as they only interact weakly, this means that right-handed neutrinos (left-handed antineutrinos) do not exist in the standard model.

The W boson has $T_3 = \pm 1$ and thus changes the flavour of a particle to the flavour of its isospin partner. Decays between different generations of fermions are forbidden in this formulation. For quarks, however, these decays are an experimentally observed fact. The mass eigenstates that can be observed in nature can be explained as mixed states of the weak interaction. This mixing is described in the unitary CKM matrix [14, 15]:

$$V_{\text{CKM}} = \begin{pmatrix} V_{ud} & V_{us} & V_{ub} \\ V_{cd} & V_{cs} & V_{cb} \\ V_{td} & V_{ts} & V_{tb} \end{pmatrix} \quad (2.9)$$

with the probability of transition between quark q_i and quark q_j being $|V_{q_i q_j}|^2$. The values of the matrix elements have been measured with high accuracy and agree with the prediction of a unitary matrix. The measured values are [13]:

$$V_{\text{CKM}} = \begin{pmatrix} 0.9737 & 0.2245 & 0.00382 \\ 0.221 & 0.987 & 0.0410 \\ 0.008 & 0.0388 & 1.013 \end{pmatrix} \quad (2.10)$$

As the off-diagonal elements are up to two orders of magnitude smaller than the diagonal elements, decays between different generations are suppressed. As the decay of lighter quarks of the second and third generations (s and b) into heavier quarks (c and t) is kinematically forbidden, only flavour-changing decays across families are possible. This leads to a relatively long lifetime for s and b quarks, compared to their up-type iso-spin partners.

The Brout-Englert-Higgs Mechanism

As already mentioned in the previous section, the electroweak Lagrangian (equation 2.4) does not permit mass terms for the gauge bosons, as they would break the $SU(2)$ symmetry. In addition, self-interaction between the vector bosons W and Z leads to divergent cross sections. Both problems of the theory can be solved by the Brout-Englert-Higgs mechanism [16, 17], which introduces an additional scalar field with a corresponding boson: the Higgs boson H.

The Higgs mechanism introduces a complex $SU(2)$ doublet of scalar fields ϕ :

$$\phi = \begin{pmatrix} \phi^+ \\ \phi^0 \end{pmatrix}. \quad (2.11)$$

ϕ is added to the Lagrange density by:

$$\mathcal{L}_{Higgs} = (D_\mu \phi)^\dagger D^\mu \phi - V(\phi) \quad (2.12)$$

with the coupling terms to the standard model included in D_μ :

$$D_\mu = (\partial_\mu - igB_\mu - ig' \frac{\sigma_i}{2} W_i^\mu) \quad (2.13)$$

and with the potential

$$V(\phi) = \mu^2(\phi\phi^\dagger) + h(\phi\phi^\dagger)^2 \quad (2.14)$$

with parameters μ and h . The electroweak Lagrangian including the new field ϕ is still invariant under $SU(2)$ and $U(1)$ gauge transformations. All symmetries stay intact, and the theory is renormalisable. Spontaneous symmetry breaking – meaning an unsymmetrical ground state of an otherwise symmetrical model – can now be included via the choice of the parameters of the potential V . A negative value of h would lead to a potential with no minima, which is not physically sensible. Hence, h has to be positive. The sign of μ^2 determines the number and position of the minima for $h > 0$. $\mu^2 > 0$ would lead to a single trivial minimum at $\phi_0 = 0$. A negative μ^2 however, creates a local maximum at $\phi_0 = 0$ with a family of minima circular around it:

$$|\phi_0| = \sqrt{\frac{-\mu^2}{2h}} = \frac{v}{\sqrt{2}}, \quad (2.15)$$

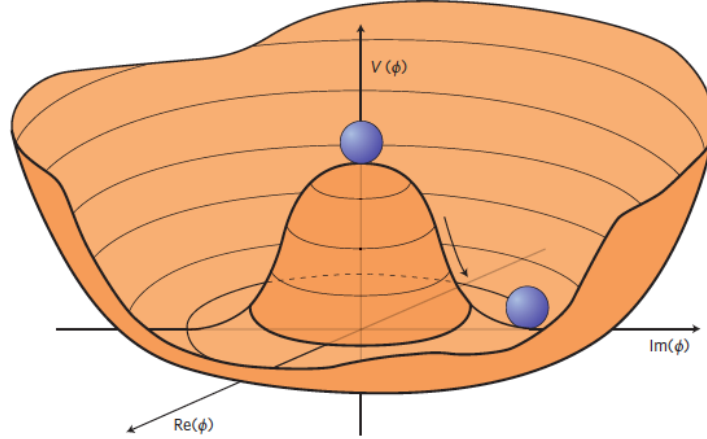


Figure 2.3: The Higgs potential $V(\phi)$. A negative μ^2 leads to the 'Mexican hat potential' with a family of minima on a circle. Figure taken from Ref. [18].

with the vacuum expectation value v . The two-dimensional shape for the potential $V(\phi)$ with $\mu^2 < 0$ ('Mexican hat potential') can be seen in figure 2.3. A potential with $\mu^2 < 0$ leads to spontaneous symmetry breaking, as one point on the circular $\phi_0 = 0$ has to be chosen. The inclusion of the potential at its minimum into the electroweak Lagrangian leads to typical mass terms:

$$\left(\frac{g'v}{2}\right)^2 W_\mu^- W^{+\mu}. \quad (2.16)$$

Further analysis of the behaviour of W^μ and B^μ (for example described in Ref. [11]) show, that apart from the W bosons, the Z boson also obtains a mass, while the photon remains massless. This can be explained by the fact that the spontaneous symmetry breaking only affects the $SU(2)$ symmetry, while the $U(1)$ symmetry of electromagnetism stays unbroken.

This way, three of the four fields of the complex doublet ϕ are integrated by the massive vector bosons W^- , W^+ and Z . The fourth field stays unaffected. Excitations of this free field lead to an additional boson which is massive and scalar (spin 0), called the Higgs boson.

The Brout-Englert-Higgs mechanism also generates the masses of elementary fermions. In order to do this, the gauge invariant so-called Yukawa term [11]

$$\mathcal{L}_{\text{fermion}} = -\lambda_f(\bar{\psi}_L \phi_0 \psi_R + \bar{\psi}_R \phi_0 \psi_L) \quad (2.17)$$

is added to the Lagrange density. The Yukawa coupling λ_f denotes the coupling strength between fermion and Higgs potential and is directly proportional to the mass of the fermion. Mass is generated via the coupling of the right and left-handed components of the fermion wave function $\psi_{L,R}$, to the Higgs potential.

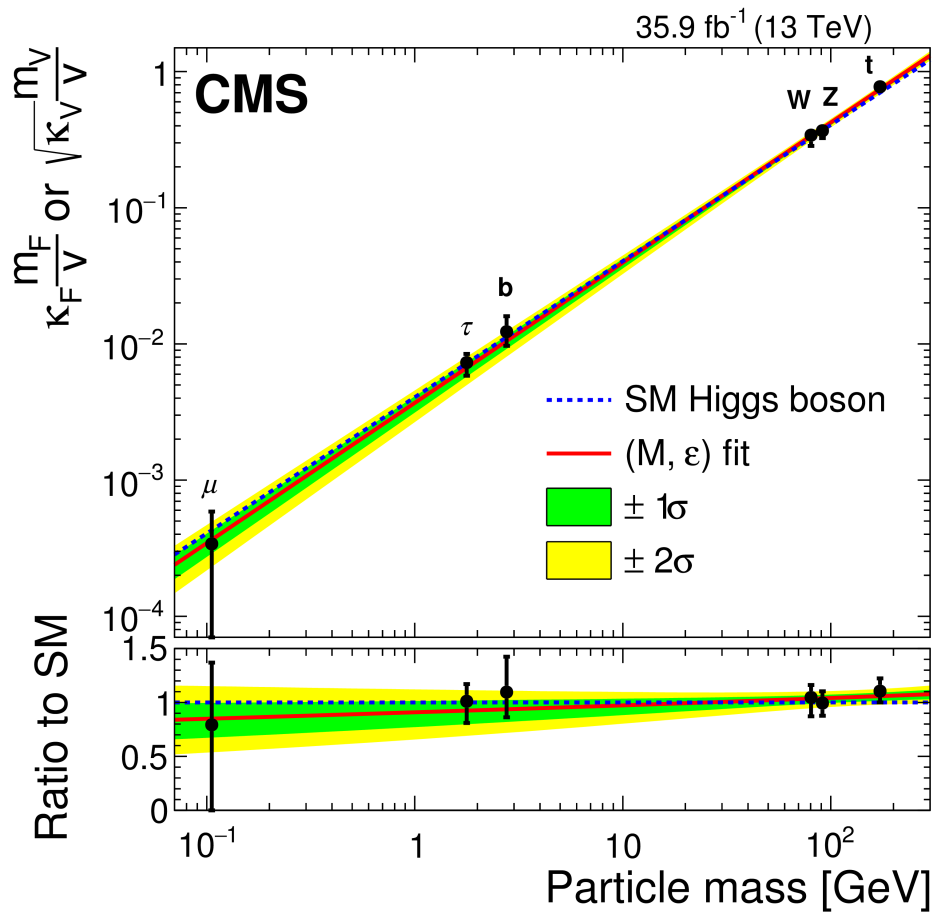


Figure 2.4: Measured coupling strengths of the Higgs boson to massive fermions and bosons. The blue dashed line shows the standard model expectation. The red line with the yellow and green error band shows the best fit to the measured data points. Figure taken from Ref. [19].

The Yukawa coupling strengths can be measured using the cross sections of Higgs boson processes. Measurements of the couplings to top [20–22] and b quarks [23], as well as tau leptons [24] and muons [25] show excellent agreement to the expected proportionality to fermion mass. The coupling to vector bosons is expected to be proportional to the square of the boson mass. Measurements of these couplings [26, 27] are also in agreement with the standard model prediction. A summary plot of these measurements can be seen in figure 2.4.

2.1.2 The Strong Interaction

The strong interaction is the force that binds nucleons into atomic nuclei. It is also responsible for the confinement of quarks in hadrons. Due to the strength of the strong force, particles carrying the corresponding charge cannot exist as independent particles, but almost immediately form hadrons. However, in fixed target experiments it was found that, at high momentum transfer, the quarks in protons behave as free particles [28]. This leads to the conclusion that, contrary to electrodynamics, the coupling strength of the strong interaction decreases at higher energies. This behaviour is explained with a quantum gauge field theory with the gauge group $SU(3)$ [29]. In analogy to quantum electrodynamics, this theory is called quantum chromodynamics (QCD). The Lagrangian is [11]:

$$\mathcal{L}_{QCD} = \sum_{i,j=1}^3 \bar{q}_i (i\gamma^\mu D_{\mu,ij} - m_q \delta_{ij}) q_j - \frac{1}{4} \sum_{a=1}^8 G_{\mu\nu}^a G^{a,\mu\nu}, \quad (2.18)$$

with the quark mass m_q , the quark wave function q_j , the covariant derivative D_μ ,

$$D_{\mu,ij} = \delta_{ij} \partial_\mu + \frac{i}{2} g_S (\lambda_a)_{ij} G_\mu^a \quad (2.19)$$

and the gluon field tensor:

$$G_{\mu\nu}^a = \partial_\mu G_\nu^a - \partial_\nu G_\mu^a + i f_{bc}^a G_\mu^b G_\nu^c. \quad (2.20)$$

The sum over i and j in equation 2.18 describes three colour charges, the summation over a includes eight different gluon fields G_μ^a . The λ_a are the eight Gell-Mann matrices, forming the basis of $SU(3)$. The f_{abc} are the corresponding structure constants $f_{abc} = \frac{1}{4} i \cdot \text{tr} \lambda_a [\lambda_b, \lambda_c]$.

The three different colour charges of the strong interaction are commonly called "red", "green" and "blue". A quark carries one of the colour charges. Colour neutral hadrons can be formed as either combinations of three differently coloured quarks (baryons), or of a quark and antiquark that carry the same colour (mesons). The eight massless gluons carry different combinations of colour and anti-colour that do not combine to colour neutrality. As the gluons are colour-charged particles, they do not only interact with the quarks,

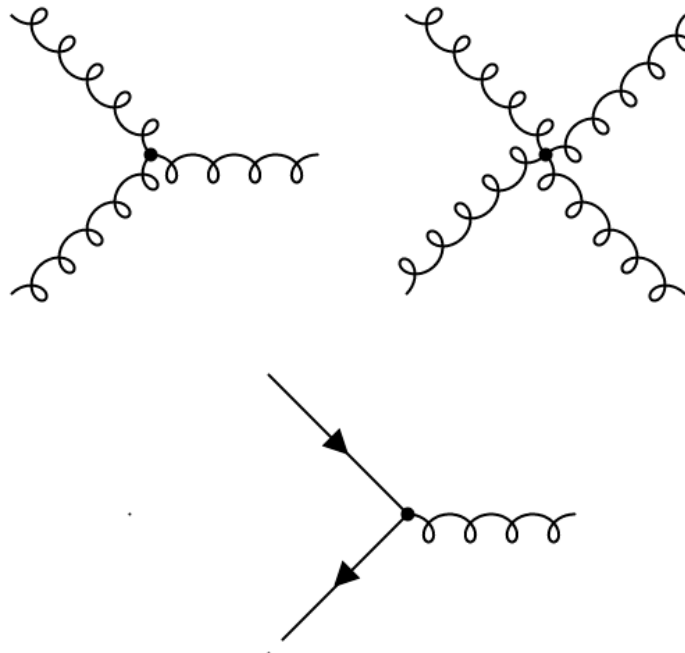


Figure 2.5: The basic vertices of QCD. The gluon self-interaction vertices are shown at the top. They can contain either three or four gluons. The bottom diagram shows the interaction between quarks and a gluon.

but they also self interact. This self-interaction of massless gauge bosons is the cause of confinement, at low energy, where the coupling is strong, and asymptotic freedom, towards large energies, where the coupling strength decreases. Feynman diagrams of the basic vertices of QCD can be seen in figure 2.5.

2.2 The Z Boson

The Z boson is an electrically neutral gauge boson of the weak interaction. It is the mediator of the weak neutral currents. Weak neutral currents, and with them indirectly the Z bosons, were first discovered at CERN in 1973 in the Gargamelle bubble chamber [30]. Direct discovery was achieved ten years later in 1983, also at CERN, at the SPS collider [31, 32].

The Z boson has a mass of about 91.2 GeV [13]. It couples to all particles carrying weak hypercharge Y [4]:

$$Y = 2(Q - T_3). \quad (2.21)$$

Table 2.1: The experimental branching ratios for Z boson decays. Only significant branching ratios are shown. The values are taken from Ref. [13].

Decay mode	branching ratio (in %)
e^+e^-	3.363 ± 0.004
$\mu^+\mu^-$	3.366 ± 0.007
$\tau^+\tau^-$	3.370 ± 0.008
neutrinos	20.00 ± 0.06
hadrons(all)	69.91 ± 0.06
up-type/2	11.6 ± 0.6
down-type/3	15.6 ± 0.4
$c\bar{c}$	12.03 ± 0.21
$b\bar{b}$	15.12 ± 0.05

The weak hypercharge is a combination of the electromagnetic charge Q and the third component T_3 of the weak isospin. All known elementary fermions, as well as the Higgs boson, carry weak hypercharge. The coupling is measured via the branching fractions of the Z boson decays. Z bosons decay exclusively into fermion antifermion pairs. The branching ratios can be seen in table 2.1. The coupling to neutrinos is strongest, with about 20% of all Z bosons decaying into neutrinos. The coupling to charged leptons is half – about 10% of Z bosons decay to charged leptons. The coupling to quarks is of similar strength, however the phase space for hadronic decays is tripled by the colour charge of the quarks. About 70% of all Z bosons decay hadronically. These 70% can be subdivided into 12% per up-type quark (u and c), and 15% per down-type quark (d,s,b). As the weak hypercharge is identical for fermions of different generations, the couplings to the Z bosons are expected to be identical for quarks and leptons of different generations. The coupling to top quarks cannot be measured this way, as the decay is kinematically forbidden due to the high mass of the top quarks. This coupling can be measured by analysing the cross sections of processes containing a top-Z vertex. An excellent process at the LHC is the $t\bar{t}Z$ process, which is analysed in this thesis.

2.3 The Top Quark

The top quark is the up-type quark of the third generation and weak isospin partner of the b quark. With a mass of about 172 GeV [13], it is the heaviest elementary particle known to exist. It was discovered at Fermilab by the CDF and D0 experiments in 1995 [33, 34]. Due to its large mass, the top quark only has a lifetime of about 5×10^{-25} s. As this is more than an order of magnitude smaller than the timescale for hadronisation, the top quark decays before forming hadrons, which makes it the only quark that can be studied

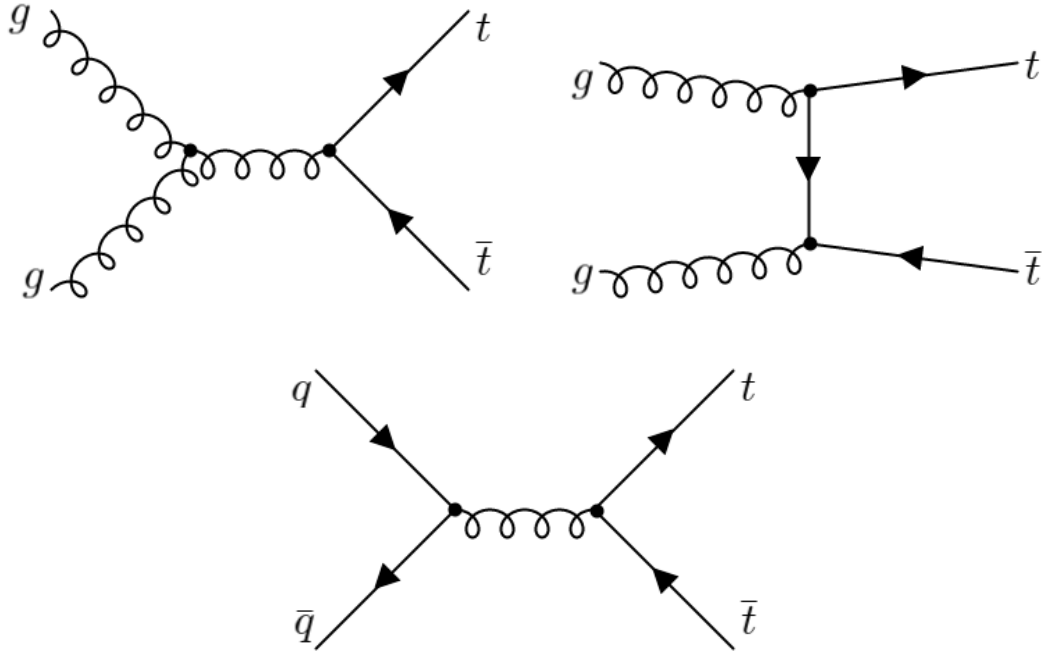


Figure 2.6: The most relevant production processes of top quark-antiquark pairs.

in its bare state. The large mass, more than 30 times the mass of the second heaviest fermion, the b quark, may also provide hints to physics beyond the standard model, since its origin is not yet explained. Another motivation to study the top quark is that it has not been so extensively studied as other particles, since only now with the LHC there is sufficient energy and luminosity to produce top quarks in vast amounts. This offers the possibility for top quark measurements with unprecedented precision. For these reasons, top quark physics is a central topic of the LHC physics programme.

In proton-proton collisions, single top quarks are produced via the weak interaction, from b quarks. At the LHC, top quarks are produced about four times more often via the strong interaction, in the form of top quark-antiquark pairs ($t\bar{t}$) from the fusion of gluons or quark-antiquark pairs. Feynman diagrams for the production processes can be seen in figure 2.6. The cross section for $t\bar{t}$ production at a centre of mass energy of $\sqrt{s} = 13$ TeV has been measured by both ATLAS and CMS to be $830 \pm 0.4(\text{stat}) \pm 36(\text{syst}) \pm 14(\text{lumi})$ pb (ATLAS, [35]) and 791 ± 25 pb (CMS, [36]). Both measurements agree with the theoretical prediction, which is calculated in next-to-next-to-leading order (NNLO) [37]:

$$\sigma_{t\bar{t},\text{NNLO}} = 794.0^{+3.5\%}_{-5.7\%} \text{ pb} \quad (2.22)$$

The top quark decays almost exclusively into a b quark and a W boson. Top quark-antiquark pairs are usually classified into three categories, via the decays of the two

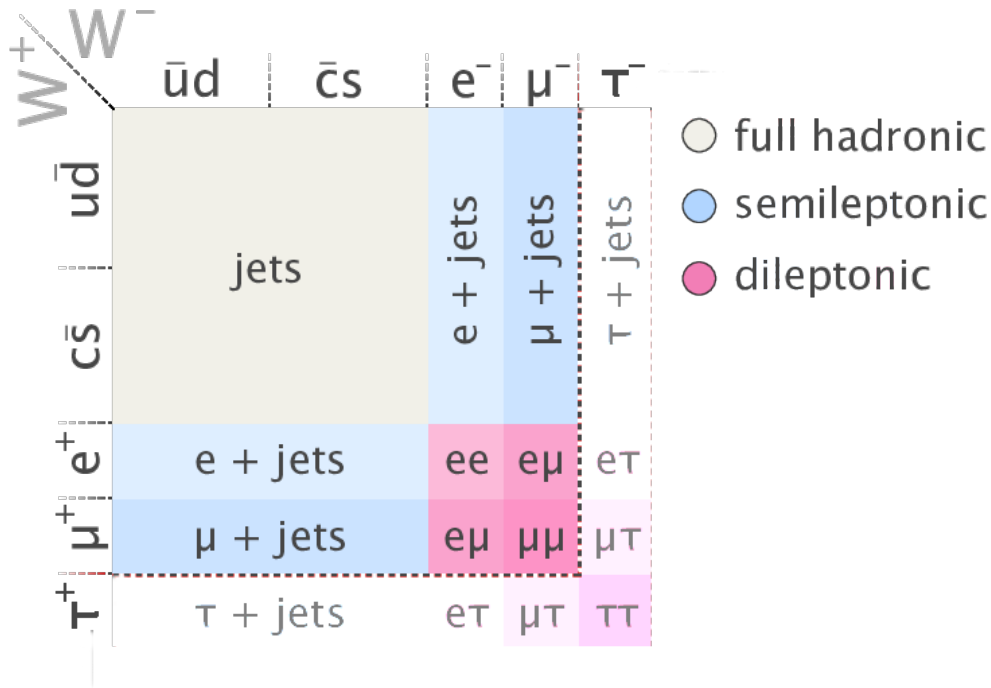


Figure 2.7: The decay channels of the $t\bar{t}$ system, separated by the decays of the two W bosons. Fully hadronic (grey): both W bosons decay hadronically, semi-leptonic: one W decays hadronically one decays leptonically or dileptonic: both W bosons decay leptonically. While decays into tau leptons are considered leptonic, tau leptons are usually not used in dileptonic analyses, as the short lifetime of taus and their hadronic decay channels make tau reconstruction a difficult task. Figure adapted from [38] (removed details on tau decays).

W bosons they produce:

- Fully hadronic: Both W bosons decay hadronically (45.7%)
- Semi-leptonic: One W decays hadronically, one decays leptonically (43.8%)
- Dileptonic: Both W bosons decay leptonically (10.5%) [13]

A systematic depiction of these decay channels can be seen in figure 2.7. Due to its large cross section the $t\bar{t}$ process is an excellent source for measurements of 3rd generation standard model parameters and the search for possible deviations, for example by looking at processes where the top quark is produced in association with additional particles. The electromagnetic coupling of the top quark can be measured, for example, in $t\bar{t} + \gamma$ [39, 40],

while couplings to heavy vector bosons are measured in $t\bar{t}+W$ [41, 42] and $t\bar{t}+Z$ processes [43, 44]. As the $t\bar{t}Z$ process is the main topic of this thesis, the theoretical predictions of the process are discussed in the following section. Previous experimental results are shown in chapter 6.

2.4 The $t\bar{t}Z$ Production Process

The production of a top quark-antiquark pair in association with a Z boson ($t\bar{t}Z$) is a process predicted by the standard model. By measuring the cross section, the coupling between the top quark and the Z boson can be determined, and possible deviations from the standard model can be discovered [45].

As for $t\bar{t}$ production, the production of $t\bar{t}Z$ at the LHC is also dominated by strong processes. Feynman diagrams for the $t\bar{t}Z$ process can be seen in figure 2.8. Theoretical predictions of the cross section are calculated at NLO accuracy in QCD [46–49]. Additional electroweak corrections are also included in the calculations [50]. The latest theoretical publication on the cross section of $t\bar{t}Z$ summarises the previous measurements and adds additional next-to-next-to-leading logarithmic (NNLL) corrections [51]. A summary of the cross section calculations can be seen in figure 2.9. The best cross section calculation of the $t\bar{t}Z$ process is obtained from averaging over the four different scale calculations with NNLL corrections. For a centre-of-mass energy of 13 TeV, it is calculated to be [51]:

$$\sigma_{t\bar{t}Z} = 859_{-9.5\%}^{+8.6\%+2.3\%} \text{ fb.} \quad (2.23)$$

The $t\bar{t}Z$ process is also suitable for searches for physics beyond the standard model, as the cross section is sensitive to anomalous couplings of the top quark to the Z boson. The terms of the standard model Lagrangian concerning $t\bar{t}Z$ interactions can be written as [52]:

$$\mathcal{L}_{t\bar{t}Z}^{SM} = e\bar{t}[\gamma^\mu(C_V^Z + \gamma_5 C_A^Z)]tZ_\mu, \quad (2.24)$$

with the standard model vector and axial vector couplings C_V^Z and C_A^Z . This Lagrangian can be extended to include anomalous couplings:

$$\mathcal{L}_{t\bar{t}Z} = e\bar{t}[\gamma^\mu(C_{V,1}^Z + \gamma_5 C_{A,1}^Z) + \frac{\sigma^{\mu\nu} q_\nu}{M_Z}(C_{V,2}^Z + \gamma_5 C_{A,2}^Z)]tZ_\mu, \quad (2.25)$$

with $\sigma^{\mu\nu} = i/2[\gamma^\mu, \gamma^\nu]$ and $q_\nu = (p_{T,t} - p_{T,\bar{t}})_\nu$. In the standard model, $C_{V,2}^Z$ and $C_{A,2}^Z$ are finite, they are however negligibly small. If a beyond the standard model mechanism were to change these couplings to be of comparable magnitude as the $C_{AV,1}^Z$, this would affect the cross section of the $t\bar{t}Z$ process. Figure 2.10 shows predictions of the differential $t\bar{t}Z$ cross section, as a function of the p_T of the Z boson, for the standard model in blue and for a hypothetical new physics scenario where $C_{V,2}^Z$ and $C_{A,2}^Z = 0.2$ in red. While the total cross section is only slightly affected, the shape of the distribution changes significantly. Cross section enhancements can therefore be detected in $t\bar{t}Z$ events with high p_T Z bosons.

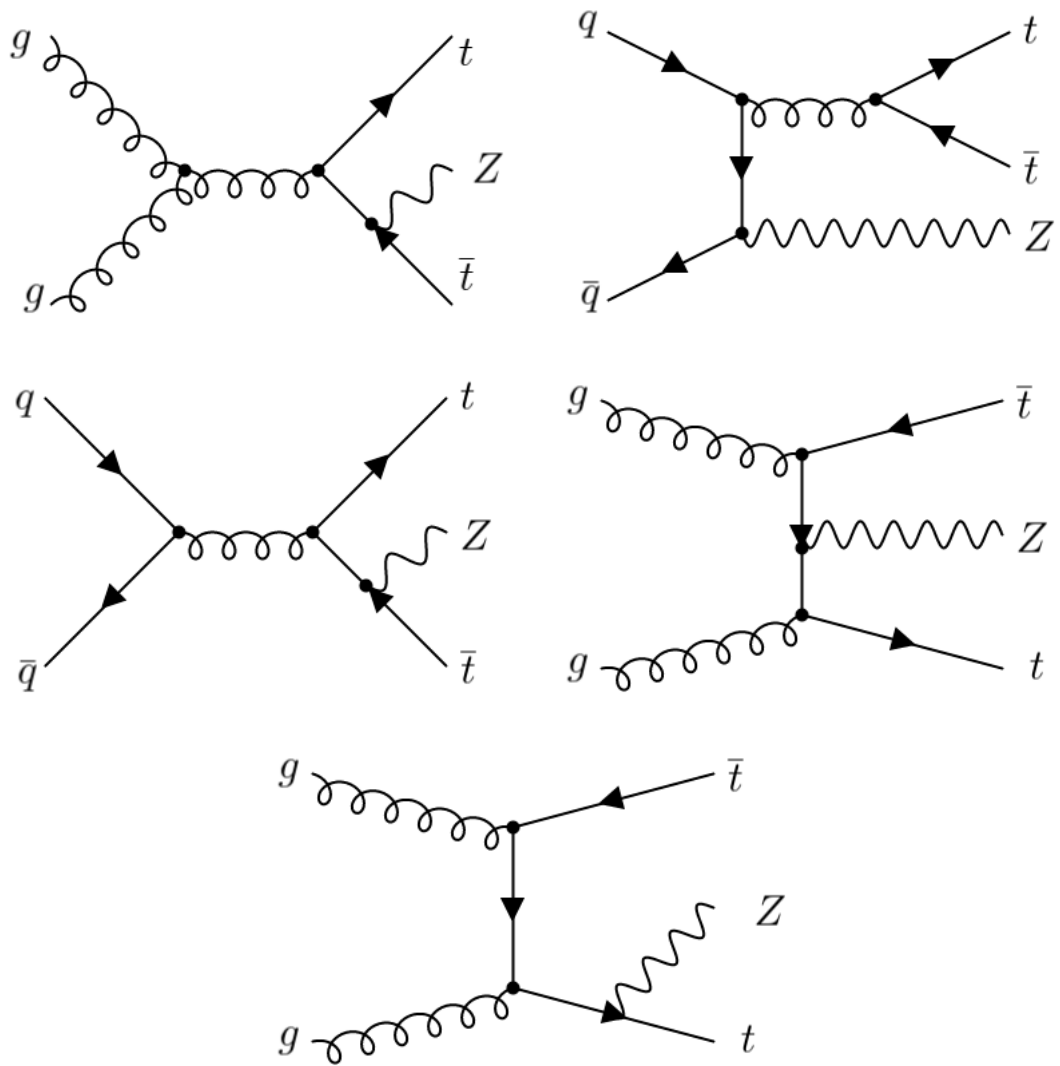


Figure 2.8: Examples for production Feynman diagrams of the $t\bar{t}Z$ process in leading order, by the strong interaction. This is not a complete list. All diagrams can for example be charge conjugated, or the Z can be switched with the gluon in the top right diagram.

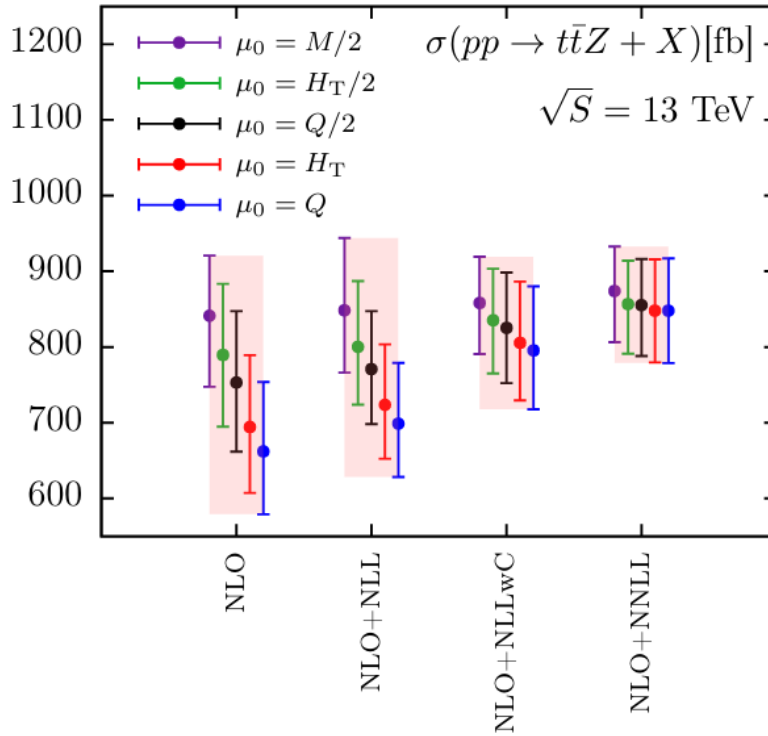


Figure 2.9: Predictions of the $t\bar{t}Z$ cross section, for different levels of accuracy, with five different choices for the renormalisation scale. For the highest accuracy level up to date (NLO+NNLL), the choice of scale has only a minimal effect on the result, therefore the five calculations are averaged for the final cross section calculation. Figure taken from Ref. [51].

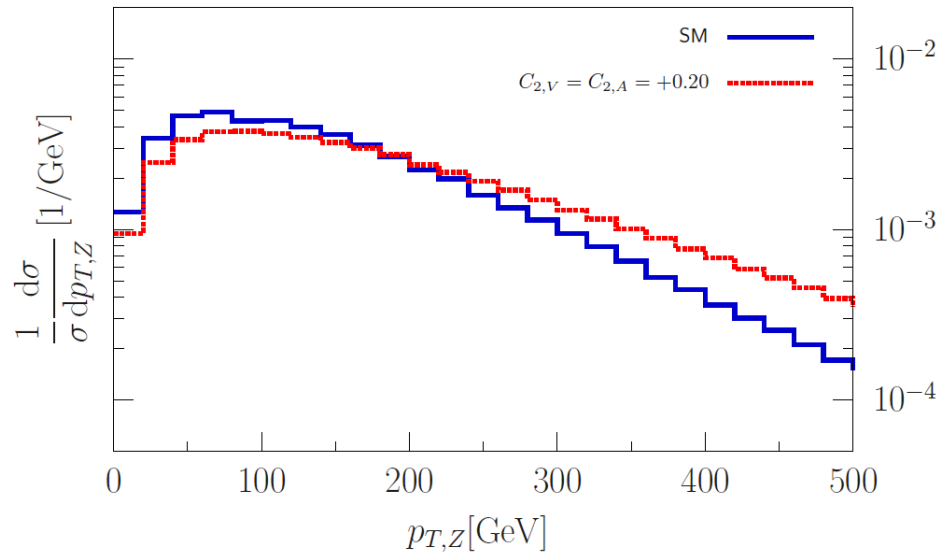


Figure 2.10: Cross section of the $t\bar{t}Z$ process, as a function of the p_T of the Z boson, for the standard model (shown in blue) and for a model with anomalous top- Z couplings $C_{V,2}^Z$ and $C_{A,2}^Z = 0.2$ (shown in red). While the total cross section is changed only minimally, the shape of the distribution is affected more significantly and high p_T Z bosons are more likely. Figure adapted from [52] (axis label moved from right to left).

As in all sciences, the experimental confirmation or refutation of theories is essential in fundamental physics. No theory can withstand contradictory experimental evidence. Both confirmation and refutation are equally important to scientific progress. On the one hand, the standard model has been confirmed time and again in countless measurements – on the other hand, many ground-breaking scientific advancements were led on by experimental surprises.

In this chapter, the experimental setup that is used to produce and collect the data analysed in the third part of this thesis in chapters 6 to 14 is shown. Section 3.1 describes the CERN accelerator complex and the Large Hadron Collider (LHC). An overview of luminosity and the general techniques to measure it is shown in section 3.2, and section 3.3 explains the Compact Muon Solenoid (CMS) Experiment. In section 3.4, a special focus is put on luminosity detectors, especially the Fast Beam Conditions Monitor (BCM1F), as the calibration of this detector is a part of this thesis.

3.1 The Large Hadron Collider

The Large Hadron Collider (LHC) is a particle accelerator located at CERN near Geneva, Switzerland. It measures 27 km in circumference and accelerates proton and heavy ion beams to an energy of 6.8 TeV. Two beams are accelerated in opposite direction and brought to collision in four interaction points, within the caverns of the LHC experiments: ATLAS¹ [54] and CMS [55], general-purpose detectors searching for new physics, ALICE² [56], an experiment specialised in heavy-ion physics, and LHCb³ [57], an experiment dedicated to the physics of b quarks.

The LHC is a synchrotron, a circular accelerator that keeps the particles on a fixed orbit during acceleration by augmenting the magnetic field of the deflection magnets. This requires a minimum energy for the injected particles. Therefore, the LHC is connected to

¹A Toroidal LHC ApparatuS

²A Large Ion Collider Experiment

³Large Hadron Collider Beauty

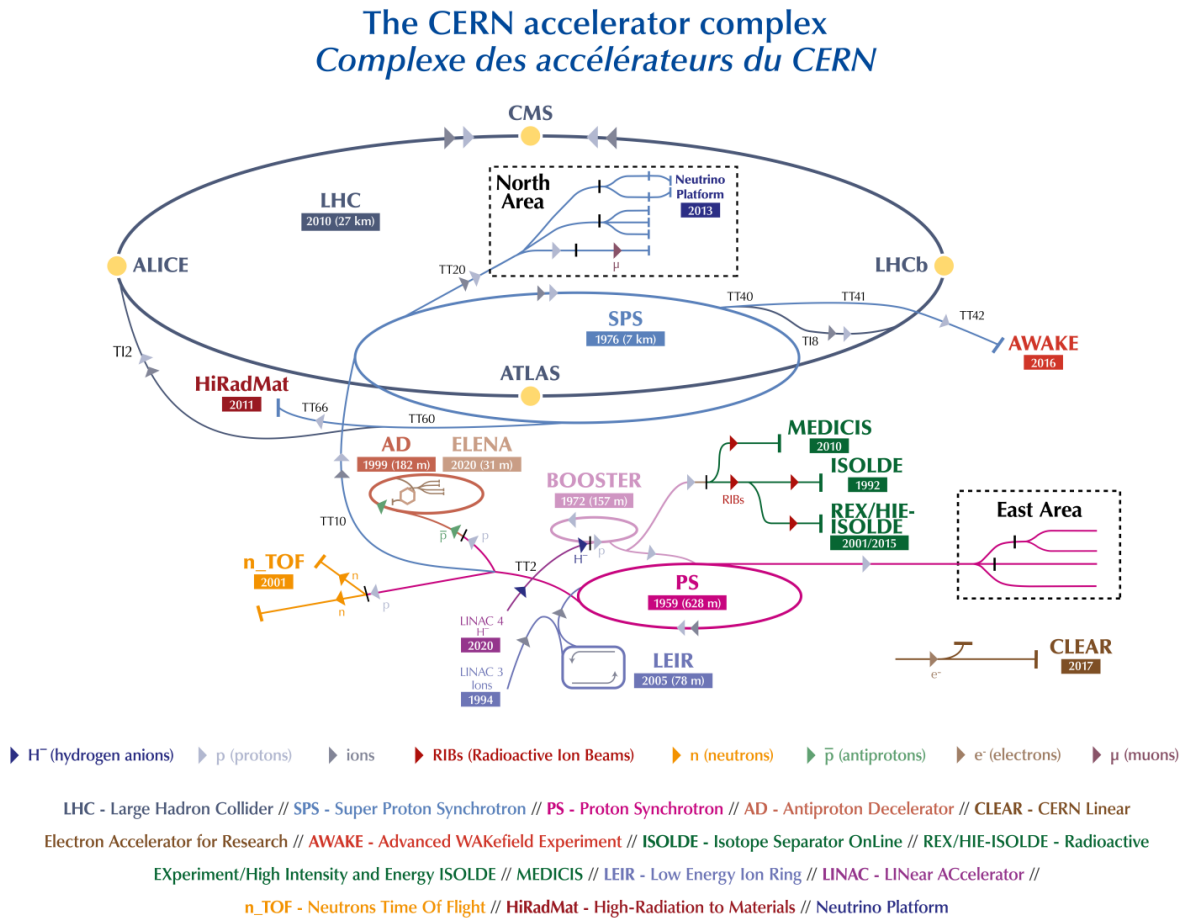


Figure 3.1: The accelerator complex at CERN. Figure taken from Ref. [53].

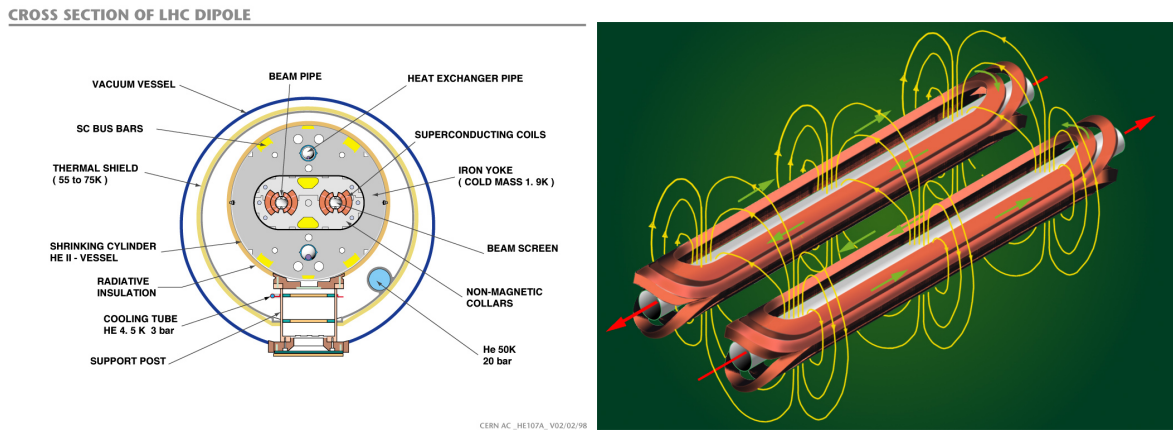


Figure 3.2: Cross section of an LHC dipole magnet (left) and the magnetic field created around the beam pipes (right). The magnetic field points upwards in one and downwards inside the other beam pipe. That way, protons or ions are accelerated in opposite directions. Figures taken from Refs. [58] (left) and [59] (right).

a number of pre-accelerators known as the CERN accelerator complex. This complex is shown in figure 3.1. The protons are first accelerated as a continuous beam in the linear accelerator LINAC4, to an energy of 50 MeV. From there, they are injected into the Proton Synchrotron Booster, where the continuous beam is separated into bunches with about 10^{11} particles in each bunch. At 1.4 GeV, the bunches are inserted into the Proton Synchrotron (PS). There they are accelerated to 25 GeV, when the PS has reached the full capacity of bunches. Then, the bunches are inserted into the Super Proton Synchrotron (SPS) and finally into the LHC when they have reached an energy of 450 GeV.

Several fillings of the SPS are needed in order to reach the capacity of the LHC and, equally, several fillings of the PS are needed to fill the SPS. This creates characteristic filling schemes with so-called bunch trains, series of bunches separated by the minimum time of flight of 25 ns, with larger gaps in between, as the insertion from one synchrotron into the other cannot be done without interruption.

Inside the LHC, the particles are accelerated to their final energy of 6.8 TeV and brought to collision at a centre-of-mass energy of 13.6 TeV. As two beams of positively charged particles need to be accelerated in opposite direction, the dipole magnets used to keep the particles on their orbit need a special design, creating a magnetic field pointing upward on one side and downward on the other. A cross section of such a magnet and the resulting magnetic field can be seen in figure 3.2.

In this thesis, data from the second run period of the LHC (Run 2), is used. This period includes the years 2015-2018, when the LHC operated at a centre-of-mass energy of 13 TeV.

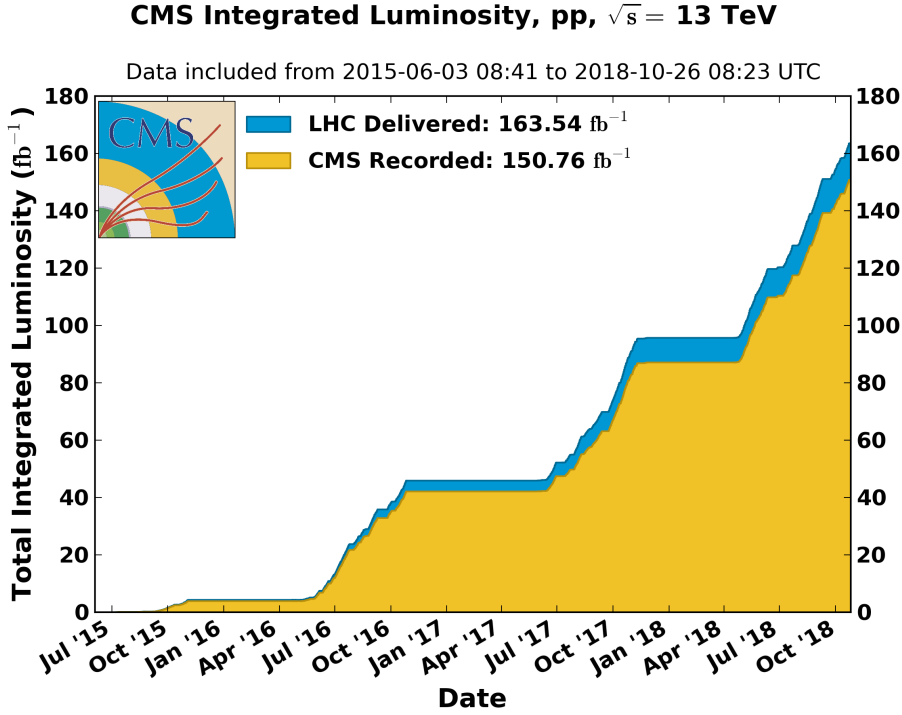


Figure 3.3: The integrated luminosity taken in the years 2015-2018. The luminosity delivered by the LHC is displayed in blue, the fraction of it that was recorded by the CMS Experiment is shown in yellow. Only proton-proton collisions at 13 TeV are considered. Taken from Ref. [63].

3.2 Luminosity

One of the most important features of a particle collider is the instantaneous luminosity. It is a measure for how many events of a given cross section occur per unit of time. The instantaneous luminosity is defined by [60]:

$$L = \frac{1}{\sigma} \frac{\partial N}{\partial t}, \quad (3.1)$$

with the interaction cross section σ , the number of events N and the time t . The design instantaneous luminosity of the LHC is $10^{34} \frac{1}{\text{cm}^2\text{s}}$ [61]. This value was reached in 2016 and in the years 2017 and 2018 more than twice this value was achieved [62].

The instantaneous luminosity integrated over time is a measure for the number of collisions that occurred over a period of time. It is usually stated in inverse barns. The integrated luminosity produced at the LHC and recorded by the CMS Experiment from 2015 to 2018 can be seen in figure 3.3.

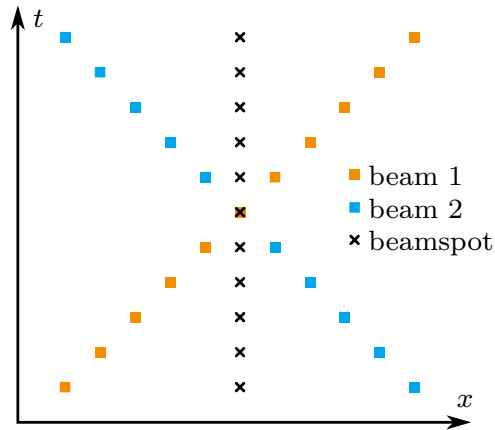


Figure 3.4: Schematic depiction of the beam positions during a VdM scan (with fewer steps). Starting at a maximum separation, the beams are moved closer towards each other until the maximum overlap (head-on collision) is reached and continuing on to again maximum separation. Figure taken from Ref. [65].

3.2.1 Measurement of Luminosity

Precise knowledge of the integrated luminosity is of high importance for experimental analyses. No cross section measurement can be more precise than the precision of the luminosity. Therefore, measuring the luminosity with the highest achievable precision is of the utmost importance.

For a specific collider the instantaneous luminosity can be calculated by [60]:

$$L = \frac{N_A N_B n_b f}{2\pi \Sigma_x \Sigma_y}, \quad (3.2)$$

with the numbers of particles per bunch $N_{A,B}$, the number of bunches n_b , the collision frequency f and the widths of the Gaussian beam profiles $\Sigma_{x,y}$. The beam parameters $N_{A,B}$, n_b and f , are known with sufficient precision. The Gaussian beam profiles however have to be measured. This happens in the so-called Van der Meer scan, named after Simon van der Meer who first proposed the method in 1968 for the intersecting storage rings (ISR) at CERN [64].

Van der Meer scan

A Van der Meer scan (VdM scan) is a method to calibrate the luminosity measurement at particle colliders, using rate measurements. At the LHC, a VdM scan is usually performed once per year to calibrate the luminosity measuring systems.

During the scan, which is performed in a special dedicated filling of the collider, the two beams are separated, reducing the beam overlap region. Starting at a maximum

separation of about six nominal beam widths, the beams are moved closer towards each other until the maximum overlap (head-on collision) is reached and continuing on to again maximum separation. In total, 25 steps with 30s of measuring time each are made. VdM scans are always conducted in pairs, one in horizontal and one in vertical direction. A schematic view of this procedure can be seen in figure 3.4. The rate measurements are plotted over the beam separation, and Gaussian fits are performed separately for each bunch crossing. A distribution of VdM scan data from the BCM1F detector (see section 3.4.1) with a Gaussian fit can be seen in figure 3.5.

The standard deviations of these fits, $\Sigma_{x,y}$, can be used to calculate the luminosity according to the formula 3.2, or to measure the visible cross section of a luminosity measuring system, also referred to as luminometer:

$$\sigma_{vis} = \frac{2\pi\Sigma_x\Sigma_y R_{max}}{N_A N_B}, \quad (3.3)$$

with the rate in head-on collisions R_{max} in one bunch crossing, which is obtained from the peak of the fit. Assuming a linear and stable behaviour of a luminometer, σ_{vis} is a constant and can be used to calculate the instantaneous luminosity from rate measurements for data taking fills. Each colliding bunch is analysed separately and the results are averaged. The bunch-to-bunch variation is used as one of the error estimates for the result.

3.3 The CMS Experiment

The CMS Experiment is one of the four main experiments at the LHC. It is a general purpose experiment designed for precision measurements and the search for new physics. The detector is cylindrical in shape and designed using an onion shell approach: different sub-detectors designed for identifying particles and measuring momentum and energy are installed inside and around a super-conducting solenoid magnet. After a brief introduction to the coordinate system used to describe the detector and events within, the most important sub-detectors are described in this section.

3.3.1 Coordinate System

Both, a spherical and a Cartesian coordinate system are used to describe location inside the CMS Experiment. The origin of both systems is the interaction point located in the centre of the detector, inside the beam pipe. In the Cartesian system, the z axis is defined in the direction of the beam pipe, the x-axis points inward towards the centre of the LHC ring. The spherical system uses the radial distance from the interaction point r , the azimuthal angle ϕ , measured from the x-axis in the x-y plane and the polar angle θ ,

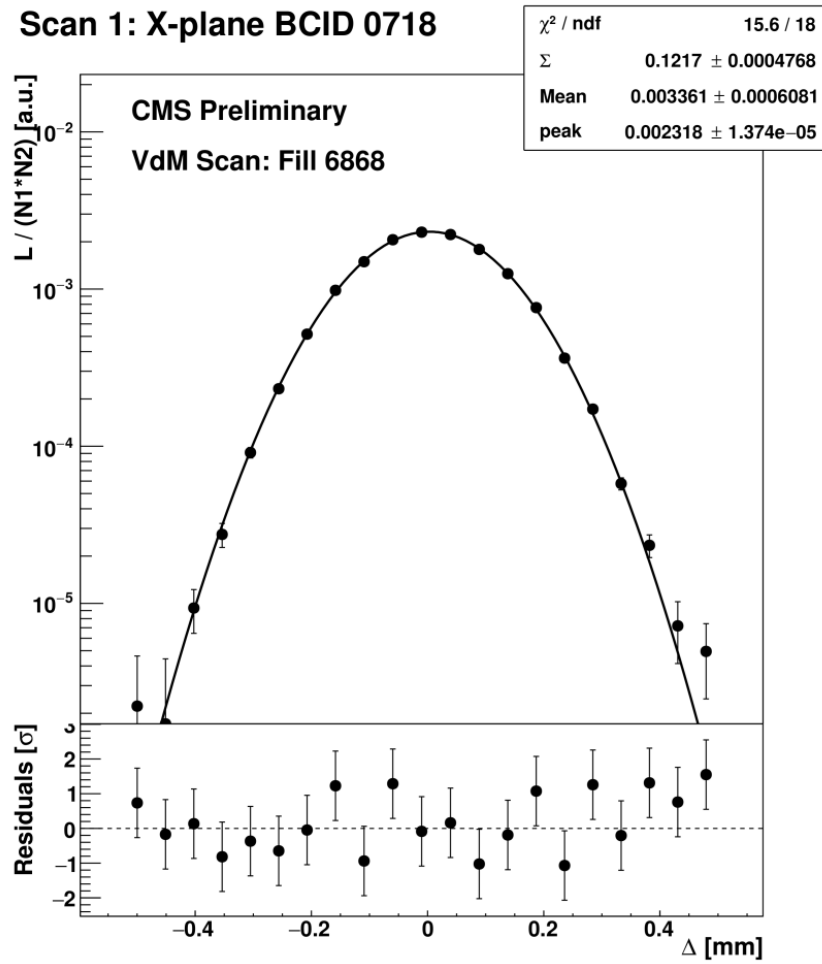


Figure 3.5: Example figure of a Gaussian fit to the rate measurements taken during the VdM scan by the BCM1F detector in 2018. The measured rate is shown on the y-axis, the x-axis shows the separation between the two beams. Figure made with Ref. [66].

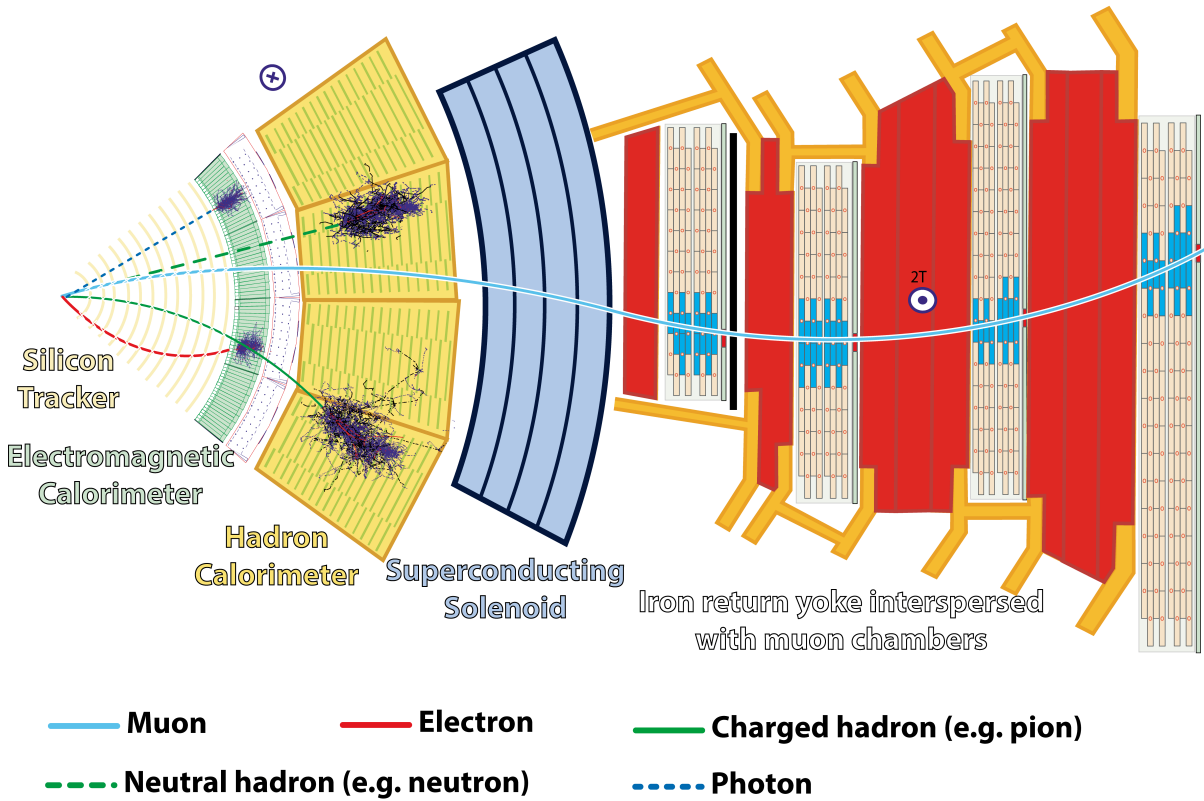


Figure 3.6: A slice of the CMS detector. The different detector layers are shown with left to right indicating inside to outside. The silicon tracking detector is shown in white, the ECAL in green, the HCAL in yellow and the muon system in light orange. The lines indicate the path and interactions of particles within the detector. Figure taken from Ref. [68].

between the y -axis and the z -axis [67].

Another more commonly used variable to describe the polar angle is the pseudorapidity:

$$\eta = -\log \tan \left(\frac{\theta}{2} \right). \quad (3.4)$$

For massless and other highly relativistic particles, this is identical to the rapidity⁴ of the particle [67].

3.3.2 Detector Setup

Tracker

The innermost part of the CMS Experiment is the silicon tracking system, responsible for the reconstruction of tracks of charged particles [69]. Among many different applications, tracks are the basis of reconstructing a particle's momentum as well as the reconstruction of primary and secondary vertices, an indispensable tool for flavour tagging.

The tracking system consists of two parts: the inner and the outer tracker. The inner tracker uses silicon pixel sensors. The pixel tracker, installed during Run 1 (up to 2012) and the first full year of Run 2 (2016), is designed for a maximum of 25 interactions per bunch crossing (also called pileup) with 25 ns bunch spacing, which corresponds to the design luminosity of the LHC. It consists of three cylindrical layers around the beam pipe and two endcap layers at each side [55]. To handle the larger number of interactions per bunch crossing in the later years of Run 2 the inner tracker was replaced in the end-of-year technical stop between 2016 and 2017. The new pixel detector has four layers of sensors in the barrel region and three endcap layers. The resolution is about 10 μm in $r\phi$ and about 20 μm in z direction [69].

For the outer tracker, in a region where the occupancy is lower, silicon strip sensors are used. This system is divided into four parts: The inner and outer barrel, the inner disks and outer endcap (TIB, TOB, TID and TOC). The resolution of the silicon strip tracker is about 35-52 μm in the $r\phi$ and 52 μm in z direction. The tracker system covers an η range up to $\eta = 2.5$ [55]. The layout of the complete tracker can be seen in figure 3.7. In the schematic slice of the CMS detector in figure 3.6 the tracker is displayed in white with yellow lines.

Electromagnetic Calorimeter

The electromagnetic calorimeter (ECAL) is used to identify and to measure the energy of electrons and photons [55, 67, 70]. It consists of a hermetic layer of lead tungstate crystals placed around the tracking system. There are 61200 crystals equipped with avalanche photo diodes in the barrel, and 7324 crystals equipped with vacuum phototriodes in each endcap. In addition, a preshower detector with a higher granularity is installed in front of the endcaps, to identify collimated photons from π^0 decays.

Lead tungstate crystals have a fast reaction (80% of the scintillation light is emitted in 25 ns) and are radiation hard. This makes them an ideal material to use under LHC conditions. Due to the high density of lead tungstate, the 23 cm long crystals cover 26 radiation lengths and 25 radiation lengths in the endcaps.

⁴The rapidity is defined as $y = \frac{1}{2} \log \frac{E+p_z}{E-p_z}$.

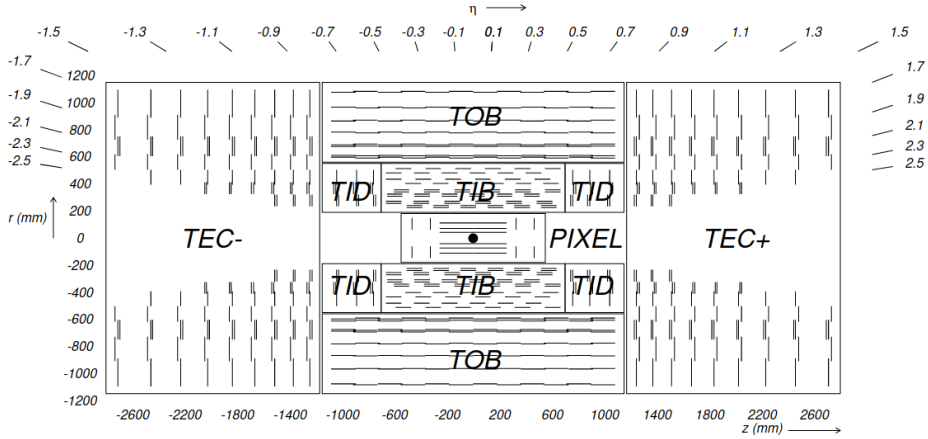


Figure 3.7: The tracking system of the CMS detector. Each line represents a layer of sensors. In the centre, the (non-upgraded) pixel tracker can be seen, with the different strip sensor modules arranged around it. Figure taken from Ref. [55].

The energy resolution is energy-dependent and can be calculated via [70]:

$$\frac{\sigma_E}{E} = \frac{2.8\%}{\sqrt{E}} + \frac{12\%}{E} + 0.30\%, \quad (3.5)$$

with the energy E in GeV. In figure 3.6 the ECAL is shown in green.

Hadron Calorimeter

The hadron calorimeter (HCAL) is a sampling calorimeter consisting of alternating layers of brass absorber and scintillating material. It is located between the ECAL and the solenoid from 1.77 m to 2.95 m from the beam pipe. It measures the energy of hadronic showers and is also used to determine the missing transverse energy $E_{T_{miss}}$. Apart from the main barrel and endcap calorimeters (HB and HE) covering the $|\eta|$ range < 1.3 and from 1.3 to 3.0 respectively, two additional systems are part of the HCAL: the outer calorimeter HO and the forward calorimeter HF. The outer calorimeter consists of an additional layer (two in the central segment of CMS) of scintillator material placed outside the magnet coil, using the magnet and parts of the steel return yoke as absorber. It is used to detect hadronic energy that leaks through the main calorimeter. The forward calorimeter is placed at a distance of 11.2 m from the interaction point, close to the beam pipe. It covers the η range between 3.0 and 5.2 [55, 67].

In the schematic CMS detector slice (figure 3.6, displaying only the barrel region) the HCAL is displayed in yellow. The HO is not shown. The location of HF can be seen in figure 3.8.

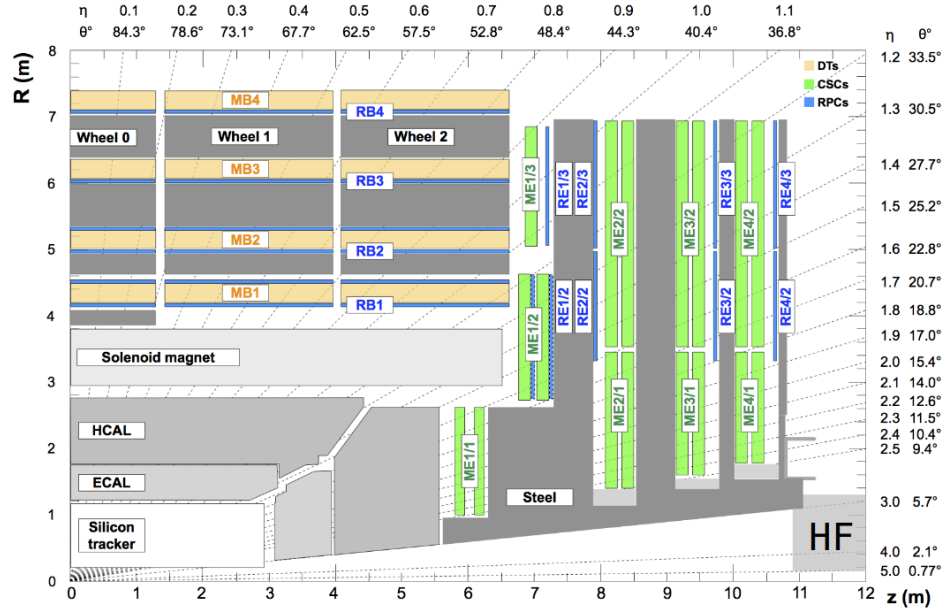


Figure 3.8: Slice through one quarter of the CMS Experiment. Both the barrel and the endcap region are shown. The different colours indicate the different detector types used in the muon system. Drift tubes are used in the barrel region and are shown in orange. Cathode strip chambers are used in the endcap and are shown in green. In both regions, resistive plate chambers are installed additionally. These are shown in blue. Figure adapted from Ref. [71] (added label for HF).

Muon System

The outermost detector layer is the muon system, dedicated to identifying muons and measuring their p_T . It is located outside the solenoid magnet inside the steel return yoke. Three types of gaseous detectors are used in the muon system. In the barrel region where the flux is low, drift tubes (DT) are used. In the endcaps cathode strip chambers (CSC) are used, as they are more suited to the high flux environment.

Both in the barrel and endcap region, a number of resistive plate chambers (RPC) are installed in addition to the DT and CSC detectors. While offering a lower spacial resolution, these chambers have a very fast response (~ 1 ns) and are used to precisely determine the correct bunch crossing for each detected muon.

In figure 3.6 the muon system is displayed in white and orange. A layout of the muon system with the locations of the different detector types can be seen in figure 3.8.

Trigger system

Depending on the filling scheme, collisions inside of CMS happen at a rate of up to 40 MHz. It is impossible to store all data that is produced. However, most collisions only contain soft QCD events that are not of interest to physics analyses. Therefore, the rate can be reduced to a number of events that can be saved by only selecting events that fulfil certain criteria that make them interesting to analysts. This selection is the task of the trigger system [72].

The CMS trigger system has two stages: the level 1 trigger (L1) and the high level trigger (HLT). The L1 trigger is a hardware based system using mostly programmable FPGAs [73]. It selects events based on information of the calorimeters and the muon system. The complete data from all subdetectors for up to 100 thousand events per second is kept in a buffer to be further analysed by the high level trigger. The HLT is a software based system running on a dedicated processor farm. There the events selected by L1 are reconstructed similarly as in offline analyses, and selected due to predefined criteria in different trigger settings. The final rate of events selected by HLT is of the order of several hundred events.

3.4 Luminosity Detectors

Several systems for measuring luminosity are present within the CMS Experiment, providing several independent rate measurements. This redundancy is necessary as without an associated measurement of the luminosity, the data collected by CMS cannot be used for cross section measurements. The differences between the measurements of the luminosity are used in the determination of the luminosity uncertainty. Three of the luminosity measurement systems, PLT, HF and BCM1F are also used for monitoring of the instantaneous luminosity during operation ('online').

In this section, a description of the different luminosity systems is given. In section 3.4.1 one of the systems, the BCM1F detector, is described in greater detail, as its calibration is a part of this thesis.

DT The DT luminosity measurement system, further called DT, uses the rate in the drift tubes in the muon system. In this region outside the solenoid, the hit rate is very low compared to the other luminometers. Therefore, the integrated rate over a 23 s time period is used [75]. As in the VdM scan only 30 s measurements are performed for each beam separation step, DT is too slow to be calibrated by this method and can therefore only be calibrated by comparison to a VdM-calibrated luminometer ('cross calibration').

HFOC/HFET Both the HFOC and the HFET luminosity measurements rely on data from the hadron forward calorimeter (HF), in an η range between 3.15 and 3.50.

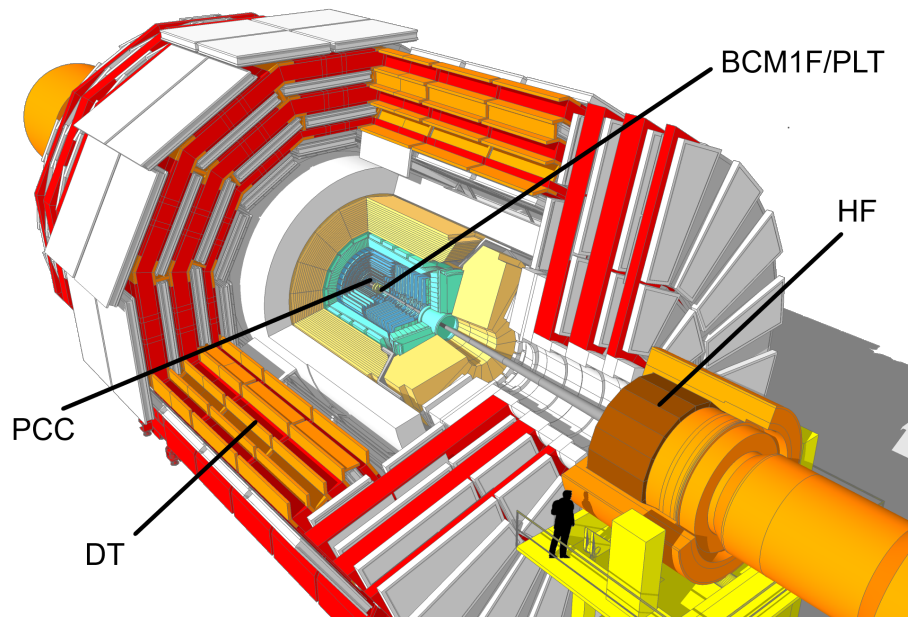


Figure 3.9: The CMS Experiment with the locations of the luminosity measurement systems. PCC uses data from the pixel tracker, HFOC and HFET use the hadron forward calorimeter and DT luminosity is calculated from data of the muon system. BCM1F and PLT are dedicated systems located around the beam pipe at 1.8 m distance from the interaction point. Adapted from Ref. [74] (Added luminometer labels).

Both measurements use data from a dedicated read-out system, providing data at the full 40 MHz sampling rate.

HFOC uses the zero counting algorithm [76], which counts the fraction of bunch crossings $p(0)$ that have no hit above a certain threshold. HFET measures the sum of the transverse energy that is deposited [75].

Despite small non-linearity and radiation damage effects, HFOC provided the best luminosity measurement for most of 2018.

PCC stands for pixel cluster counting. As the name implies, the method relies on counting the number of hit clusters in the pixel tracker in a bunch crossing. Due to the large amount of pixels, the occupancy is very low compared to the total amount of pixels. Hence, this method is expected to have an excellent linearity up to several times the achieved maximum instantaneous luminosity. Until late 2017 when hardware failures made this method unavailable, PCC was by default the best luminosity measurement.

As the read-out of PCC requires the CMS data acquisition system to be running, the measurement can not be used for online luminosity monitoring [77].

PLT The pixel luminosity telescope (PLT) is a dedicated system for measuring the luminosity. It is located at both sides at 1.8 m distance from the interaction point around the beam pipe, together with the BCM1F detector. On each side, eight so-called telescopes are installed. Each telescope consists of three pixel sensors in a row with 7.5 cm distance. Hits are only counted, if all three sensors of a telescope register the hit. This way, hits from random scattering are rejected. The rate of these triple coincidences can thus be assumed to be proportional to the luminosity [78].

3.4.1 BCM1F

The BCM1F detector [79] is located inside the barrel part of CMS around the beam pipe. It consists of two ring-shaped parts, which are placed at a distance of 1.83 m at each side of the collision point, on a common support structure with the PLT. An artistic depiction of the placement on one side can be seen in figure 3.10.

BCM1F measures both beam-induced background and luminosity. Its fast timing of 6.25 ns (four bins per bunch crossing) makes it possible to resolve single bunch crossings and to measure the beam-induced background in between two bunch crossings.

The version of the detector that is described here, was installed in the end-of-year shut-down between 2016 and 2017. This was necessary as high-voltage instabilities and unreliable detector operation of the version installed in 2015 made a replacement necessary.

Both detector rings consist of two separate half circles, so-called C-shapes, that are equipped with six sensors each, making a total of 24 sensors. The sensors are located at a radius of 7 cm. Each sensor has two read-out channels. A picture of a C-shape can

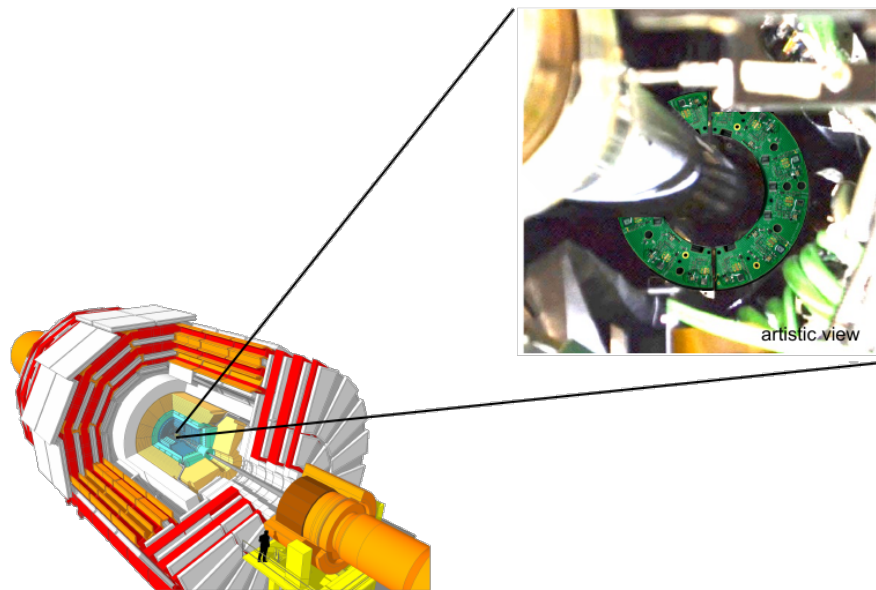


Figure 3.10: Artistic depiction of the placement of BCM1F. In the zoom-in at the top left, two C-shapes forming a ring around the beam pipe are shown. In reality, this would not be visible, as the support structures block the view. Adapted from Ref. [74].

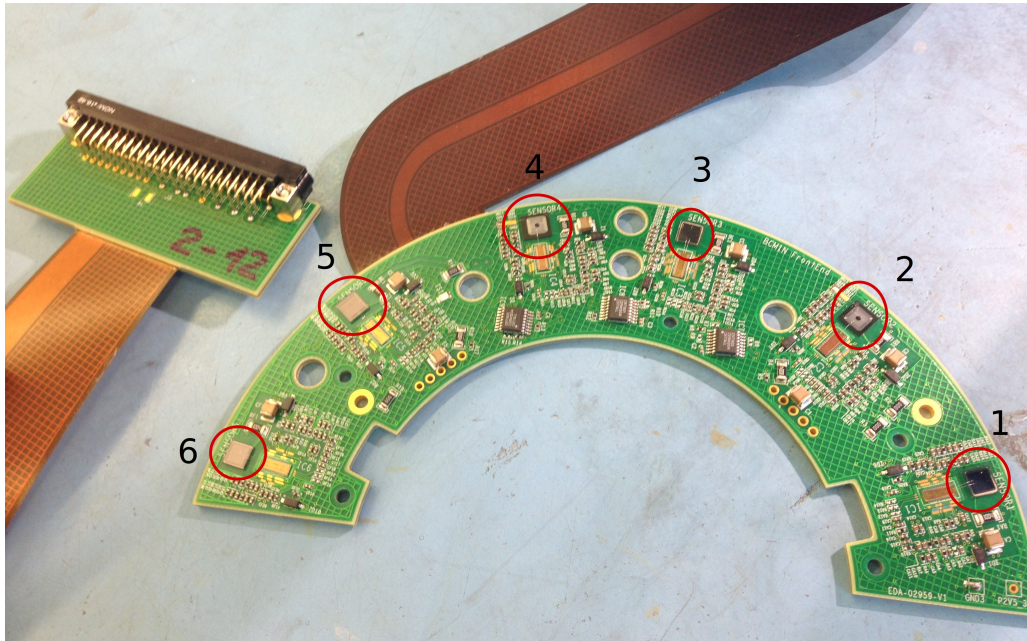


Figure 3.11: A C-shape of the BCM1F detector, as it was installed in 2017/18. The sensors are marked with red circles. Sensor number 6 on the left is a sCVD sensor, sensors 1, 3 and 5 are pCVDs and sensors 2 and 4 are silicon.

be seen in figure 3.11. Three different types of sensors were used in the replacement of BCM1F installed in 2017: four single-crystal diamond sensors (sCVD), ten poly-crystal diamond sensors (pCVD) and ten silicon sensors.

sCVD sensors were the sensor type used in the 2015/16 version of BCM1F. They were not expected to perform better than in the original version and were only installed for comparison purposes. As it was expected, they ceased to function after only a short period of time.

pCVD sensors were chosen to replace the sCVD sensors as the main source for luminosity measurement in the 2017/18 version of the detector. They are expected to show a more stable behaviour, while also keeping the advantages of diamond sensors. Diamond sensors are both reliable and radiation hard. They have very low leakage currents and do not require cooling. However, in operation, the efficiency of the pCVD sensors was observed to be dependent on the rate of incoming particles. This effect needs to be compensated by calibration. The necessary calibrations have been done as a part of this thesis and are described in chapter 5.

Silicon sensors are diodes connected in reverse direction. They are also radiation hard and reliable, but compared to diamond sensors, they suffer from drawbacks in the

given setup. Silicon sensors, in contrast to diamond sensors, suffer from increased leakage current with irradiation. To keep the leakage current under control, cooling of the sensors is required. However, cooling is only available indirectly due to BCM1F being located inside the cooled tracker system (about -10°C). This leads to high leakage currents. Due to the lack of cooling and a problem with the circuit boards, only one of the ten silicon sensors proved to be functional.

Due to the leakage currents saturating the electronics, the sensor ceased to function in June 2018. Before this, however, the measurements showed excellent linearity and were used as a calibration source for the pCVD sensors.

RECONSTRUCTION ALGORITHMS

Particles as well as their properties are reconstructed from the electronic signals in the different detector systems. In CMS the reconstruction is performed centrally, using various highly sophisticated reconstruction algorithms to determine positions, energy and momenta of the particles. The algorithms for analysis objects, that are of relevance for the analysis in this thesis, are described in this chapter. In sections 4.1 and 4.2 the reconstruction of tracks and vertices and the particle-flow algorithm are described. These two methods are the basis for all following reconstruction methods. Section 4.3 describes the reconstruction of jets, with special focus on boosted jets (fatjets) and b jet identification. The identification of leptons is discussed in section 4.4, and section 4.5 covers the reconstruction of missing transverse energy. In the last section, a brief description of event shape variables is given. These variables assign a value to each event based on the number and distribution of jets. They are used as inputs for the Deep Neural Network used in the main analysis of the thesis.

4.1 Tracks and Vertices

A crucial task for the analysis of CMS data is the reconstruction of charged-particle trajectories, so-called tracks, from signals in the tracking system. Tracks are used to determine both the momentum of charged particles and the charge. The algorithm must meet high requirements for precision and speed.

The first step in reconstructing tracks is to reconstruct particle hits from the electronic signals from the tracker systems. A pixel hit is defined as a number of adjacent pixels that together collect an amount of charge above a threshold. In the strip tracker, a hit is defined as one strip with a signal five times as high as the background noise, or two adjacent strips with more than two times the background each. This threshold is chosen to be as sensitive as possible while still excluding signals from electronics noise [80].

Tracks are reconstructed from the hits using the Combinatorial Track Finder (CTF), which is an adaptation of the Kalman filter technique [81], developed for CMS. The tracking is done in several steps: first a track seed is chosen. A track seed consists of

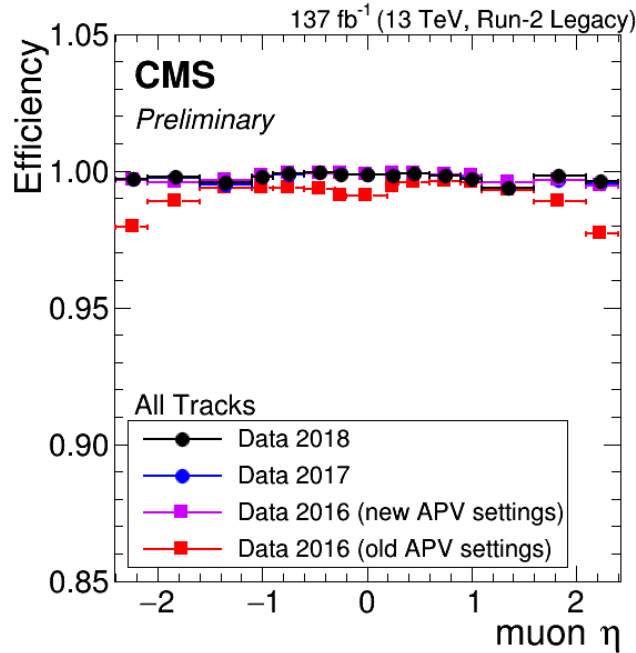


Figure 4.1: Efficiency of the track reconstruction for muon tracks as a function of η . Figure taken from Ref. [82].

either two or three pixel hits, originates from close to the beam spot (the area where the two beams collide), and has a p_T greater than a chosen threshold. In a second step, the seed trajectory is extrapolated, and further candidate hits are assigned as belonging to the track. The selected hits are then fitted in the third step, determining the best-fit values of the track parameters. In the last step, quality criteria are applied, and based on these, the track is either selected or discarded [80].

These four steps are iterated several times. After each iteration, the hits associated to the final tracks are removed, reducing the complexity of the procedure for the tracks reconstructed in following iterations. For each iteration, the seed criteria are loosened, to allow for more possible tracks.

Reconstruction efficiencies vary for different kinds of charged particles, the track p_T , the η region of the track, and also the data-taking period, due to changes in the tracker geometry. While in the barrel region, more than 90% of the tracks with a p_T above 1 GeV are reconstructed, the efficiencies in the endcaps and for low p_T tracks can be smaller [80]. The track reconstruction efficiency for muon tracks, as a function of η , in the four different data-taking periods can be seen in figure 4.1. Interaction vertices are reconstructed from tracks that satisfy certain quality criteria. These tracks are clustered into groups coming from the same proposed vertex, using the z -coordinate of the track at the point of closest approach to the collision area, also referred to as beam spot. All vertices with at least two

tracks are then fitted using the adaptive vertex fitter algorithm [83]. The achieved vertex resolution depends on the number of tracks associated to the vertex. It ranges between about $10 \mu\text{m}$ (≥ 40 tracks) to approximately $150 \mu\text{m}$ (≤ 5 tracks) [80].

A high number of proton-proton collisions occur in each bunch crossing, leading up to about 40-60 interaction vertices in each event. The vertex with the highest p_T sum of all associated tracks is defined as the primary vertex of the event [84]. All other vertices are called pileup vertices.

4.2 Particle-flow

The information provided by the different subsystems of the CMS detector is combined using the particle-flow algorithm [85] to provide a global event description. The algorithm provides a list of candidate final state particles, including leptons, photons and charged and neutral hadrons, by using the combined information of all detector subsystems. This approach significantly improves particle identification and energy resolution compared to a non-correlated approach, as well as the identification of particles originating from pileup. The algorithm starts with so-called particle-flow elements: the reconstructed signals in the subdetectors, like tracks in the tracker and muon systems and energy clusters in the calorimeters. The elements are linked to form so-called particle-flow blocks using specific criteria. Tracks in the tracker are linked to calorimeter clusters based on their extrapolated trajectory, and clusters in ECAL and HCAL are linked based on their position in the $\eta - \phi$ - plane. Tracks in the tracker are also linked to tracks in the muon system. Each established link is assigned a number that provides a measure of the quality of the link. The linked particle-flow elements form so-called particle-flow blocks. The blocks are then used to reconstruct the particle-flow candidates.

4.3 Jet Reconstruction

Due to the confinement of the strong interaction, particles carrying colour charge created in the hard proton-proton interactions are not detectable directly. Instead, colour-charged particles produce bundles of charged and neutral particles, the so-called jets, which are detected in the final state of the event. Due to the high multiplicity of particles in an event (from pileup, other jets, or prompt particles), reconstructing jets is a difficult task requiring highly sophisticated methods.

Algorithms that cluster jets from single particles should satisfy two important criteria: infrared safety and collinear safety. An algorithm is infrared safe if the addition of an arbitrary amount of ultra-soft particles does not change the result. Collinear safety means that the splitting of one constituent into two cannot change the outcome. There are two kinds of jet algorithms: cone algorithms (e.g. [87]), which cluster particles inside a

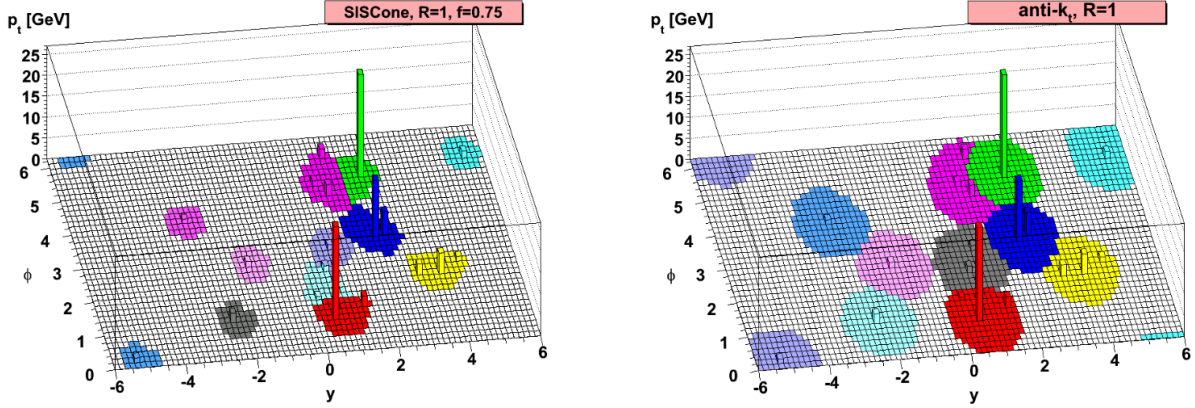


Figure 4.2: Reconstructed jet areas using the SISCone cone jet algorithm (left) and the anti- k_T algorithm (right). Due to the transverse momentum being applied inversely, anti- k_T also creates cone-like jets around hard particles. Adapted from [86].

certain cone, and sequential recombination algorithms, which cluster particles recursively depending on an algorithm-specific distance parameter.

Jets for the analysis are clustered from particle-flow candidates using the anti- k_T algorithm [86]. The anti- k_T algorithm is a sequential recombination algorithm, that uses the distance parameter d_{ij} :

$$d_{ij} = \min(k_{t,i}^{-2}, k_{t,j}^{-2}) \frac{\Delta R_{ij}^2}{R^2}, \quad (4.1)$$

with the transverse momenta of two particles $k_{t,ij}$, the distance in η and ϕ between the particles $\Delta R_{ij} = \sqrt{\Delta\phi^2 + \Delta\eta^2}$ and the chosen radius parameter R .

This algorithm starts by clustering the two particles with the smallest d_{ij} into a single object. It then proceeds recursively by clustering the objects with the next smallest d_{ij} . The algorithm stops, when the distance of the clustered object to the beam, d_{iB} ,

$$d_{iB} = k_{t,i}^{-2} \quad (4.2)$$

is smaller than the d_{ij} to any other object. The final clustered object is then defined as a jet and removed from the collection of particles. The algorithm then proceeds with the remaining objects.

Since the transverse momentum of the particles is taken into account inversely, the d_{ij} between two soft particles will be high and soft particles will be more likely clustered to nearby hard particles than to each other. This leads to cone-shaped jets around the hardest particles in the event¹. In the schematic depiction, shown in figure 4.2, it can be seen that the anti- k_T algorithm leads to cone-like jets.

¹Other recursive jet clustering algorithms like the Cambridge-Aachen or the k_T algorithms lead to irregularly shaped jet areas

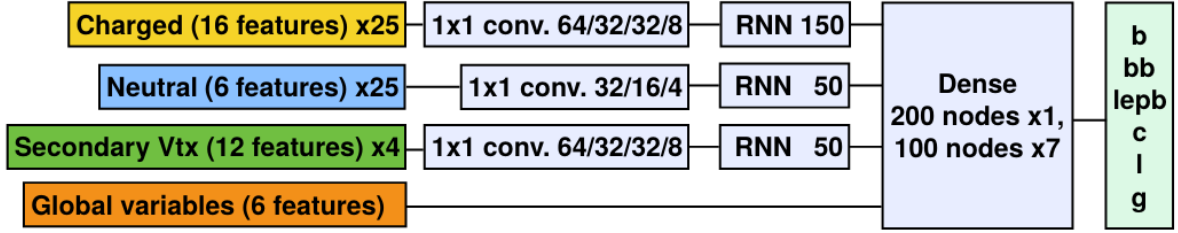


Figure 4.3: The network architecture of DeepJet. Input features from the 25 most important charged and neutral particle-flow candidates and from secondary vertices are preprocessed to remove dependencies on transverse momentum and pseudorapidity, and to transform them to an optimal input shape for the neural network. The classification is performed together with the global variables using a dense neural network with seven layers. Figure taken from Ref. [90].

The anti- k_T algorithm is the standard algorithm used in CMS for Run 2 data. For CMS Run 2, standard jets are clustered with a radius parameter R of 0.4 (AK4 jets).

Pileup mitigation Before clustering particle-flow candidates into jets, particles coming from pileup interactions are removed. The approach used for AK4 jets is called Charged Hadron Subtraction (CHS). All charged hadrons that are associated to pileup vertices due to their tracks are removed from the event prior to clustering [88].

Jet Energy Corrections To reconstruct the properties of the parton that created the jet, several corrections are applied to the jet properties. This happens for several reasons. Firstly, the detector response is not perfectly uniform and linear and neutrinos cannot be detected. Also, a pileup-dependent correction needs to be applied, as CHS only removes charged hadrons and disregards contributions from neutral particles. Jets in simulated data also need to be corrected for differences between the experimental data and the simulation. These corrections are applied to the p_T and η of the reconstructed jets. Their uncertainties are amongst the most important uncertainties for analyses using multi-jet final states [89].

Another important quantity for jets is the p_T resolution. It ranges from about 5% for high p_T jets to about 20% for soft jets. For simulated jets the resolution is better, and simulated jets are artificially smeared to correct the simulation such that it describes the actual data [89].

4.3.1 b tagging

In top-quark analyses, the identification of jets originating from b quarks (b jets) is an essential ingredient, as top quarks almost exclusively decay into a b quark and a W boson. The distinction between b jets and jets originating from light quarks is made possible by the comparatively long lifetime of b quarks. The B hadrons resulting from the hadronisation of the b quarks travel distances of the order of a millimetre, creating a secondary vertex. Due to their high mass, the B hadrons carry a large part of the momentum of the initial fragmentation process. The hard fragmentation provides another criterion that differentiates light jets from b jets.

Simple b-tagging algorithms count the number of displaced tracks or calculate a probability for the presence of a secondary vertex [91]. In recent years, during the second run period of the LHC, sophisticated deep learning algorithms have become the standard for b-tagging.

The b-tagging algorithm that is used for the analyses in this thesis is called DeepJet [90]. DeepJet is a deep learning algorithm that uses more than 600 input features. Unlike earlier deep learning b-tagging algorithms, like DeepCSV [92] which use only track and vertex information that pass stringent quality criteria, DeepJet uses information from all tracks and vertices in the jet as well as global event variables.

A schematic of the neural network structure of DeepJet can be found in figure 4.3. The input features are separated into four groups: features from charged and neutral particle-flow candidates, features from secondary vertices and global variables. Features from the first three groups are preprocessed to remove dependencies on transverse momentum and pseudorapidity, and to transform them to an optimal input shape for the neural network. The classification is performed together with the global variables using a dense neural network with seven layers. The output consists of six different output classes, describing the compatibility of the input jet with b jets, c jets (jets originating from c quarks) or light jets. The b jets are further classified into hadronic and leptonic B hadron decays, as well as double b jets (jets with two B hadrons). Light jets are classified into light (uds) jets and gluon jets. For this thesis, the main focus of interest is the b jet classification provided by DeepJet. The classifier attributes a value between zero and one to each jet. A higher value means that the jet is more likely to be a b jet. To classify jets, a cut value has to be chosen above which each jet is labelled a b jet. These cut values are chosen by their respective mistag rate, meaning the fraction of light and c jets that are falsely classified as b jets.

The three working points usually chosen for b-tagging are "loose" (10% mistag rate), "medium" (1% mistag rate) and "tight" (0.1% mistag rate). The efficiency of correctly labelled jets is dependent on the transverse momentum. In figure 4.4 the efficiencies for the three working points of DeepJet and DeepCSV are shown ranging from a jet p_T of zero to 800 GeV. For the medium working point of DeepJet, that is used in this thesis, the efficiency is about 80% in the most relevant p_T range.

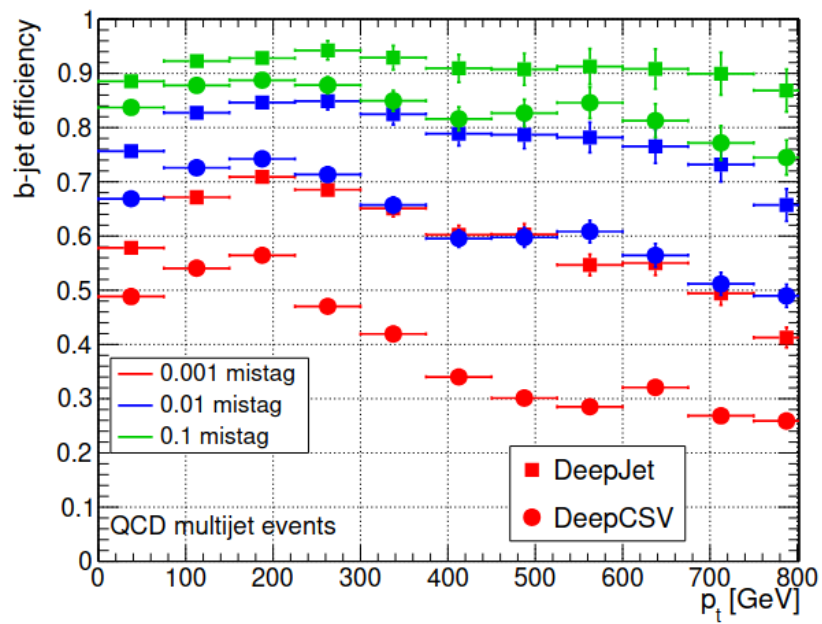


Figure 4.4: The p_T dependent tagging efficiencies for DeepJet (quadratic markers) and DeepCSV (round markers). The loose, medium and tight working points are shown in green, blue and red, respectively. Figure taken from Ref. [90].

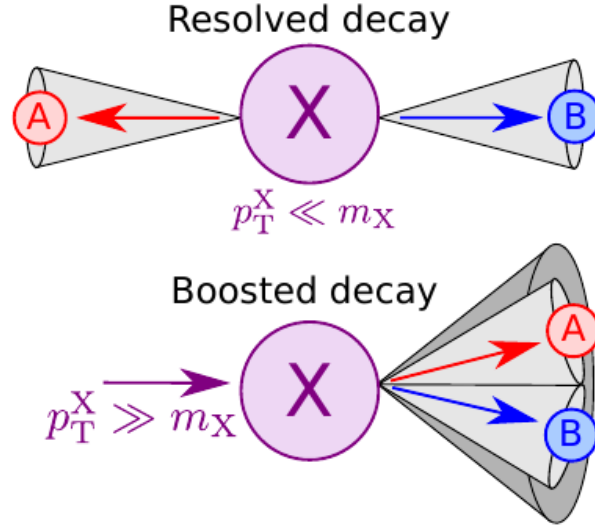


Figure 4.5: Systematic depiction of a particle X decaying into two jets A and B, in the resolved regime (top) and in the boosted regime (bottom). A boosted jet (dark grey) is formed when the two jets are merged through the boost. Figure taken from Ref. [93].

As the simulation does not match the data with perfect accuracy, b-tagging efficiencies differ between real data and simulation. These differences are taken into account via scale factors – multiplicative factors that are applied to the weight of the simulated events for each present jet.

4.3.2 Boosted jets

Vector bosons and top quarks can decay into final states with several quarks. If the p_T of the original particles is high (above 200 GeV for vector bosons), the two (or three for top quarks) jets from the decay cannot be reconstructed as separate jets using the standard AK4 jets, as the two jets are overlapping in the detector. To reconstruct this kind of objects, wider jets, so-called boosted jets or fatjets, are used. The two or three jets from the final state particles are reconstructed as one composite jet. For boosted jets, like for standard jets, the anti- k_T algorithm is used. The radius parameter is increased to a value of 0.8 (AK8 jets).

Pileup mitigation for boosted jets is done using a different method than for standard jets. Instead of CHS, the algorithm PileUp Per Particle Identification (PUPPI) [94] is used. The PUPPI algorithm calculates a weight for each particle. In an ideal case, a particle from the primary vertex would get a weight of one, while a particle from the pileup would

get a weight of zero. The weight is applied to the p_T of each particle. For the calculation of the weights, a shape parameter α is calculated for all particles. Charged particles can be associated to pileup through tracking. The distribution of the α of these particles is calculated. Pileup particles usually have an α within a few standard deviations of the mean of the α distribution. Therefore, a particle's weight can be calculated using the distance of their α and the mean of the pileup α distribution. As a final correction, all particles with a weight w below a threshold w_{cut} are removed. The jet clustering algorithm is applied to the corrected set of particles.

4.3.3 Boosted Jet Tagging

Boosted jets can originate from a variety of origins: hadronically decaying high p_T vector bosons, Higgs bosons and also hadronically decaying top quarks, where the W boson jet is in addition superimposed by the b jet from the top quark. They can, however, also originate from the superposition of QCD jets. The correct assignment (tagging) of the origin of a boosted jet provides insights into processes involving hadronically decaying bosons, since the reconstruction of a hadronically decaying boson from resolved jets is generally a difficult task, due to a multitude of combinatoric possibilities of the different jets².

A comparatively simple approach to the tagging of boosted vector boson jets is the use of the so-called "subjettiness" observable, τ_N [95]. The observable τ_N indicates the compatibility of a jet with the hypothesis of a jet with exactly N subjets. τ_N is calculated by:

$$\tau_N = \frac{1}{d_0} \sum_k p_{T,k} \min \{ \Delta R_{1,k}, \dots, \Delta R_{N,k} \} \quad (4.3)$$

with the normalisation parameter $d_0 = \sum_k p_{T,k} \Delta R_0$ and the distance of the i -th subjet to the k -th jet constituent particle $\Delta R_{i,k}$. A hadronically decaying boson is expected to form a two-prong jet with a low τ_2 compared to its τ_1 . For boosted boson tagging, the combined variable $\tau_{21} = \tau_2/\tau_1$ is used. Distributions of this variable for boson jets and QCD jets can be seen in figure 4.6. The shape and mean of the distributions for bosons differs significantly from the distribution from QCD. However, the subjettiness cannot provide a good differentiation between W and Z bosons, both of which have a substructure comprising two subjets.

In order to distinguish between bosons, the mass of the jet can be analysed or Higgs or Z bosons decaying into two b-quarks can be identified via boosted jet b-tagging (for example with the multivariate double b tagger [97]). The best distinction, however, is reached using sophisticated neural network algorithms. These algorithms can use high level inputs (such as τ_{21} or the mass of the jet), or low level inputs (such as the four-vectors of the particle-flow candidates constituting the jet). At the present day, algorithms using

²It can be done with b jets, as it is for example done in Ref. [20].

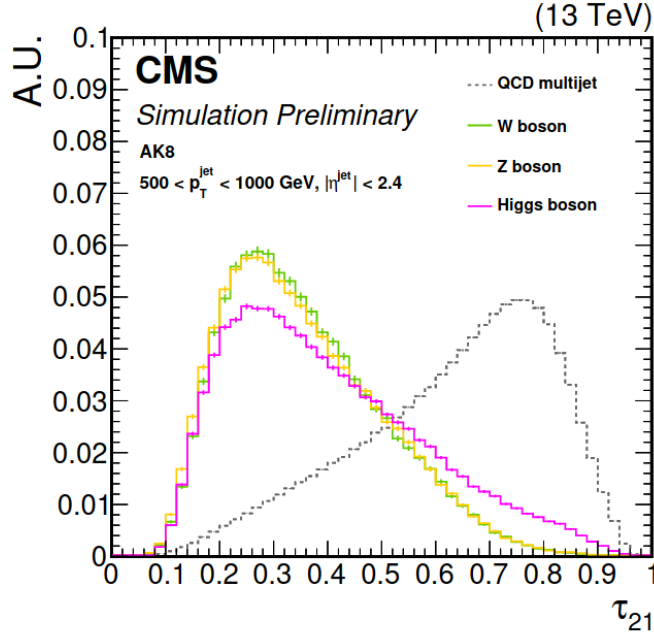


Figure 4.6: The distributions of τ_{21} for W, Z and Higgs bosons, as well as for QCD jets. The distributions show a significant difference between bosons and QCD. Taken from Ref. [96].

low level inputs have shown better performance. One of these algorithms is DeepAK8 [96]. Similar to DeepJet (section 4.3.1), DeepAK8 uses the variables from the 100 hardest particles (ordered by p_T) as well as secondary vertex information. The output classes are divided into W, Z, H, t or QCD jets. Each output class is subdivided into the corresponding decay modes for each particle (e.g. $Z \rightarrow b\bar{b}$, $Z \rightarrow c\bar{c}$ etc.). The full list of output classes can be taken from table 4.1.

The best performance in the differentiation of boosted jets is provided by ParticleNet [98]. While ParticleNet provides the same output classes as DeepAK8, a different approach of inputs and network architecture is used. ParticleNet treats the input particle-flow candidates as an unordered cloud of particles, analogous to a point cloud in 3D image recognition. Following this approach, the network architecture is also developed from image recognition techniques. The input features for each particle only include spatial p_T and energy information. No further inputs are used.

With this approach, ParticleNet outperforms all other boosted jet taggers. Comparisons of the receiver operator characteristics of different boosted jet taggers can be seen in figure 4.7. In figure 4.7(a) and 4.7(b) the performance of DeepAK8 is compared to other tagging algorithms for top quarks and for Z bosons. It is shown that DeepAK8 outperforms all other algorithms both for top and Z tagging. In figure 4.7(c) the performance for top tagging of DeepAK8 is compared to the performance of ParticleNet. Even though the p_T

Table 4.1: The output classes of DeepAK8/ParticleNet. The primary output classes W, Z, Higgs, Top and QCD are subdivided into their respective decay modes.

Class	Higgs	Top	W	Z	QCD
Subclasses	H \rightarrow b \bar{b}	t \rightarrow bcq	W \rightarrow cq	Z \rightarrow b \bar{b}	QCD(bb)
	H \rightarrow c \bar{c}	t \rightarrow bqq	W \rightarrow qq	Z \rightarrow c \bar{c}	QCD(cc)
	H \rightarrow VV(qqqq)	t \rightarrow bc		Z \rightarrow q \bar{q}	QCD(b)
			t \rightarrow bq		QCD(c)
					QCD(others)

range of the performance plots is different, ParticleNet is shown to outperform DeepAK8. As the best tagging performance also for Z bosons is to be expected from ParticleNet, it is chosen as the boosted jet tagger used in the analysis of this thesis.

4.4 Lepton Identification

Leptons are taken from particle-flow candidates. However, the purity of the reconstructed leptons is not good enough when using solely the particle-flow algorithm. Backgrounds to the leptons can arise from misidentified hadrons, from photon splitting or from leptons created in jets in the decays of b and c quarks. Therefore, for most physics analyses additional criteria – the so-called lepton IDs – are applied.

Several different IDs, using sequential requirements (cuts) or MVA methods are available within CMS. For this thesis, cut-based IDs are used to identify leptons.

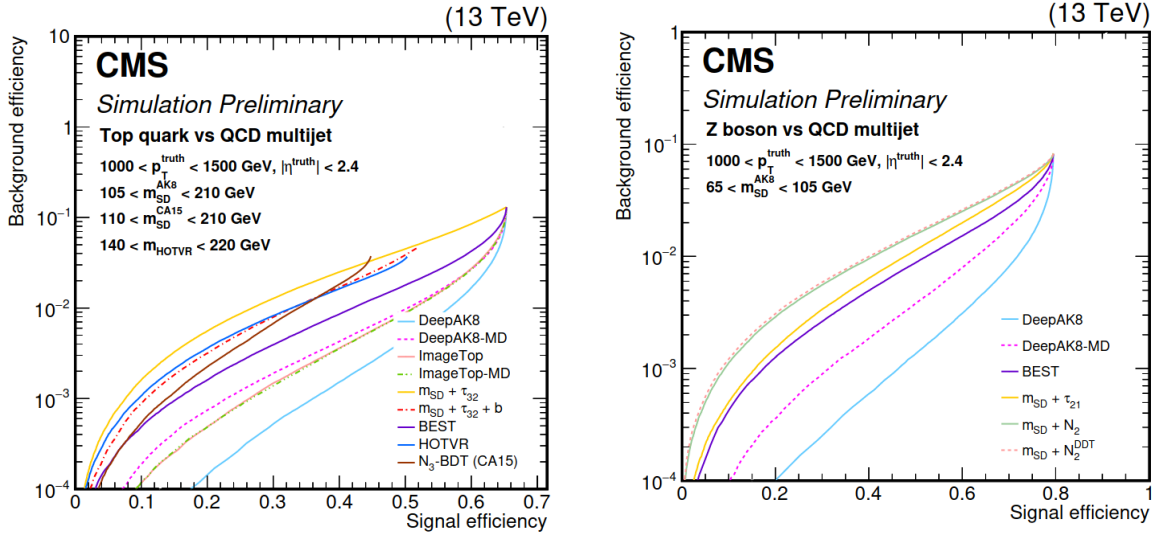
4.4.1 Electrons

The cut-based electron ID was developed using data from the year 2017 and is valid for all three data-taking years of Run 2. Seven variables are used to create the ID. These include isolation criteria, criteria stemming from the shape of the electromagnetic shower in the ECAL as well as information from tracking.

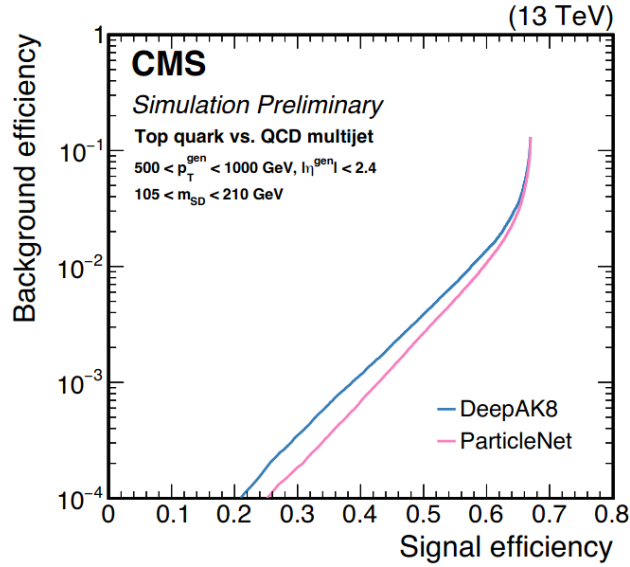
The isolation I is defined as the sum of the transverse momenta of particle-flow candidates inside a cone of $\Delta R < 0.3$ around the electron candidate. For the ID, the combined isolation divided by transverse energy of the electron is used:

$$I_{\text{combined}}/E_T = (I_{ch} + \max(0, I_n + I_\gamma - I_{PU}))/E_T, \quad (4.4)$$

with the I_{ch} , I_n, I_γ originating from charged and neutral hadrons and photons respectively. I_{PU} corrects for pileup and is dependent on the number of colliding protons in the event. Criteria on the ECAL shower include the hadronic over electromagnetic energy ratio (H/E). H is defined as the energy deposited in the HCAL in a cone of $\Delta R < 0.15$ around



(a) Different top tagging algorithms. Figure (b) Different Z tagging algorithms. Figure taken from Ref. [99].



(c) The performance of DeepAK8 and ParticleNet for top tagging. Figure taken from Ref. [100].

Figure 4.7: Receiver operator characteristics for different tagging algorithms. The figures at the top show performances for all commonly used boosted jet taggers for top tagging (left) and Z boson tagging (right). In both cases, DeepAK8 shows the best results. The bottom plot shows the performance for ParticleNet for top tagging, compared to DeepAK8. ParticleNet outperforms DeepAK8.

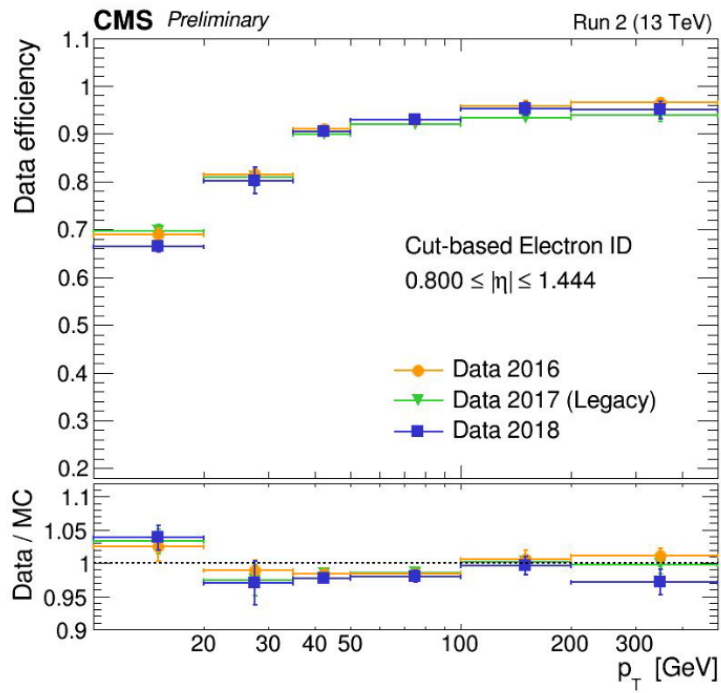


Figure 4.8: The electron reconstruction efficiency using the loose working point of the cut-based electron ID, in the barrel region. The three data-taking years are shown in orange (2016), green (2017) and blue (2018). The ratio plot in the lower part of the figure shows the differences between data and simulation. Taken from Ref. [101].

the electron candidate, E is the reconstructed energy of the electron candidate.

To veto electrons created by photon splitting in the tracker, all electrons passing the ID must have a hit in the first pixel layer. These, as well as the remaining variables, are described in more detail in Ref. [102].

Four different working points of the ID are customarily used within CMS. These include the 'veto' working point at 95% efficiency as well as 'loose', 'medium', and 'tight' working points at approx. 90%, 80% and 70% efficiency, respectively. The p_T dependent efficiency using the loose working point can be seen in figure 4.8.

As for b-jet efficiencies, the electron reconstruction efficiency using the ID differs between data and simulation. These differences usually range between 1 and 5% and are corrected using scale factors.

4.4.2 Muons

Muons can be reconstructed either as 'tracker muons' or as 'global muons', very often as both. Tracker muons are reconstructed starting from a track in the tracker systems. The track is extrapolated to the muon system. It is attributed to a tracker muon, if at least one muon segment hit matches the track. Tracker muons with only one hit in the innermost layer of the muon system are often misidentified, as these hits can originate from remnants of hadronic showers.

Global muons are reconstructed starting from a reconstructed track in the muon system. This track is extrapolated back to the tracker and matched with the corresponding tracker track. A combined fit is performed to find the combined muon track [71].

The loose muon ID only requires the muon to be reconstructed as a tracker muon or a global muon. This allows for a small amount of misidentified hadrons to pass the ID.

For the medium muon ID, all loose muons are selected, and additional criteria are applied: the track must have hits in 80% of the tracker layers and the compatibility between the tracker track and the muon system hits must be greater than a certain value. This value is chosen to provide an efficiency of the medium muon ID of 99.5%. For global muons to pass the medium muon ID, the compatibility criterion is looser. However, the combined fit is required to pass goodness-of-fit criteria to reach the desired efficiency.

A tight muon must be reconstructed both as a tracker muon and as a global muon with stringent criteria both on the number of hits in the tracker and muon systems and goodness-of-fit tests. In addition, cuts on the impact parameters (the closest approach to the primary vertex) are applied to veto muons originating from hadron decays in flight.

For the analyses in this thesis, the medium muon ID is used. The efficiency of this ID as a function of the muon p_T can be seen in figure 4.9. The ID is optimised to provide an average efficiency of 99.5%. The data-to-simulation agreement is very good, and all scale factors are within $\sim 1\%$ of unity.

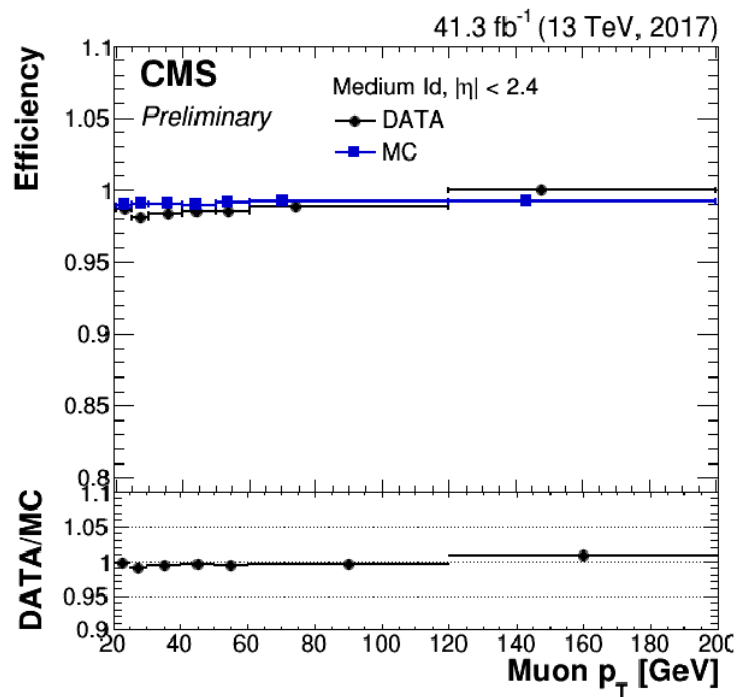


Figure 4.9: The efficiency of the medium muon ID for the data-taking year 2017 as a function of the transverse momentum of the muon. The performance in data is shown in black, the performance in simulation is shown in blue. Data-to-simulation agreement is shown in the bottom part of the figure. Taken from Ref. [103].

4.5 Missing Transverse Momentum

Weakly interacting neutral particles do not interact with the detector material, and therefore escape the detector undetected. In the standard model, this is the case for neutrinos. Many beyond the standard model theories also postulate undetectable stable particles, for example the hypothetical lightest supersymmetric particle [104]. This makes the indirect measurement of undetectable particles a highly important task, both for standard model analyses as well as for searches for new physics.

The indirect detection of undetectable particles is made feasible through the measurement of 'missing transverse momentum', p_T^{miss} . Missing transverse momentum is defined as the negative vectorial sum of all particle-flow candidates in the event [105]:

$$\vec{p}_T^{miss} = - \sum_i \vec{p}_{T,i} \quad (4.5)$$

In collisions, the vectorial sum of the transverse momenta of all collision products is required to be zero. Some particles escape detection, for example because of p_T and energy thresholds. This leads to inaccuracies in the measurement of p_T^{miss} .

4.6 Event Shape Variables

Event shape variables describe the geometrical distribution of particles and energy in an event. For the analysis in this thesis, event shape variables describing the distributions of jets are used.

Traditional event shape variables are based on the Sphericity tensor [106],

$$S^{\alpha\beta} = \frac{\sum_i p_i^\alpha p_i^\beta}{\sum_i \vec{p}_i^2}, \quad (4.6)$$

with the \vec{p}_i being the four-vectors of the jets in the event and α and β being indices of their x, y and z components. This tensor has three eigenvalues, $\lambda_{1,2,3}$ (ordered from high to low value), with $\lambda_1 + \lambda_2 + \lambda_3 = 1$. These eigenvalues are used to calculate the event shape variables:

- Sphericity S :

$$S = \frac{3}{2}(\lambda_2 + \lambda_3) \quad (4.7)$$

- Aplanarity A :

$$A = \frac{3}{2}\lambda_3 \quad (4.8)$$

- C :

$$C = 3(\lambda_1\lambda_2 + \lambda_1\lambda_3 + \lambda_3\lambda_3) \quad (4.9)$$

- D :

$$D = 27\lambda_1\lambda_2\lambda_3 \quad (4.10)$$

Another class of event shape variables are the Fox-Wolfram-Moments $H(l)$ [107]. The Fox-Wolfram-Moments describe the distribution of jets using spherical harmonics:

$$H(l) = \sum_{ij} \frac{|\vec{p}_i||\vec{p}_j|}{E_{vis}^2} P_l \cos(\theta_{ij}), \quad (4.11)$$

with the visible energy in the event E , the l -th Legendre polynomial P_l and the angle θ_{ij} between jets i and j .

Part II
Luminosity Studies

CALIBRATION OF THE BCM1F DETECTOR

In this chapter calibrations for the Fast Beam Condition Monitor (BCM1F) detector, described in section 3.4 are shown. The calibrations described in this chapter correct for two kinds of effects:

- Non-linearity effects describe a direct dependency of the visible cross section σ_{vis} on the incoming hit rate. This dependency is affected by the filling scheme. With fewer bunches and/or larger gaps between them, a lower non-linearity effect is observed.
- Long-term changes in the detector efficiency can occur due to radiation damage in sensors and read-out electronics.

After an introduction to measurement methods with BCM1F in section 5.1, corrections for non-linearity effects are shown in section 5.2. Corrections are developed for the two years in which this version of BCM1F was used: 2017 and 2018. Due to differences in the availability of suitable calibration sources, different approaches are used for the two years. The methodology developed for 2018 is discussed in section 5.2.1. The corrections for 2017 are discussed in section 5.2.4.

The second type of corrections, for long-term detector effects, is shown in section 5.3. In section 5.4, the results of the calibration are discussed and the final corrected luminosity measurement is compared to the measurements from before the calibration and to the best known luminosity measurement by the other luminometers.

The calibrations presented in this chapter were implemented in the online data-taking to improve the online luminosity measurement, and will be published in Ref. [108].

5.1 Measurement of Instantaneous Luminosity with BCM1F

The BCM1F detector measures the instantaneous luminosity by counting hits from charged particles. The number of hits is defined as an average over a chosen set of active channels that are selected from the 48 channels of the detector. In this study, only the 20 channels equipped with pCVD sensors (see section 3.4.1) are used. During the data-taking year 2017 and the first part of 2018, until the VdM scan in July 2018, all pCVD channels were active. For the later part of 2018, six channels were masked due to technical effects such as low efficiency or strong turn-on effects. The calibrations described in this chapter only refer to the luminosity that is measured using the active channels.

The visible cross section σ_{vis} , that is needed to calculate the instantaneous luminosity from the rate of hits in the detector, is measured in a Van der Meer (VdM) scan, as described in section 3.2.1 [64]. VdM scans are typically performed only once per data-taking period. However, σ_{vis} can change over time due to radiation damage and other hardware effects. Inefficiencies at high rate reduce σ_{vis} , making it dependent on the instantaneous luminosity.

An important method to track these changes are so-called emittance scans, short VdM-like scans, performed at the beginning and also at the end of each fill, to determine changes in σ_{vis} during the data-taking, for example due to the change in instantaneous luminosity. During Run 2, emittance scans consist of nine steps of different beam separation both in x and y direction, and can be used to measure σ_{vis} with a precision of about 3-5% [109]. A measurement of the instantaneous luminosity during a fill and an emittance scan can be seen in figure 5.1. By comparison of emittance scan results for different fills, long-term changes of the detector's σ_{vis} can be tracked.

As for other luminometers (see section 3.4), the rate measurement to determine the luminosity does not count hits directly. Instead, the so-called occupancy μ_b is used [110]:

$$\mu_b = -\ln\left(1 - \frac{N_b}{N_{\max}}\right), \quad (5.1)$$

with the number of hits N_b in one bunch crossing and the maximum possible number of hits N_{\max} . This allows for the estimation of double hits in one sensor, which can't be measured directly, as μ_b can be interpreted as the mean μ of a Poisson distribution. The use of this method (also called zero-counting) therefore is preferable for a high rate environment.

From the occupancy, the single bunch instantaneous luminosity, SBIL, can be calculated via:

$$L_b = \frac{f_{\text{LHC}}}{\sigma_{vis}} \mu_b, \quad (5.2)$$

with the revolving frequency of the LHC f and the visible cross section of the luminometer. The efficiency correction ϵ applied as a factor to σ_{vis} . The non-linearity correction ρ is

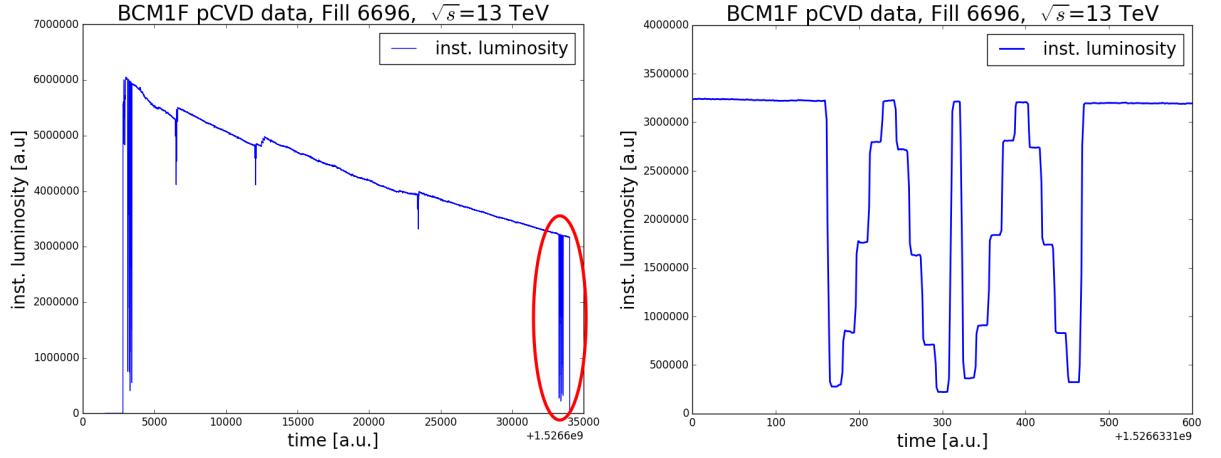


Figure 5.1: The instantaneous luminosity during one fill of the LHC (left) and a zoom in to the emittance scan (marked with the red ellipse) at the end of the fill (right). The beams are separated in nine different steps leading to a corresponding change in instantaneous luminosity, first in X direction, then in Y direction.

applied as a linear dependency on the luminosity. The corrected $\sigma_{vis}(L)$ is therefore

$$\sigma_{vis}(L) = \rho \cdot L + \epsilon \cdot \sigma_{vis,0}. \quad (5.3)$$

Using this term, the occupancy μ_b becomes

$$\mu_b = \frac{\sigma_{vis}(L)}{f_{LHC}} \cdot L_b = \rho \cdot \left(\frac{\sigma_{vis,0}}{f_{LHC}} \right)^2 \cdot L_b^2 + \epsilon \cdot \left(\frac{\sigma_{vis,0}}{f_{LHC}} \right) L_b. \quad (5.4)$$

Solving this equation for L_b results in the final corrected measurement of the SBIL [110]:

$$L_b = \rho \cdot \left(\frac{f_{LHC}}{\sigma_{vis,0}} \right)^2 \cdot \mu_b^2 + \epsilon \cdot \left(\frac{f_{LHC}}{\sigma_{vis,0}} \right) \cdot \mu_b. \quad (5.5)$$

The determination of the correction factors ρ and ϵ is shown in the following.

5.2 Corrections for Non-linear Response

In this section, the corrections for non-linear detector responses are explained. For the data-taking year 2018, sufficient data is available to calculate various types of corrections, the first three subsections will discuss 2018 only. The three types of corrections are:

Default non-linearity The non-linearity that is valid for fills with 2544 bunches (nominal conditions for 2018), explained in subsection 5.2.1.

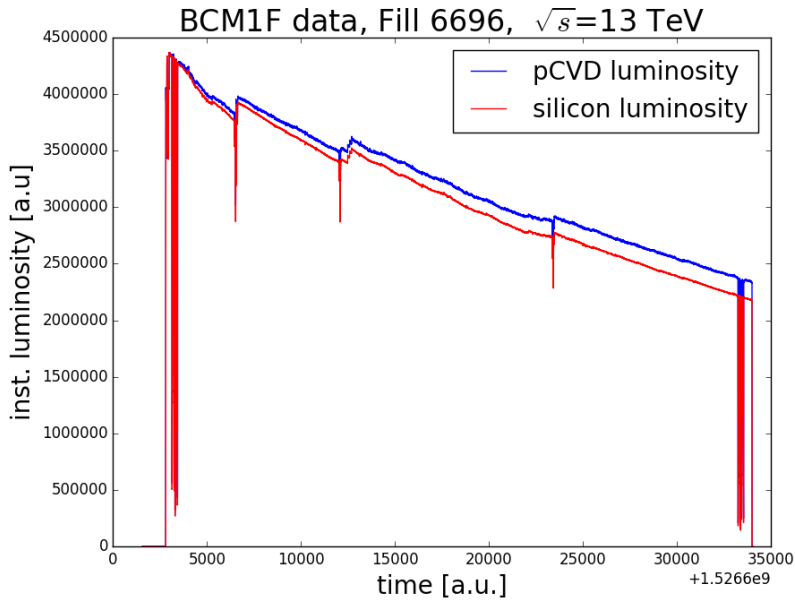


Figure 5.2: The luminosity measurements for one fill of the LHC from the silicon channel of BCM1F in red and from a pCVD channel in blue. For better visibility, a pCVD channel with a similar efficiency as the silicon channel at the beginning of the fill was chosen.

Correction based on the number of bunches in a fill As the non-linearity is dependent on the total rate of detector hits, the default non-linearity can not be used for fills with a lower than nominal number of bunches in the machine. A correction for these fills is shown in subsection 5.2.2.

VdM correction Beam conditions during the VdM scan are vastly different from nominal conditions. A correction for this, based on the corrections above, is shown in subsection 5.2.3.

For 2017, far fewer data is available to calculate corrections. Therefore, the analysis cannot be done at the same level of sophistication as for 2018. The analysis of 2017, based on the methods developed for 2018, is shown in subsection 5.2.4.

5.2.1 Non-linearity in 2018

The visible cross section of the detector was found to be dependent on the total hit rate, since, at high particle fluxes, more hits escape detection, due to dead-time effects in detection material and read-out electronics. This leads to a non-linear behaviour: At the beginning of a fill when there is the maximum number of protons in a bunch, the luminosity is high. The efficiency of the detector then is lower than at the end of a fill,

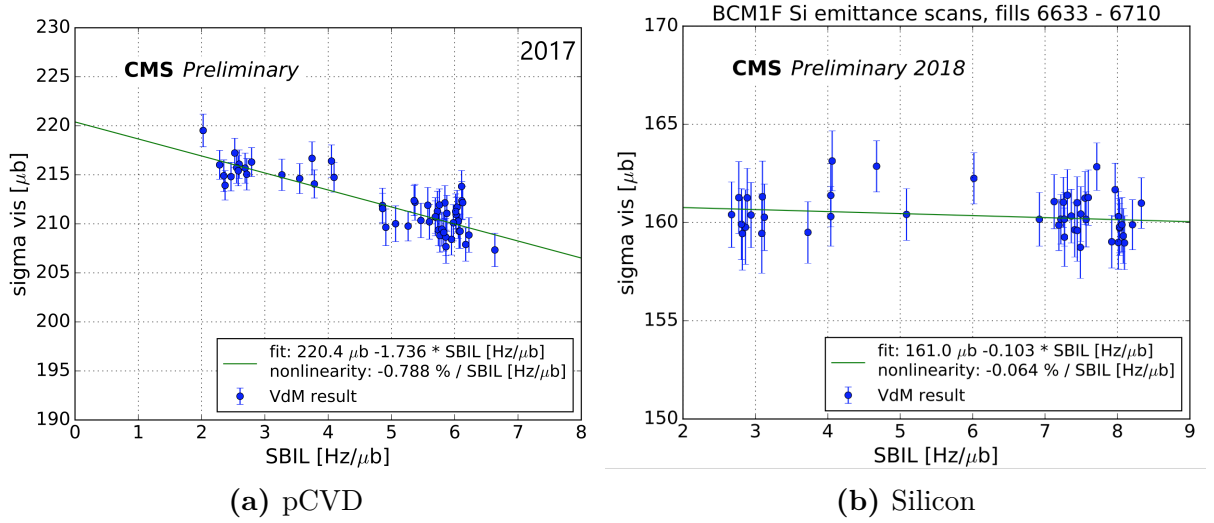


Figure 5.3: Measurements of σ_{vis} as a function of the SBIL, for the pCVD channels on the left and for the silicon channel on the right. For the silicon channel, the emittance scans at low SBIL (at the end of the fills) show approximately the same result as at high SBIL. For the pCVD channels, there is a clear difference between the two sets of scans. The figures are adapted from Ref. [108] (added label for 2017).

when a large fraction of the protons is lost, and the luminosity is lower. The result of such non-linearity can be seen in figure 5.2, in which the measurements of a pCVD channel and a silicon sensor channel for one fill are compared. It is visible that the measurement from the silicon channel decreases more steeply than the pCVD measurement. As the silicon channel is observed to have a linear response from other sources, it can be concluded that the efficiency of the pCVD sensors depends on the instantaneous luminosity.

Using the measurement of σ_{vis} from early and late emittance scans, the non-linearity can be measured directly. Figure 5.3(a) displays the emittance scan measurements as a function of the single bunch instantaneous luminosity (SBIL), the luminosity created by one single collision of a bunch. It is usually measured in $\frac{\text{Hz}}{\mu\text{b}}$. At high SBIL, at the beginning of a fill, the measured σ_{vis} is lower than at low SBIL. Typical values of the SBIL with Run 2 conditions range from 2-3 $\frac{\text{Hz}}{\mu\text{b}}$ at the end of a fill to 6-8 $\frac{\text{Hz}}{\mu\text{b}}$ at the beginning. The average SBIL is proportional to the luminosity. In the following, the values for the non-linearity are stated in "% per unit SBIL". This refers to this average value.

Most data-taking fills in 2018 were done with nominal conditions. Here, the non-linearity can be calculated as the difference in σ_{vis} between the emittance scans at the beginning and the end of a fill. The measurements of the non-linearity per fill can be seen in figure 5.4.

From the measurements with nominal conditions, the default non-linearity is estimated to be 1.4% per unit SBIL for all fills before the VdM scan fill 6868. After this fill,

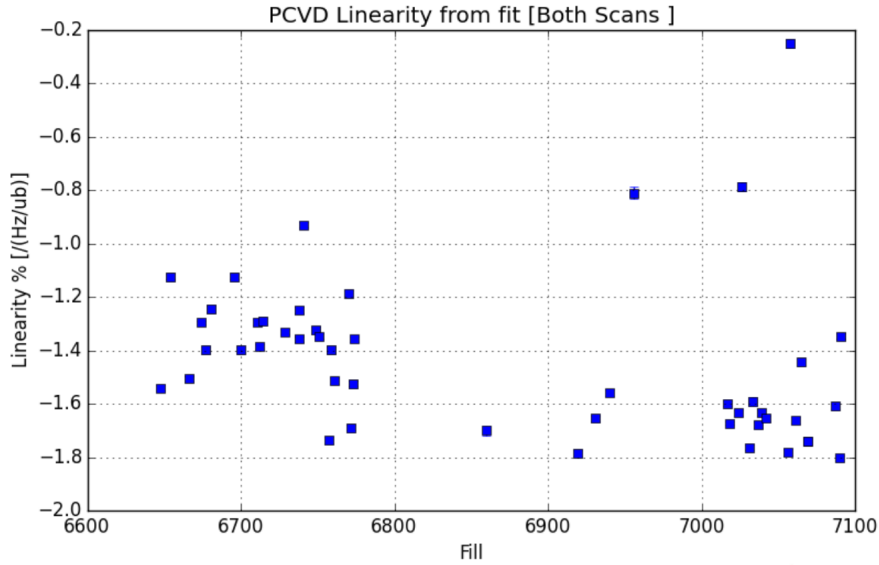


Figure 5.4: Non-linearity calculated from emittance scans at the beginning and end of a fill. Only fills with a nominal conditions are displayed. The non-linearity at nominal conditions can be divided into two regions, caused by a change in the channel mask at the VdM scan in Fill 6868. The figure is taken from Ref. [108].

several pCVD channels were not used any more for the calculation of the instantaneous luminosity, as mentioned above. This leads to a change in the default non-linearity, as the value differs between channels. The non-linearity is estimated to be 1.65% per unit SBIL for all fills after the VdM scan.

The corrections described in the following sections are applied to the default non-linearity values described here.

5.2.2 Dependency of the non-linearity correction on the number of bunches in a fill

Both, the efficiency and the non-linearity described in the previous section, change depending on the total rate of charged particles. Therefore, the values of efficiency and non-linearity are corrected for fills with a lower hit rate. This is the case in fills with a lower number of colliding bunches.

There are only few fills with a lower than nominal number of colliding bunches. As a result, the emittance scans can not be used to calculate the non-linearity as there is too little data available. Instead, the non-linearity is calculated by comparison of the pCVD luminosity measurement to the measurement of another, linear detector.

The silicon channel of BCM1F is chosen as a reference luminometer for 2018, as it shows

Number of colliding bunches	2448	2162	974	590	326
Fills	6640	6638	6688	6613	6594
	6641	6694	6706	6614	6595
	6641		6747	6615	

Table 5.1: Fills with a lower than nominal number of colliding bunches that were used to calculate the corrections depending on the number of bunches. Only fills before the VdM scan are considered. To be published in Ref. [108].

linear behaviour. This can be seen in figure 5.3, which shows the measurement of σ_{vis} both for early and late emittance scans. The measurements for the pCVD channels are shown in figure 5.3(a), those for silicon in figure 5.3(b). While there is a distinct difference between early and late scans (high and low SBIL) for pCVD, the measurements of σ_{vis} are constant for the silicon channel.

However, good data from the silicon sensor is only available up to Fill 6778 in July 2018, when the silicon channel ceased to function. Hence, only fills up to Fill 6778 are used to calculate the corrections to the non-linearity. The fills used and the corresponding number of bunches in each fill are summarised in table 5.1. To calculate the non-linearity, the ratio between the number of hits in a pCVD channel and the number of hits in the silicon channel is calculated for each data point. The resulting ratios are then plotted as a function of the instantaneous luminosity, as obtained from the silicon numbers. An example set of figures from this analysis can be seen in figure 5.5.

Linear fits are performed separately for each of the 20 pCVD channels. The efficiency and non-linearity for each channel and fill are calculated from the results of the fit:

$$\rho = \frac{a}{b}, \quad \epsilon = \frac{b}{\epsilon(2544)} \quad (5.6)$$

with a being the slope of the fit and b the offset. A distribution of the resulting slopes for several fills, with nominal conditions with 2544 bunches, with 974 bunches, and with 590 bunches, can be seen in figure 5.6. While individual channels behave slightly differently, one can observe a clear trend that a lower number of colliding bunches leads to a lower slope. The average for all pCVD channels is used for further calculations.

The calculations are performed for all fills listed in table 5.1, as well as several fills with nominal conditions. The average results for efficiency and non-linearity are then plotted over the number of bunches in the fills. The dependencies of both the efficiency and the non-linearity on the number of bunches in a fill is approximately linear. Therefore, linear fits are performed to describe these dependencies. The results are displayed in figure 5.7. The results of the fits give:

$$\rho = -2.369 \times 10^{-5} \cdot n + 1.060 \quad (5.7)$$

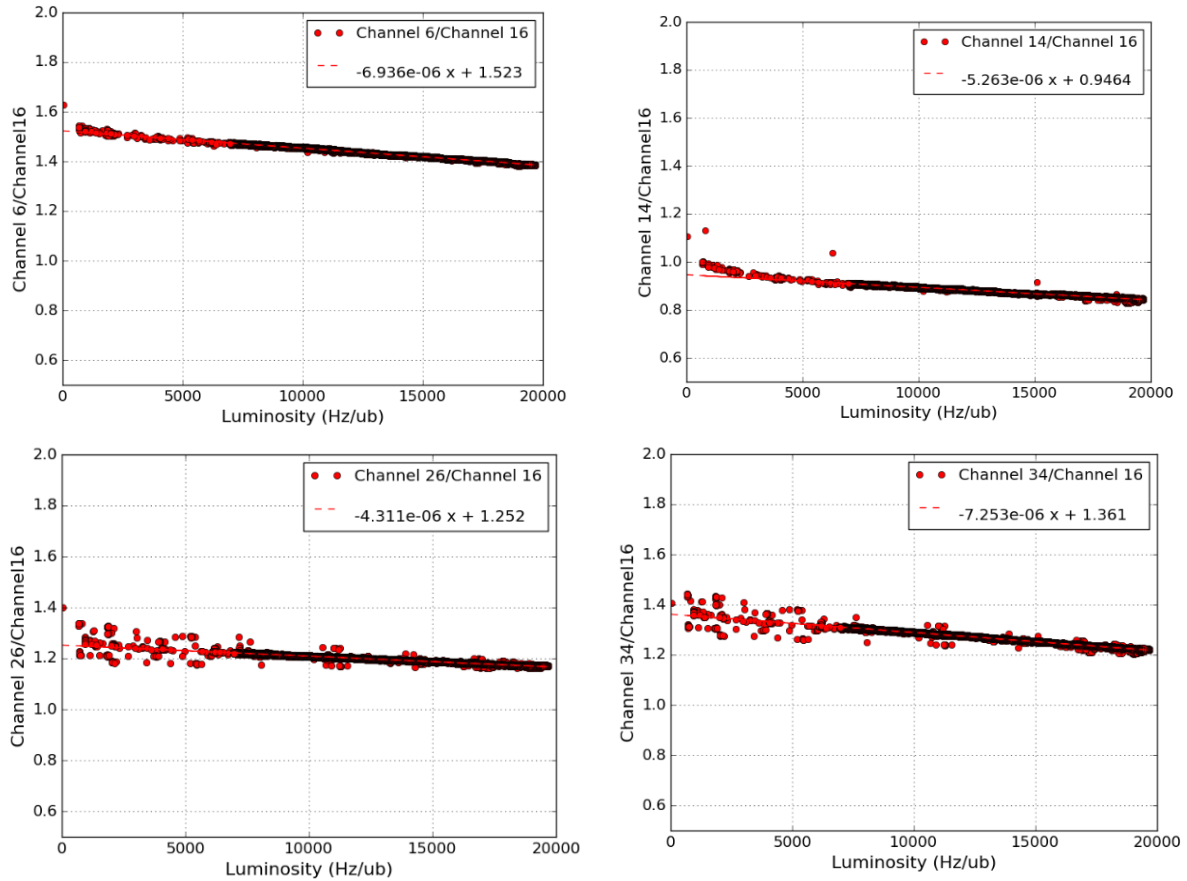


Figure 5.5: The ratio between the measurements of the instantaneous luminosity from selected pCVD channels and the silicon channel (Channel 16), as a function of the instantaneous luminosity (determined by the silicon sensor). The distributions show a linear dependency, and corrections are derived from linear fits to this ratio. The two figures at the top show channels on the +Z side, the plots at the bottom for channels on the -Z side. The spread of data points for low values in instantaneous luminosity (points taken during emittance scans) can be attributed to inaccuracies in timing for the -Z side.

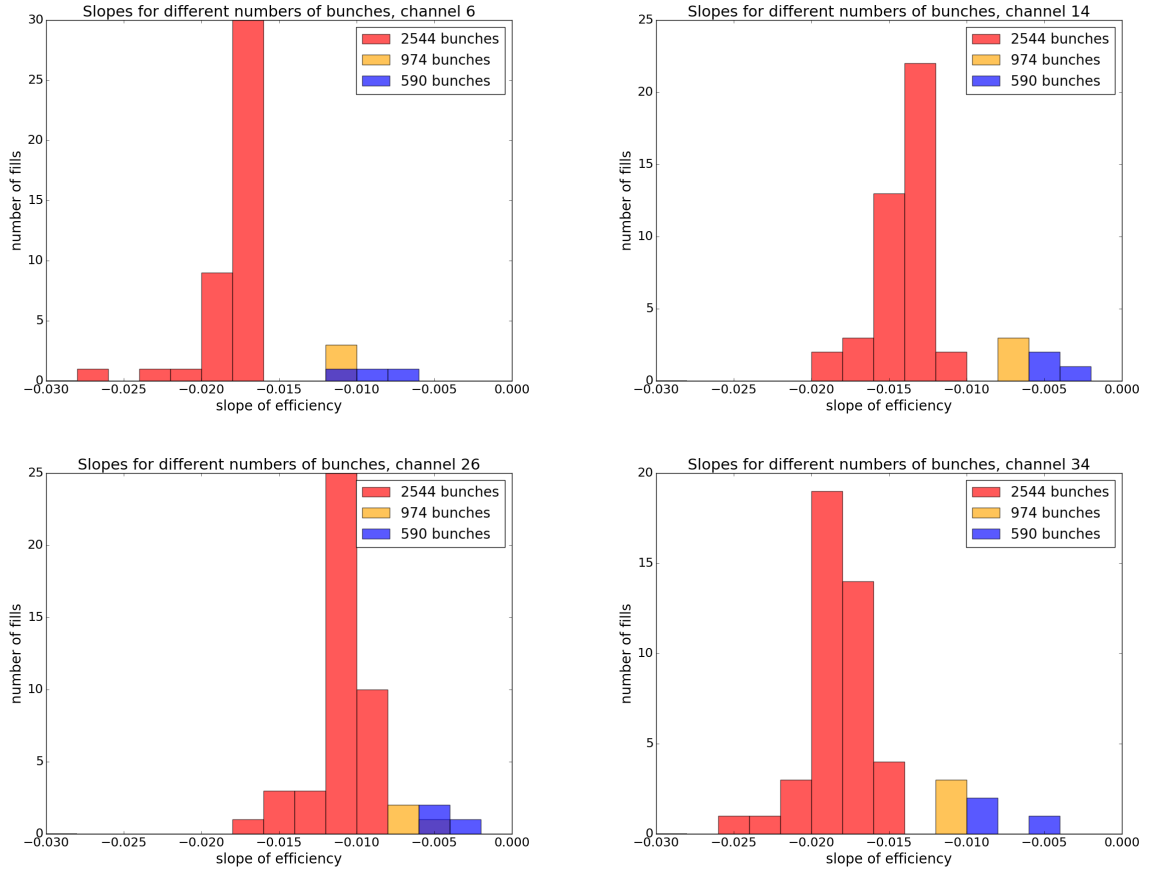


Figure 5.6: Distributions of the slopes, fitted from the ratio of pCVD luminosity and silicon luminosity as a function of the silicon luminosity, for four example channels. The slopes from fills with 2544 bunches are displayed in red, from 974 bunches in yellow and from 590 bunches in blue. Even though there are only three data points in the yellow and blue distributions, it is clearly visible that fills with a lower number of colliding bunches feature a less pronounced slope.

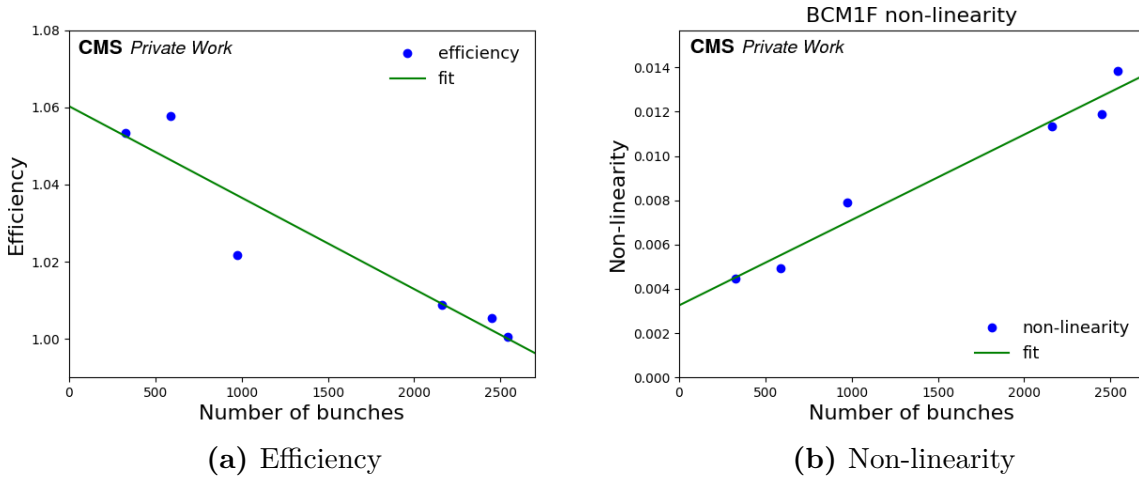


Figure 5.7: Non-linearity and efficiency as functions of the number of colliding bunches in a fill. The data points are derived from averaging over all available fills for each number of colliding bunches and all pCVD channels. The linear fits used to describe the dependency are displayed in green. To be published in [108].

and

$$\epsilon = 0.000295 \cdot n + 0.249, \quad (5.8)$$

where n is the number of colliding bunches. The parameters obtained from the linear fits are used to correct the efficiency and the non-linearity of all data-taking fills in 2018, depending on the number of colliding bunches.

5.2.3 Correction on the Van der Meer Scan measurement

The initial measurement of σ_{vis} to which the corrections are applied, is determined in the VdM scan in Fill 6868. However, the conditions in the VdM scan fill are different from nominal conditions and a correction extrapolating to nominal conditions must be found. Firstly, there are only 124 colliding bunches in the VdM fill. The correction depending on the number of colliding bunches cannot be applied directly, however, due to significantly different beam conditions. The beams are wider than in nominal conditions, leading to fewer collisions per bunch crossing. Also, the filling scheme uses single bunches instead of bunch trains with 25 ns spacing. This is a very different environment than the nominal conditions with bunch trains because the detector efficiency is recovering between the collisions of the single bunches.

Since the rate is therefore very low compared to nominal conditions, it can be assumed that the detector operates at maximum efficiency, with no observable rate effects. To estimate the value of this efficiency, the correction for the number of bunches is used as a

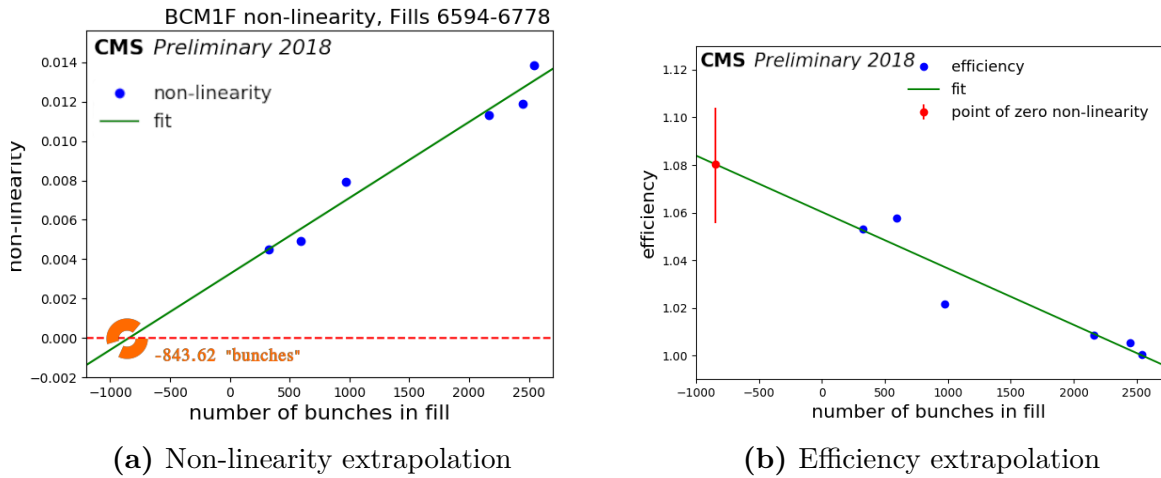


Figure 5.8: The distributions and linear fits from figure 5.7, with extrapolations to derive the correction that is necessary to apply the VdM scan measurement to nominal conditions. The non-linearity fit is extrapolated to a point, where the non-linearity would reach 0. This point, on the fitted line of the efficiency, is then used as correction value for σ_{vis} measured in the VdM scan. To be published in [108].

basis. The linear fit that is performed to calculate the dependency is extrapolated to the point where the non-linearity reaches zero. This results in a hypothetical value of about -844 bunches. To estimate the maximum efficiency, the efficiency correction as a function of the number of colliding bunches is then extrapolated to this purely theoretical negative number of bunches. This yields a correction of 1.08, meaning that the efficiency in the VdM scan is about 8% higher than in nominal conditions with 2544 colliding bunches. Plots of this extrapolation can be seen in figure 5.8, including the statistical error from the fit, which is about 0.02.

This is only a rough estimate without physical explanation. However, it is the best estimate that could be found with the available data.

5.2.4 Non-linearity in 2017

The methods described above can not be applied for the non-linearity correction of BCM1F for the data-taking year 2017. This is for various reasons: due to technical problems with electronic noise, the silicon channel does not show the same linear behaviour as in 2018 and cannot be used as comparison. Also, the filling scheme is changed during the year from bunch trains with 25 ns between all bunches in the train to trains with a four-bunch gap every eight bunches (8b4e). As this changes the hit rate in the detector significantly, the two regions would have to be analysed separately and there are not enough fills with different numbers of colliding bunches to make a linear fit as it is

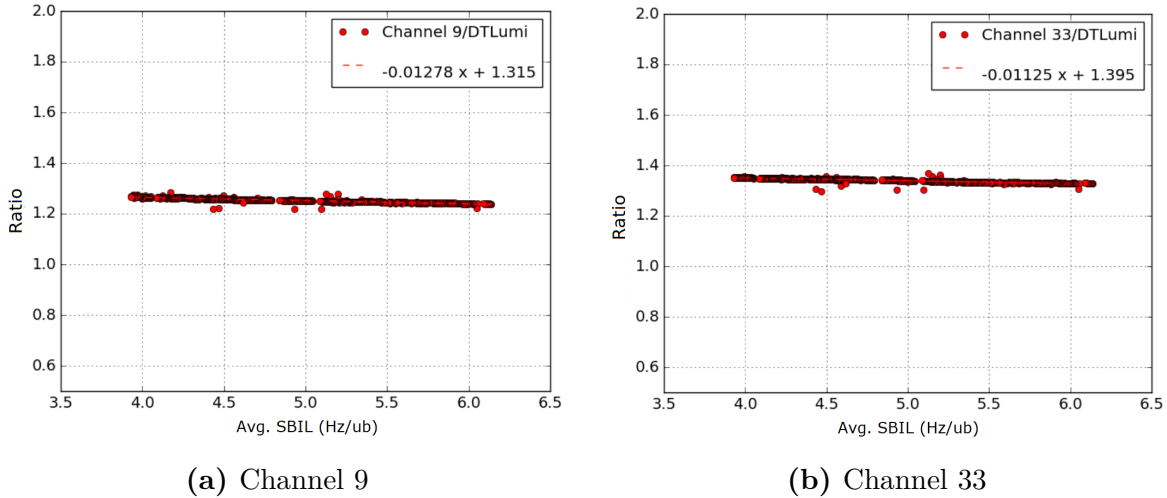


Figure 5.9: Ratio of the luminosity measurement from the pCVD channels of BCM1F to the luminosity measurement of the DT luminosity system. A linear fit is applied to calculate the non-linearity. The ratios are somewhat noisy and strong constraints are necessary in order to achieve a valid fit result. Only data points at an average SBIL above $4 \text{ Hz}/\mu\text{b}$ are displayed to exclude the emittance scan area. Furthermore, only points within 3% of the mean of the ratio are included.

done for 2018. Therefore, different methods to analyse and calibrate the detector need to be found.

As a reference luminometer, DT (see section 3.4) was chosen. The linear fits to the ratio between channels and reference are performed in the same way as for the 2018 analysis. Two example channels for this analysis are shown in figure 5.9. In contrast to 2018, the ratio points are only used at an average SBIL of about 4 and above. This is necessary as the hit rate in DT is much lower than in BCM1F. Therefore, DT is not suited to resolve the emittance scans. This leads to fluctuations of the ratio at low instantaneous luminosity. This also leads to a large number of outlier points across the complete range of luminosity. In the fits, outliers are excluded by allowing only points within 3% of the mean of the ratio. Despite these measures, valid fits are only possible for a limited number of fills.

To estimate the default non-linearity, the comparison to DT was used, instead of the emittance scan analysis as it was done in 2018. This is necessary, as emittance scans are analysed bunch-by-bunch and therefore cannot describe the change in filling scheme. Figure 5.10 shows the measured non-linearity per fill. Different colours indicate different numbers of colliding bunches in the respective fills. In the period between Fill 6019 and Fill 6150, a 25 ns filling scheme was used. While a linear dependence of the non-linearity to the number of colliding bunches can be assumed, there are not enough fills to verify this assumption. Therefore, the non-linearity is determined separately for different periods of

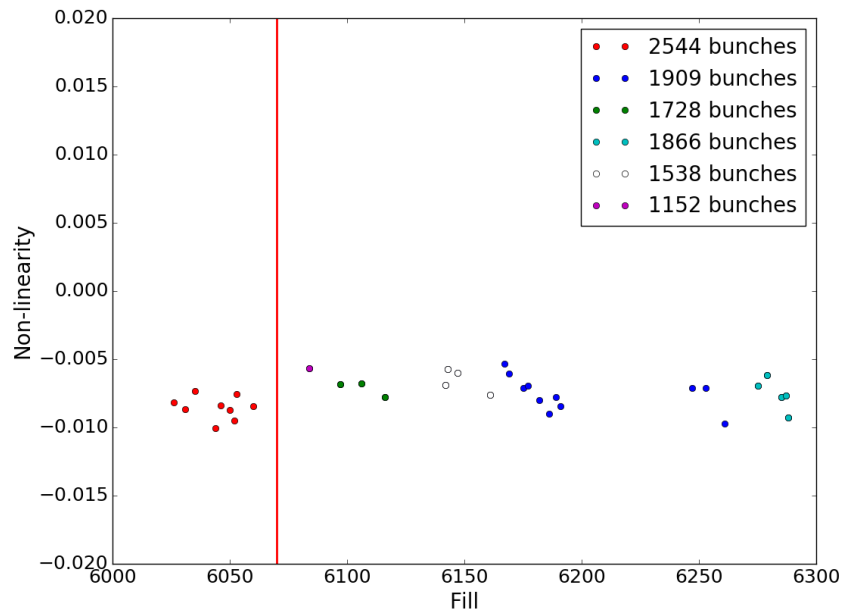


Figure 5.10: Non-linearity per fill for the data-taking year 2017. Different numbers of colliding bunches in the fills are shown in different colours. The non-linearity derived from this plot is 0.85% per unit SBIL for the first region (populated by fills with nominal conditions, shown in red) and 0.72% per unit SBIL for the second region, with the first four fills with a 25 ns filling scheme and an 8b4e filling scheme for all following fills (see text).

data-taking, grouping fills into regions with different constant values as it was done for the default luminosity in 2018.

With this method, two regions with different non-linearities are identified. In the first region, which is populated by fills with a nominal conditions only, this non-linearity is 0.85% per unit SBIL. In the second region, which is mostly, but not exclusively, populated by fills with the 8b4e filling scheme, no dependency of the non-linearity on the number of colliding bunches can be seen. For this reason, all fills from Fill 6062 to the end of the year are calibrated with a non-linearity of 0.72% per unit SBIL.

Efficiency corrections, analogous to those obtained in the 2018 non-linearity analysis, could also only be derived by region. These efficiency corrections by region are described as part of the overall detector performance analysis, discussed in the following section. Therefore, no non-linearity based efficiency correction is applied.

5.3 Radiation Damage and Annealing Effects

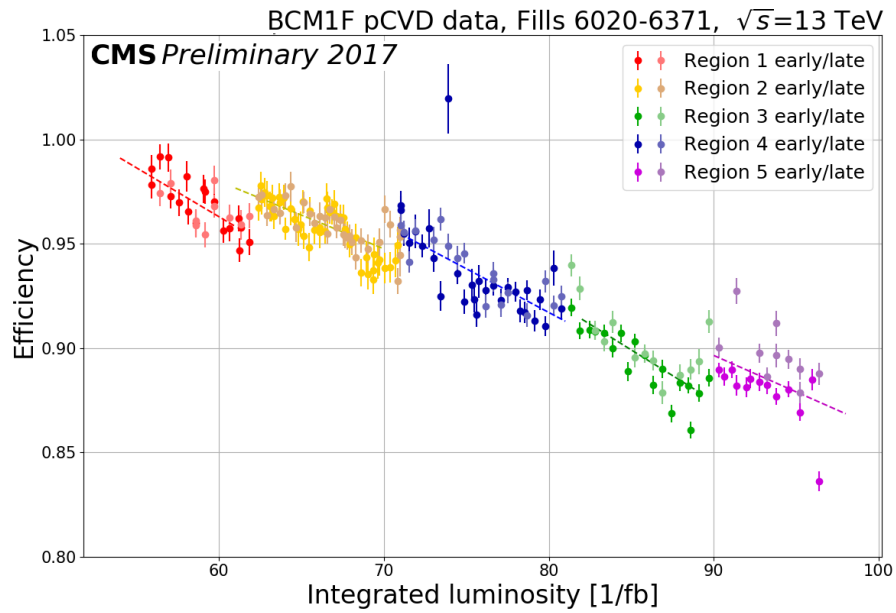
The efficiency of the detector is also influenced by time-dependent effects, like ageing, through accumulating radiation damage in the sensors as well as the readout electronics. There, the front end lasers of the optical readout are particularly susceptible to irradiation effects. Annealing happens when the lasers are warmed and the radiation damage is reversed, recovering efficiency. This typically happens when the tracker system, which provides also the cooling for BCM1F, is turned off.

To keep track of these changes, the emittance scans that measure σ_{vis} for each fill are analysed. The measurements for all fills with nominal conditions are plotted as a function of the integrated luminosity, which is proportional to the radiation the detector was subjected to. The resulting distributions for the data-taking years 2017 and 2018 can be seen in figures 5.11(a) and 5.11(b).

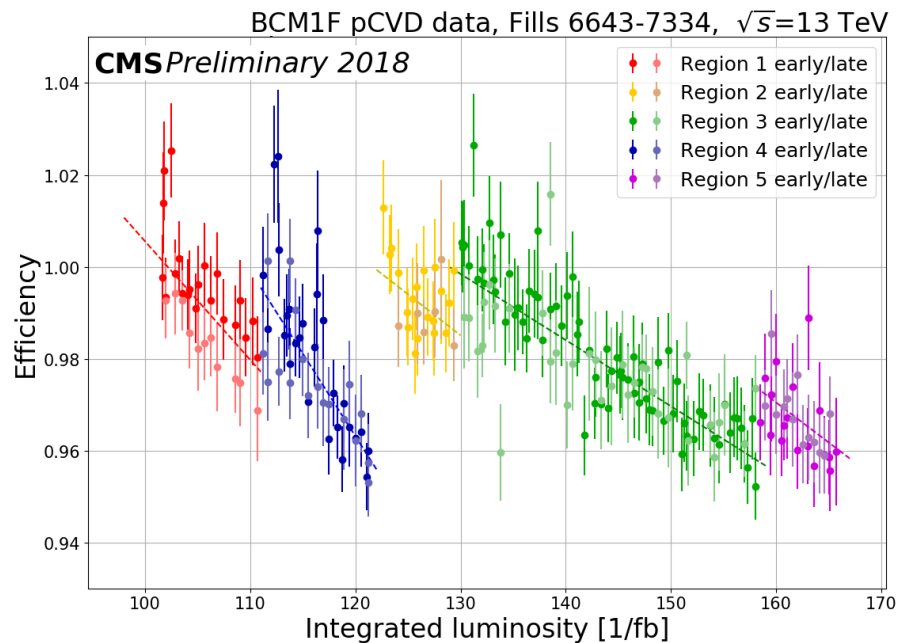
The distributions show linear declines in efficiency, interrupted by jumps to higher values. To determine a dependency that can be used as a calibration, the data points are divided into different regions, bordered by jumps in efficiency. For each region, a separate linear fit is performed.

For 2018, each of the jumps in efficiency can be attributed to a change in the detector environment. An example for such an event is a period of time when the cooling was turned off and the detector warmed up. The strongest jump, between the blue and yellow regions, can be attributed to the masking of channels. The efficiency measured at the VdM scan is defined as the nominal value.

For 2017 the jumps and changes in slope can not always be attributed to events in the detector environment and the regions have to be chosen by eye. Both for 2017 and 2018, five regions with different characteristics can be identified. Separate linear fits are done for all the regions. The resulting calibration curves can be found in table 5.2.



(a) Detector performance 2017



(b) Detector performance 2018

Figure 5.11: Detector performance analysis for 2017 and 2018. The efficiency decreases over time, as radiation damage accumulates. The jumps in the efficiencies are caused by annealing effects, when the detector is warmed up during technical stops. The regions between the jumps are calibrated via linear fits. Different fit regions are displayed in different colours. For 2018 all jumps can be attributed to physical events. For 2017 the regions are chosen by eye. To be published in [108].

Detector performance 2017	
Fills <6061	$-0.00469 \cdot \text{int.lumi} + 1.244$
Fills 6061 - 6194	$-0.00323 \cdot \text{int.lumi} + 1.174$
Fills 6194 - 6291	$-0.00419 \cdot \text{int.lumi} + 1.252$
Fills 6291 - 6336	$-0.00492 \cdot \text{int.lumi} + 1.317$
Fills >6336	$-0.00350 \cdot \text{int.lumi} + 1.211$
Detector performance 2018	
Fills 6594 - 6711	$-0.00259 \cdot \text{int.lumi} + 1.264$
Fills 6711 - 6800	$-0.00360 \cdot \text{int.lumi} + 1.395$
Fills 6800 - 6980	$-0.00179 \cdot \text{int.lumi} + 1.217$
Fills 6980 - 7259	$-0.00144 \cdot \text{int.lumi} + 1.186$
Fills >7259	$-0.00174 \cdot \text{int.lumi} + 1.249$

Table 5.2: Calibration curves from the emittance scan analysis for BCM1F in 2017 and 2018. To be published in [108].

5.4 Final Calibration

In this section, the effects of the calibrations are shown and the quality of the calibrated BCM1F measurements is discussed. For this purpose, the measurements including the corrections shown in this chapter are compared to the best up-to-date luminosity measurements from HFOC (HFET for 2017) and DT, as well as to a BCM1F calibration without the corrections applied.

The effects of the corrections can be seen in figure 5.12. In this figure, ratios of different luminosity measurements are shown. The blue dots indicate the ratio between the latest calibration of HFOC, which is assumed to be the best luminosity measurement in 2018, and BCM1F without the corrections (labelled BCM1Fv3). This calibration includes only a flat 1.4% per unit SBIL for the non-linearity correction. No other corrections for efficiency or non-linearity are applied. The orange dots show the ratio between the latest calibration of HFOC and the new calibration of BCM1F (labelled BCM1Fv5), with all corrections applied. The non-linearity can be seen easily in the blue line. In the figure, the points corresponding to one fill form an almost vertical line, as the visible cross section rises with decreasing luminosity. The data after the calibration, depicted by the orange line, still reveal a similar pattern. However, the quantitative discrepancy between early and late data points in the fills is much reduced. The ratio of the BCM1F data before and after calibration, depicted by the green line, i.e. the applied correction, is also shown. Fills with nominal conditions up to the VdM scan (up to about 15 fb^{-1} of integrated luminosity) are not additionally corrected for the non-linearity, as, in that region, the 1.4 % per unit SBIL default non-linearity correction is applied in both calibrations. However, also in this area, the fills with a lower than nominal number of bunches are corrected for

efficiency and non-linearity. This can be seen best in the first 5 fb^{-1} . There, the number of bunches is raised from fill to fill. The correction based on the number of bunches lowers the efficiency, creating a stable measurement at the same ratio to HFOC as for fills with nominal conditions. This correction also removes outliers in the blue line, created by fills with a different number of bunches.

The VdM scan correction shifts the ratio from an average of the ratio at about 1.06 in the old calibration to lie between 1.02 and 1. The correction for long-term effects stabilises this ratio by correcting for the slopes in the distribution.

As a result, the new BCM1F calibration leads to a stable measurement compared to the HFOC measurement, at a ratio between 1.02 and 1.

A histogrammed distribution of the ratio can be seen in figure 5.13. The amount of data recorded at is displayed as a function of the ratio. A clear double peak structure can be seen, resulting from the jump in efficiency after the VdM scan. The first about 15 fb^{-1} form a peak at about 1.02, while the higher peak is created by the rest of the year, around about 1.

In figure 5.14 comparisons of the calibrated BCM1F data with the data from HFOC and DT are shown. The ratio between DT and HFOC is shown in orange. It is close to unity on average. This is expected due to DT being calibrated with reference to HFOC (cross calibration), as it cannot be calibrated with the VdM method. However, it can also be seen that the ratio between HFOC and DT shows no non-linearity and is more stable than the ratio of both luminometers to BCM1F. While BCM1F can not deliver a measurement that is competitive with the other luminometers, it has to be noted that this result was achieved without cross calibration, making it completely independent of any other measurement. The general agreement of the BCM1F data with the other luminometers thus adds to the confidence that the luminosity measurements are well understood. The calibrated measurement for 2017 can be seen in figure 5.15. As for 2018, this figure compares a calibration of BCM1F with only a flat non-linearity correction applied, shown in blue, with the newly calibrated version shown in orange and the ratio between the two shown in green. The calibration for 2017 is less successful than for 2016. While it manages to stabilise the measurement for the later part, there are still large fluctuations compared to HFET. Also, the non-linearity is not corrected for later fills. This result can be explained by the technical problems in BCM1F in 2017, as well as by the lack of good calibration sources.

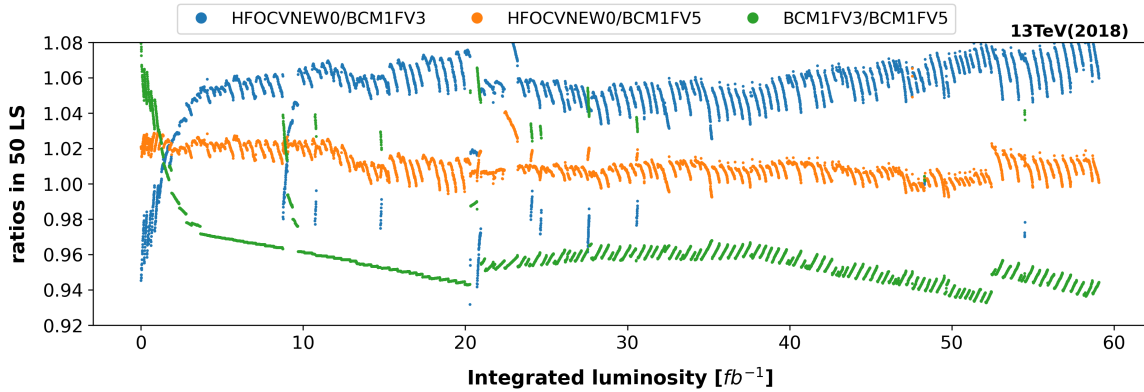


Figure 5.12: Ratio of luminosity measurements between BCM1F and HFOC for 2018. The blue dots indicate the ratio between the latest calibration of HFOC, and an older calibration of BCM1F (BCM1Fv3). The orange dots show the ratio between the latest calibration of HFOC and the new calibration of BCM1F (BCM1Fv5). In green, the ratio between the two BCM1F calibrations is shown.

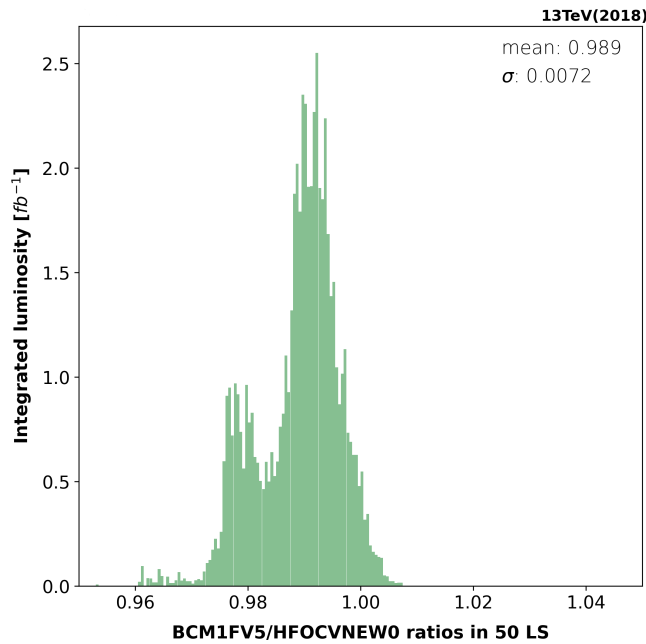


Figure 5.13: Ratio of luminosity measurements between BCM1F and HFOC for 2018. The ratio is shown on the x-axis, on the y-axis the amount of luminosity recorded at a certain ratio is shown.

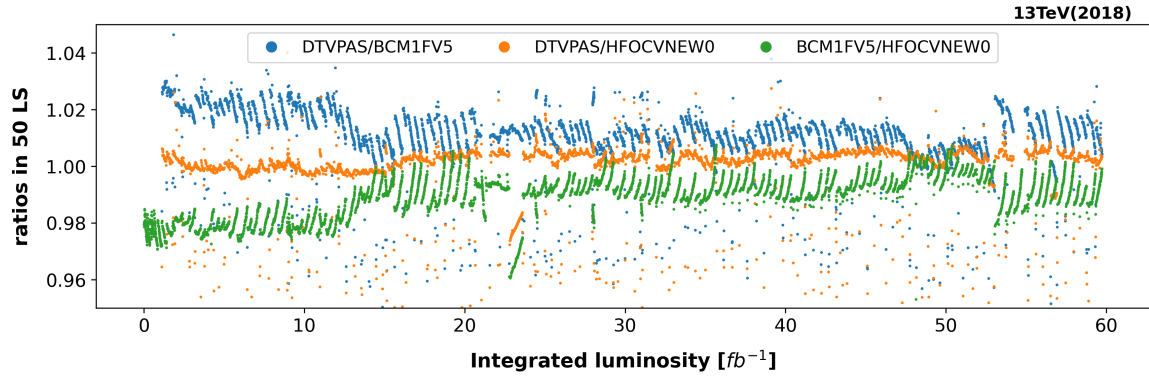


Figure 5.14: Ratio of luminosity measurements between BCM1F, HFOC and DT for 2018. The blue dots show the ratio between DT and BCM1F, the green between HFOC and BCM1F. In orange, the ratio between DT and HFOC is shown.

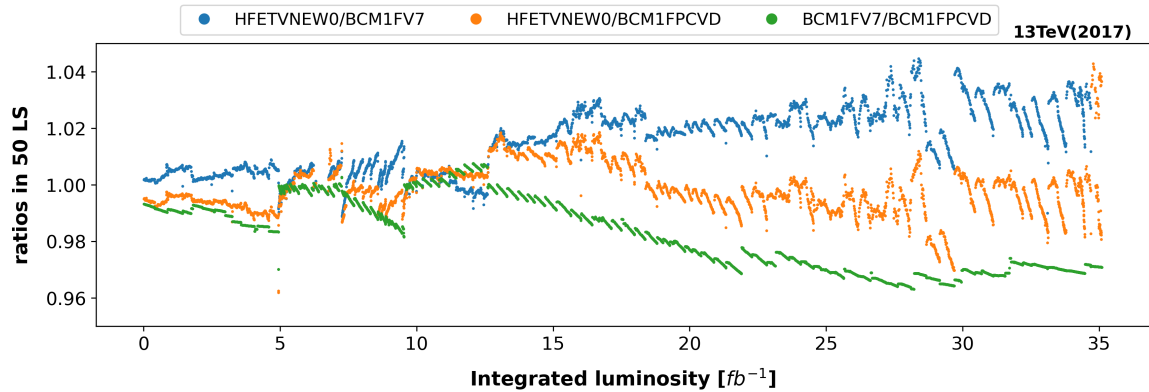


Figure 5.15: Ratio of luminosity measurements between BCM1F and HFET for 2017. The blue dots indicate the ratio between the latest calibration of HFET, and an older calibration of BCM1F. The orange dots show the ratio between the latest calibration of HFET and the new calibration of BCM1F. In green, the ratio between the two BCM1F calibrations is shown.

Part III

Measurement of the $t\bar{t}Z$ Cross Section

Part III of this thesis describes the measurement of the cross section for top quark pair production in association with a Z boson ($t\bar{t}Z$). Top quark pair events are selected with two leptons (electron or muons) in the final state. The associated Z bosons are identified through their hadronic decay into a final state with one boosted jet. The analysis is based on data collected during the LHC Run 2 data-taking period, by the CMS Experiment.

This part of the thesis is structured as follows: in this first chapter, the motivation for the measurement is explained and a summary of previous measurements is given. In the second section 6.2, the basic analysis strategy is described.

In chapter 7, the definition of the so-called physics objects, electrons, muons and jets, as they are used in the analysis is shown. Furthermore, the selection criteria for the phase space in which the measurement is performed are presented. This phase space will be further referred to as "signal region".

The following chapter, 8, discusses the most important background processes for the measurement. In chapter 9, the development of a deep neural network is shown. Using the events in the signal region, the network is trained to discriminate $t\bar{t}Z$ signal events from background events. It is described in detail which input variables are used, which hyperparameter settings were chosen, and it is analysed how different choices influence the separation power.

In chapter 10 the estimation of the various systematic uncertainties included in the calculation of the cross section are shown. The agreement of simulation and data in the signal region is analysed in section 11.

Sensitivity and optimisation studies using simulations are shown in chapter 12. The effects of changes in the boosted jet definition (different cuts on the transverse momentum and mass) and the separation into two b jet categories are presented.

The result of this analysis – the measurement of the $t\bar{t}Z$ production cross section – is discussed in chapter 13.

The final chapter 14 discusses possibilities for further studies, namely the analysis of different signal regions, as well as opportunities at LHC Run 3.

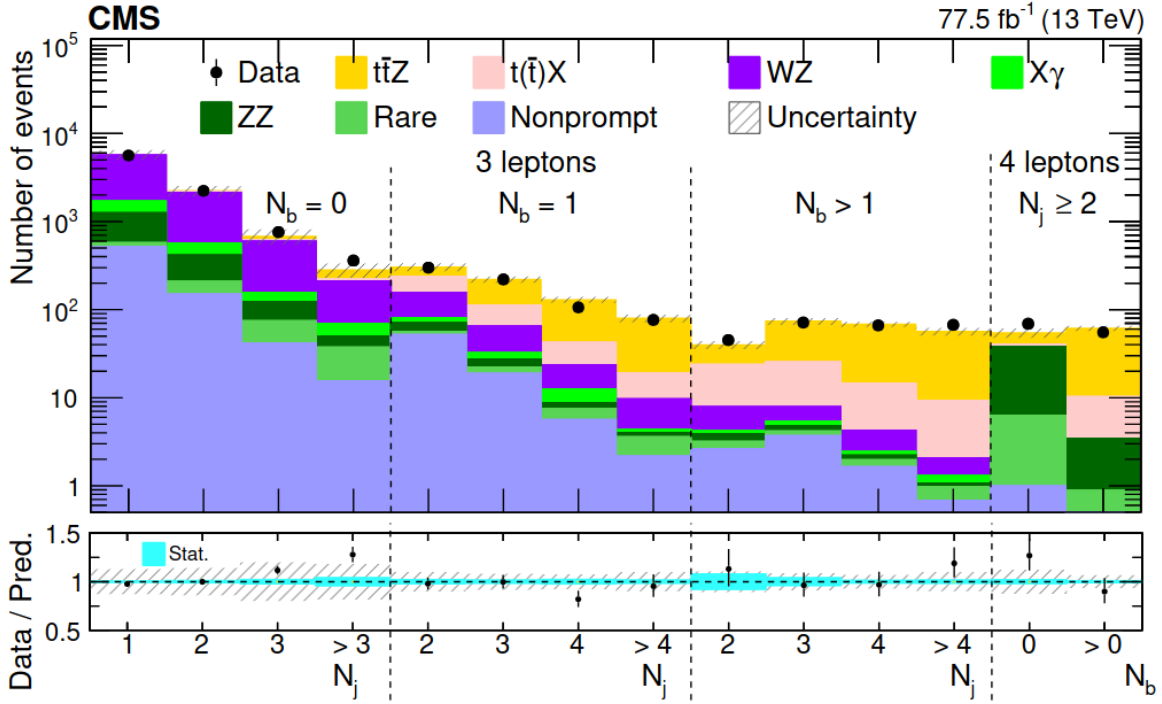


Figure 6.1: The event yields of various signal regions split by jet and lepton multiplicities, from the measurement of the $t\bar{t}Z$ production cross section with leptonic Z boson decays. The $t\bar{t}Z$ signal is displayed in yellow. Figure taken from Ref. [43].

6.1 Motivation and Previous Results

The $t\bar{t}Z$ process is expected in the standard model of particle physics, as described in section 2.4. Since cross sections of $t\bar{t}$ production have been measured with high precision, measuring this cross section provides direct access to the coupling strength of Z bosons to top quarks and can provide sensitivity to possible anomalous t-Z couplings, as proposed by several beyond the standard model theories. The process has been studied at the LHC in Run 1 with 8 TeV in both ATLAS and CMS [111, 112], together with the $t\bar{t}W$ process. The cross section of $t\bar{t}Z$ at 13 TeV was measured in CMS in Ref. [41] and in ATLAS in Refs. [42] and [44]. The CMS result reported in Ref. [43] includes the 2016 and 2017 data and is the most precise measurement to date,

$$0.95 \pm 0.05(\text{stat}) \pm 0.06(\text{syst}) \text{ pb.} \quad (6.1)$$

The most recent measurement by ATLAS [44] provides a cross section measurement of

$$0.99 \pm 0.05(\text{stat}) \pm 0.08(\text{syst}) \text{ pb.} \quad (6.2)$$

Table 6.1: The integrated luminosity of best-quality physics data, at $\sqrt{s} = 13$ TeV, provided by the CMS Experiment for 2016–2018.

Year	int. luminosity [fb^{-1}]	uncertainty [%]
2016	36.3	1.2 [76]
2017	41.5	2.3 [114]
2018	59.8	2.5 [115]
Combined	137.7	1.6

All measurements to date are in agreement with the standard model prediction of approximately 0.84 ± 0.1 pb [113].

The measurements described above target leptonic Z boson decays both in the 3-lepton (semi-leptonic $t\bar{t}$ decays) and 4-lepton (dileptonic $t\bar{t}$ decays) final states. A summary of the event yields, used for the latest measurement by CMS for various signal regions split by jet and lepton multiplicities, can be seen in figure 6.1.

Hadronic Z boson decays have been considered in neither of the previous publications. This thesis provides the first measurement of the $t\bar{t}Z$ production cross section using this decay channel.

The hadronic channels can be an important contribution to the existing measurements, as the leptonic channels have limited statistical accuracy in the region with Z bosons with a high p_T . In this region, in effective field theories, possible deviations from the standard model prediction are expected to be largest. In the measurement of the $t\bar{t}Z$ production cross section done by CMS, differential measurements are also shown. In figure 6.2, the cross section measurement is shown as a function of the transverse momentum of the Z boson, in four bins. The first three bins, up to Z boson p_T of 250 GeV, have a relatively high statistical accuracy. In the last bin, however, only few events are present, and the cross section can only be measured with an accuracy of about 20%. This is the region, where boosted $Z \rightarrow q\bar{q}$ decays offer sensitivity.

Using only hadronic high p_T Z bosons, this analysis provides an independent measurement of the $t\bar{t}Z$ production cross section. It also provides an insight into the scarcely explored region with Z bosons with large transverse momenta.

6.2 Analysis Strategy

The data used to perform this analysis was collected by the CMS Experiment during LHC Run 2, from 2016 to 2018. Only proton-proton collisions at a centre-of-mass energy of $\sqrt{s} = 13$ TeV are used. Other data recorded during Run 2, such as collisions at a lower centre-of-mass energy or heavy ion collisions, are not analysed in this thesis.

In total, proton-proton collision data corresponding to an integrated luminosity of about 138 fb^{-1} is available. Of these, 36.3 fb^{-1} were collected during 2016, 41.5 fb^{-1} during

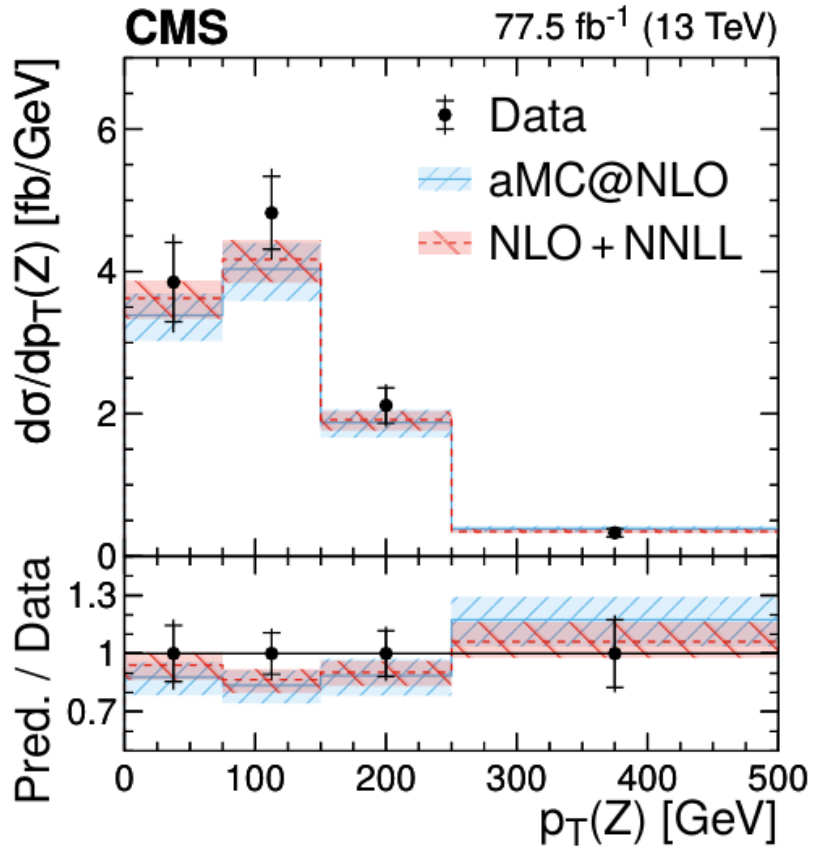


Figure 6.2: Differential measurement of the $t\bar{t}Z$ production cross section as a function of p_T Z . Two different theoretical predictions are shown in red and blue. In the last bin, for Z bosons with a p_T of above 250 GeV, the statistical error of the measurement is largest. Taken from Ref. [43].

2017 and 59.8 during 2018 [63]. A summary of these numbers can be found in table 6.1. To measure the production cross section of $t\bar{t}Z$, a likelihood fit is performed, fitting the results of a standard model simulation to the experimental data in a defined signal region. The signal strength parameter defining the cross section measurement (or an upper limit on it) and the significance of the measurement are extracted from this fit. The fits are done using the Combine framework (developed for Ref. [116]), which provides a multitude of statistical tools for CMS analyses. Details about the mathematical methods used can be found in Refs. [117–119].

For the definition of the signal region, it is of concern that top quark events often include a large number of jets. Leptonically decaying Z bosons can be reconstructed from two opposite-charge leptons with a dilepton mass close to the Z boson mass. However, reconstructing hadronically decaying Z bosons from jets is much more difficult because the backgrounds from multijet events are substantial and the experimental resolution of jets is not as good as that of leptons. The combinatorial nature of the jet pairing as well as the large cross section of top quark pair production with additional jets leads to a very high irreducible background in the $t\bar{t}Z$ signal region. In order to mitigate this background, only Z bosons with a transverse momentum greater than 200 GeV are considered in this thesis. Above this threshold, the jets from the decaying boson are highly collimated, forming one single boosted jet. Analysis of the boosted jet substructure allows to identify jets that originate from boson decays and to suppress the background.

The events in the signal region are classified using a Deep Neural Network. The network classifies an event as 'signal-like' (high output discriminant value) or 'background-like' (low output discriminant value), creating a region with a high signal purity at the upper end of the classifier distribution. The output distribution of the classifier is then used to perform the fits to extract the cross section.

DEFINITION OF THE SIGNAL REGION

7.1 Particles and Objects

Physics objects are identified in the detector based on their tracks and energy deposits, as described in chapter 4. For the final analysis, additional cuts are applied to the objects, to achieve a better purity and agreement of the simulation with the data. This chapter focuses on the physics objects used in the analysis.

7.1.1 Leptons

Only electrons and muons are used in the analysis and are referred to as leptons. Tau leptons are disregarded because of their hadronic decay channels and the presence of neutrinos in their decays.

Electrons and muons are taken from particle-flow candidates, as explained in section 4.2. In addition, the cut-based identification criteria (IDs) described in section 4.4 are applied. The electron ID uses a combination of criteria from particle-flow isolation, ECAL shower shape and tracker hits to separate actual electrons from backgrounds e.g. from jets with a

Table 7.1: The cuts applied to electrons and muons. The particle-flow isolation describes the minimum ΔR between the lepton and other particle-flow candidates. The impact parameter d is the closest distance of the track to the primary vertex.

Cut	electrons	muons
ID	medium	medium
Pseudorapidity	<2.5	<2.4
particle-flow isolation	0.15	0.15
d_z	<0.1	<0.1
d_{xy}	<0.05	<0.05

high electromagnetic content which can be misidentified as electrons. Information about the electron ID can be found in Ref. [102]. The medium working point, used in this analysis, has an efficiency of 80%.

For muons, the information from tracker hits and the muon system is used to construct an ID [120]. For the medium working point, the efficiency is 99.5%.

A number of additional cuts, recommended for use with the lepton IDs, are applied, including isolation and impact parameter cuts. A summary of all cuts applied to electrons and muons can be found in table 7.1.

As the reconstruction efficiency is lower in the forward region due to the limited detector coverage, a cut on the pseudorapidity η is applied. All electrons must have $|\eta| < 2.5$, muons are required to have $|\eta| < 2.4$.

7.1.2 Jets

Jets are reconstructed using the anti- k_T algorithm [86] following the procedure described in section 4.3. For non-boosted jets, a radius parameter of 0.4 (AK4) is used. In addition, jets are required to have a transverse momentum larger than 30 GeV. As the jet reconstruction efficiency is lower in the forward detector region, only jets with $|\eta| < 2.4$ are considered.

It is possible that two different objects are reconstructed from the same underlying particle. In case of overlap between different objects in the event, only one of the objects can be kept.

Jets that overlap with leptons ($\Delta R_{j,\ell} < 0.4$) are removed from the selection and the leptons are kept. In case of overlap between AK4 jets and boosted jets ($\Delta R_{j,bj} < 0.8$) the boosted jets are used and the AK4 jets are removed.

The DeepJet [90] algorithm, is used to probe whether a non-boosted jet originates from a b quark, as explained in section 4.3.1. Jets with a b jet classifier value above the medium working point are considered b jets.

7.1.3 Boosted jets

Boosted jets are reconstructed with a larger cone size in comparison to non-boosted jets. In this analysis, boosted jets are reconstructed with the anti- k_T algorithm, using a radius parameter of 0.8 (AK8). Boosted jets can originate from hadronically decaying vector bosons with a transverse momentum greater than approximately 180 GeV. Above this threshold, the two jets from a hadronic decay are so strongly collimated that they merge into one single larger jet. However, boosted jets can also originate from random overlap of other jets in the event, like QCD jets or jets from top quark decays.

In this analysis, boosted jets are used to identify the Z bosons. The boosted jets are required to have a Softdrop [121] mass of more than 50 GeV.

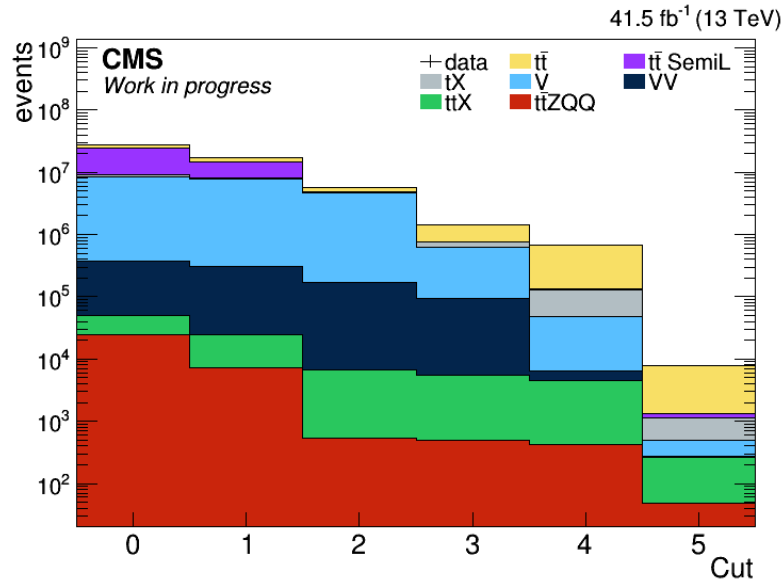


Figure 7.1: The expected number of events from simulation for the year 2017, after each applied cut in the analysis. Cut 0 refers to no explicit selection, cut 1 after the trigger selection, cut 2 indicates two leptons, cut 3 is the cut on the dilepton mass to veto events from the Drell-Yan process, cut 4 selects on one b jet and the final cut 5 includes only events with also one boosted jet.

Like AK4 jets, boosted jets with a lepton inside the cone radius are rejected in favour of the lepton.

7.2 Event Selection

Based on the physics object definitions described above, this section describes the event selection criteria defining the signal region of the analysis.

7.2.1 Trigger selection

In the CMS Experiment, the number of leptons identified at trigger level, among other criteria, determines in which dataset a given event is recorded. Events with leptons are selected by different HLT trigger paths, that can be classified into single-lepton triggers (single-electron, single-muon) and dilepton triggers (double-muon, double-electron, electron-muon). In this analysis, datasets from dilepton triggers are used. Two electrons are required to have a transverse momentum of at least 23 and 12 GeV. In addition, double-electron triggers requiring higher transverse momenta with electrons with different criteria for tracks or isolation are used. This ensures a high efficiency. This strategy

is also employed for the double-muon and the electron-muon triggers. For the two-muon dataset, minimal triggering requirements are a transverse momentum of 17 and 8 GeV. For the electron-and-muon dataset, at least 23 and 8 GeV are required.

In order to mitigate inefficiencies of the two-lepton triggers, also single-lepton triggers are used. These require one electron or one muon with a transverse momentum of at least 25 GeV (electron) or 24 GeV (muon).

Triggers are not mutually exclusive. One event can be selected by several triggers. For example, a muon with a transverse momentum of more than 50 GeV could cause all single-muon triggers to select the event, as well as several of the double-lepton triggers if another lepton is present. In this case, it is ensured that no events are counted more than once.

7.2.2 Leptons

The $t\bar{t}Z$ signal process is expected to yield two leptons, originating from the top quark-antiquark system. Each event considered in the analysis is required to have exactly two leptons. To avoid inefficiencies in the trigger selection, the minimal transverse momentum is chosen to be slightly higher than the minimal triggering requirement. The first lepton, i.e. the one with higher p_T , is required to have a transverse momentum of at least 24 GeV, the second lepton is required to have at least 18 GeV.

Two leptons can also originate from leptonically decaying Z bosons, which occur in several background processes, e.g. the Drell-Yan process or also $t\bar{t}Z$ with a leptonically decaying Z boson. It is therefore necessary to veto leptons originating from Z bosons instead of the top quark-antiquark system. Events with same-flavour lepton pairs with a combined mass closer than 10 GeV to the Z boson mass are therefore excluded from the selection. Prompt leptons, i.e. leptons that originate from the primary vertex, can also originate from pileup or QCD events. These leptons usually have a low combined mass, while dilepton pairs from $t\bar{t}$ decays tend to have a high mass between 50 and 300 GeV. This background is excluded by applying a cut on events with a combined dilepton mass of less than 40 GeV.

7.2.3 Jets and b jets

Jets (with the requirements stated in section 7.1.2) play an important role in the analysis. In leading order, the dileptonic $t\bar{t}Z$ signal process is expected to have two AK4 jets. Both of these jets originate from b quarks produced in the decays of the top quarks. It is not unlikely, however, that a real b jet is not identified as such. Also, some jets escape detection for various possible reasons, such as their p_T being below the minimal requirement or limits in the detector acceptance. This can be seen in figure 7.2. The figure shows the simulated distribution of identified jets and b jets for the signal process. Most events show only one b jet. Therefore, in this analysis, only one b jet is required in

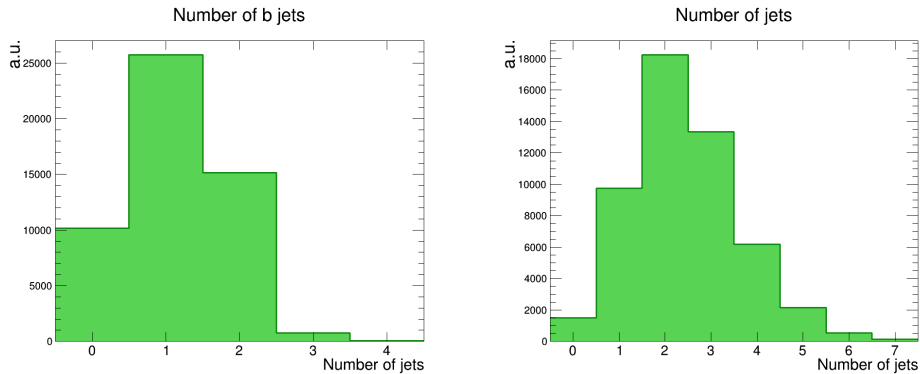


Figure 7.2: Multiplicity distributions of reconstructed jets and b jets in a simulated signal sample. Even though two b jets are expected from the leading order process, in a large fraction of the events only one or even zero b jets are reconstructed. Therefore, only one b jet is required in the signal region.

the signal region. There are also events with zero b jets. However, these are discarded, as a selection without b jets would also include too many background processes without top quarks. In the leading order signal process, no other AK4 jets besides the two b jets are expected. Therefore, no further requirements on non b-tagged jets are made.

7.2.4 Boosted jets

The $t\bar{t}Z$ signal process contains one hadronically decaying Z boson with a high transverse momentum. This boson is identified by the presence of a boosted jet, fulfilling the requirements described above. In background processes, boosted jets occur due to QCD radiation or due to the superposition of non-boosted jets. This also affects the signal process, and signal events with more than one boosted jet can occur. In this analysis, however, only events with exactly one boosted jet are considered for the signal region.

A minimum p_T of 200 GeV is chosen as threshold. This threshold is set about 20 GeV above the minimal requirement for the two jets from the boson to form a boosted jet. This guarantees a good reconstruction efficiency, while at the same time, it is low enough to not lose too great an amount of signal. However, it can be argued that a higher threshold increases the purity in the signal region, as boosted jets from background sources tend to have a lower p_T than true boson jets. The effect of the choice of p_T threshold value is therefore one of the sensitivity studies presented in chapter 12.

PROCESSES AND SIMULATED SAMPLES

Other than the $t\bar{t}Z$ signal process, several irreducible background processes are present in the signal region. The main background process is dileptonic $t\bar{t}$ production, due to its large cross section. Also, other $t\bar{t}+X$ processes such as $t\bar{t}H$ or $t\bar{t}W$ play an important role.

This section provides an overview of the most important background processes. The contribution to the signal region of each process as well as the distributions of the events in different observables, including the DNN inputs and classifier, are monitored using simulated samples.

For each process, four separate samples are available, corresponding to the four data-taking eras used in the analysis. These eras mainly correspond to the data-taking years, with 2016 split into two parts, due to a major change in the tracker settings. The eras are

- 2016, before the change in tracker settings (further called 2016 preVFP), corresponding to 19.5 fb^{-1}
- 2016, after the change in tracker settings (further called 2016 postVFP), corresponding to 16.8 fb^{-1}
- 2017, corresponding to 41.5 fb^{-1}
- 2018, corresponding to 59.8 fb^{-1}

8.1 The Signal Process $t\bar{t}Z \rightarrow q\bar{q}$

The signal process is top quark pair production in association with a Z boson, $t\bar{t}Z$. In this analysis, the specific decay channel with the top quark pair decaying into two leptons and the Z boson decaying hadronically is studied. Only high- p_T Z bosons forming a boosted

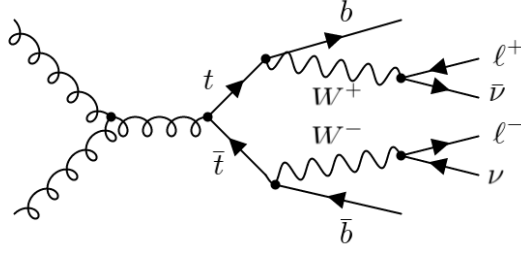


Figure 8.1: An example Feynman graph for dileptonic $t\bar{t}$ production, including the top quark decay chains.

jet are considered as signal. A detailed description of the signal process can be found in section 2.4.

The simulated samples for the signal process are generated at NLO accuracy using the MadGraph5_aMC@NLO generator [122]. The parton shower is simulated using Pythia8 [123]. The detector simulation is done with GEANT4 [124] for the signal sample as well as for all other samples.

The $t\bar{t}Z$ signal samples are simulated inclusively in $t\bar{t}$ decays. For Z bosons, only hadronic decays are included, with no minimum p_T requirement for the Z bosons. The samples contain 46.3 million events in total, divided into 6.39 million events for 2016 preVFP, 5.80 million for 2016 postVFP, 14.2 million for 2017 and 20.0 million for 2018. In total, from these events, about 100,000 contribute to the signal region.

From the total number of expected events (normalised to the luminosity of the corresponding data) in the signal region, about 0.6 % originate from the $t\bar{t}Z$ signal.

8.2 Top Quark Pair Production

The dominant background process is $t\bar{t}$ production. This mainly includes dileptonic $t\bar{t}$ production, with a contribution of approximately 85% in the signal region. An example Feynman graph of this process can be seen in figure 8.1.

Also, semi-leptonic $t\bar{t}$ events, which pass the event selection when another detector signature is wrongly identified as a second lepton, are present. The semi-leptonic channel accounts for 2.7% of the events in the signal region. The fully hadronic channel does not significantly contribute to the signal region. The dileptonic and semi-leptonic channels are simulated as separate samples. Both sample types are simulated using PowHeg [125–127] with the parton shower being simulated using Pythia8. Approximately 346 million simulated dilepton events are available, as well as about 1.15 billion semi-leptonic events.

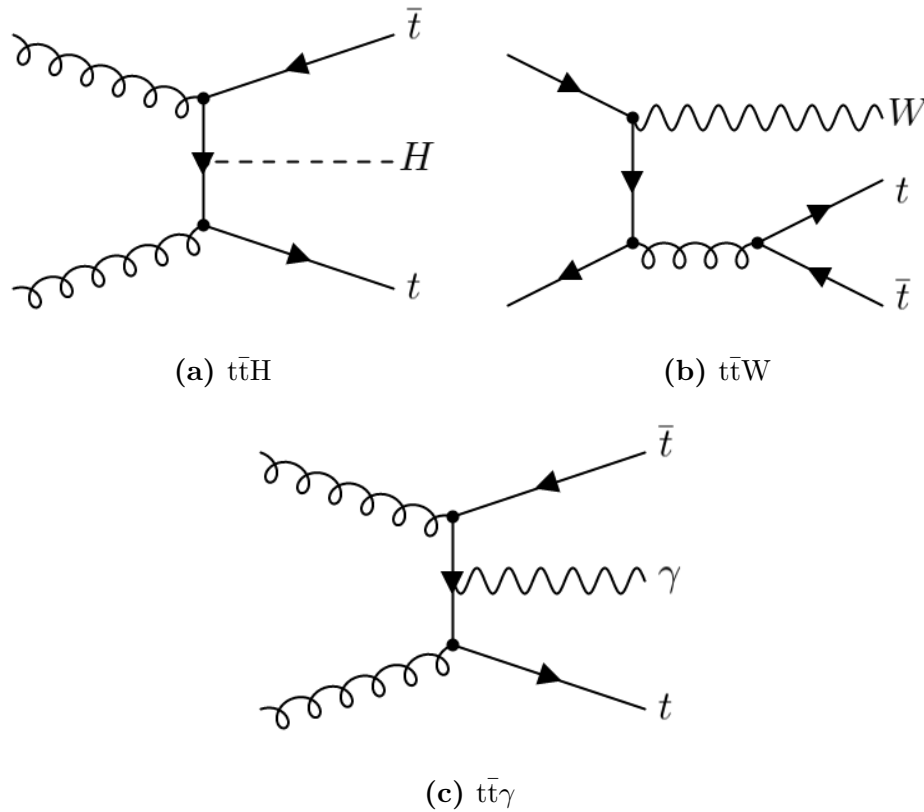


Figure 8.2: Example diagrams for $t\bar{t}+X$ processes. In general, the production modes are similar to those of $t\bar{t}Z$ production.

The signal region contains about 600,000 simulated dileptonic events as well as 16300 semi-leptonic events.

8.3 Other Top Quark Pair Processes

The $t\bar{t}X$ category contains all processes that have a boson produced in association with a $t\bar{t}$ pair. This includes $t\bar{t}H$, $t\bar{t}W$, $t\bar{t}\gamma$ as well as $t\bar{t}Z$ with leptonically decaying Z bosons. In combination, these processes contribute about 1.7% of the events in the signal region. Example Feynman graphs for these processes can be found in figure 8.2. In general, the production modes are similar to those of $t\bar{t}Z$ production. This leads to a highly similar event signatures, especially for $t\bar{t}H$ and $t\bar{t}W$ as Higgs and W bosons have a mass similar to the Z boson and also have hadronic decay channels.

All $t\bar{t}+X$ samples are simulated using the MadGraph5_aMC@NLO generator, as is the

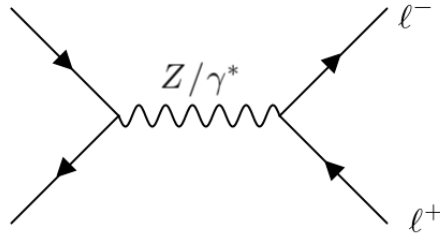


Figure 8.3: Feynman graph of the leading order Drell-Yan process.

signal sample. The available samples for $t\bar{t}H$ are split into one sample with the Higgs boson decaying into a $b\bar{b}$ pair and one for all other Higgs boson decays. The $t\bar{t}+W$ samples are divided into one sample with leptonic and one sample with hadronic W decays. All the $t\bar{t}+X$ samples are simulated with inclusive top quark decays.

The cross sections of the $t\bar{t}+X$ processes have been measured by the CMS and ATLAS experiments. For $t\bar{t}H$ [20–22, 128–130], the latest cross section measurement has an uncertainty of about 30%. For $t\bar{t}\gamma$, [40, 131, 132], the uncertainty on the cross section measurement is about 4%. The uncertainty for $t\bar{t}W$ [41] is about 23%, for $t\bar{t}Z$ to leptons [43] about 8%.

8.4 Other Backgrounds

Several other processes provide small contributions to the events in the signal region. While the total contribution is larger than the contribution of processes of the $t\bar{t}X$ category, these processes play a smaller role, since they can be separated from the signal more easily. The processes included in this category are the Drell-Yan process [133], single top quark production [134, 135] and diboson production [136–138]. They are combined into an "other backgrounds" category for the cross section measurement, to reduce statistical errors in the fit. As the cross sections of these processes have been measured with a good accuracy, the uncertainty is assumed to be 10%.

8.4.1 The Drell-Yan process

In the Drell-Yan process, two fermions interact via a photon or a Z boson to form again two same-flavour fermions. In case of leptonic decays, this can lead to a contribution to the signal region, when additional jets are produced, as expected in higher order processes. A Feynman diagram of the leading order Drell-Yan process with leptons in the final state can be seen in figure 8.3.

Even though the Drell-Yan process can only contribute in higher order, the large cross section of the process around the Z boson mass leads to a significant amount of events

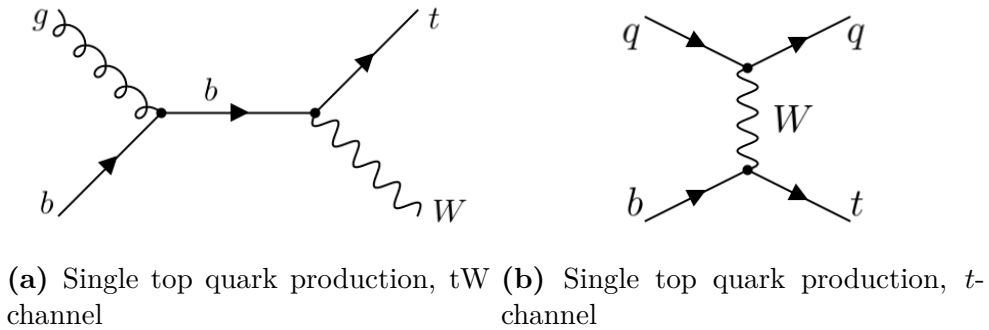


Figure 8.4: Feynman diagrams for the single top quark processes included in the analysis

passing the baseline selection. In order to counter the contribution from Drell-Yan events, events with lepton pairs with a mass inside the Z window, between 80 and 100 GeV, are removed from the signal region. With this cut applied, the Drell-Yan process still contributes about 2.8% of the events in the signal region.

The standard simulated samples for the Drell-Yan process do not provide a sufficiently large number of events with the high amount of additional hadronic interaction needed in the signal region. For this reason, specific simulated samples are used that are produced to provide a higher amount of events with high transverse hadronic energy. These samples provide about 32700 simulated events in the signal region.

8.4.2 Single top quark production

Events in which a single top quark is produced can also provide a contribution to the signal region, if an additional lepton candidate is present. The contributing events can originate from single top quark t -channel production (Feynman graph in figure 8.4(b)) or from tW production (Feynman graph in figure 8.4(a)), with the tW channel being dominant.

Five separate simulated samples per year are used to describe these events – t -channel events are separately produced for electrons, muons and taus originating from the leptonic top quark decay. Events with hadronic top quark decays are not included in these samples, however, they are also not expected to contribute due to the lack of leptons. The tW events are produced as one sample with top quarks and one with top antiquarks. For tW events, all W decay channels are included.

Single top quark events make up about 6.8 % of the events in the signal region.

8.4.3 Diboson production

In diboson events, a pair of vector bosons is produced. Diboson events can contribute to the background, e.g. if one of the bosons decays leptonically and the other hadronically.

Table 8.1: The numbers of expected events from simulation for the signal and the background processes in the signal region, for the different analysis years, as well as for all years combined (Run 2).

Process	# events					Relative contribution (in %)
	2016 preVFP	2016 postVFP	2017	2018	Run 2	
$t\bar{t}$ dileptonic	2850	2587	6381	9072	20890	85.4
$t\bar{t}$ semi-leptonic	55	95	209	308	667	2.73
Single top	284	257	646	471	1658	6.78
Drell-Yan	97	87	211	296	692	2.83
Diboson	3	6	11	13	32	0.13
$t\bar{t}Z(\ell\ell)$	17	15	37	53	121	0.49
$t\bar{t}W$	28	26	62	92	208	0.85
$t\bar{t}H$	11	21	24	35	90	0.37
$t\bar{t}Z q\bar{q}$	20	17	43	62	143	0.58

This process contributes to about 1% of the events in the signal region. Three simulated samples are included in the analysis in order to take the contribution of diboson events into account. One sample is included for each combination of vector bosons – WW, WZ and ZZ. These samples are inclusive in the vector boson decay channels.

CLASSIFICATION WITH A DEEP NEURAL NETWORK

After the selection of events described in the previous chapter, the signal process only contributes a very small fraction of events (0.6%) to the signal region. In order to reach a significance high enough to measure the cross section of $t\bar{t}Z$ with hadronic Z boson decays, further purification of the signal is needed. However, there is no simple physical observable that can achieve such separation. Therefore, a multivariate classifier observable is created, incorporating small differences between signal and background in several physical properties to create a high signal purity in high values of the classifier. This is done using an artificial Deep Neural Network (DNN). The DNN is developed using the TensorFlow [139] framework and keras [140].

Several observables displaying differences between the simulated background and signal samples are used as inputs to train the neural network. A binary classification is chosen, with two output classes signifying signal and background. With above 85% contribution to the signal region, dileptonic $t\bar{t}$ production is by far the largest background. Therefore, dileptonic $t\bar{t}$ is the only background considered in the training.

This chapter describes the development and results of the DNN training. The samples that were used for the training are described in section 9.1, the input variables are discussed in section 9.2, and the setup of the DNN is shown in section 9.3. The resulting final classifier which is then used as a discriminating variable to measure the cross section of $t\bar{t}Z$ is presented in section 9.4.

During the work on the analysis it became evident that an approach using two separate DNN models, one for events with exactly one b jet (1b category), and another for events with more than one b jet (2b category), results in a better agreement between data and simulation in the final classifier. Therefore, two separate models are trained. The two models use the same training samples and general setup and only differ in a small number of input variables. The following discussion remains true for both models, unless specifically stated otherwise.

Table 9.1: The numbers of simulated events used in the DNN training process for the different analysis eras

Process	Number of events
$t\bar{t}$ dilepton	223294
2016 preVFP	36382
2016 postVFP	43414
2017	93425
2018	129869
$t\bar{t}$ dilepton + $Z \rightarrow q\bar{q}$	252577
2016 preVFP	36381
2016 postVFP	47582
2017	103332
2018	149244

9.1 Training Samples

In order to avoid bias in the measurement, the simulated samples used for the analysis should be independent of the samples that are used to train the DNN. In many analyses, this is achieved by splitting the simulated samples in two parts, one that is only used for the analysis and one that is used exclusively for training the DNN. For this analysis a slightly different approach can be chosen, as, for the signal process, dedicated samples for the training are available. These samples include simulated $t\bar{t}Z$ events with hadronic Z bosons and – other than the signal samples used in the analysis – with dileptonic $t\bar{t}Z$ events only. Separate samples for each of the four eras are available. About 250k events are present in the signal region and used for the training process.

For the background, no specific training sample is available and the available $t\bar{t}$ dilepton samples are split. As these samples contain a very high number of events also in the signal region, this split does not cause any loss of statistical strength either in the analysis or in the training. About 50% of each sample are chosen to be used for the DNN training process. This results in about 220k events in the signal region. A summary of the number of events available for each year can be found in table 9.1.

Of these datasets, both for signal and background, 50% are used to train, i.e. to minimise the loss function of the model, and 30% are used for validation, to check during the training if the loss also decreases with an independent dataset. The remaining 20% of the data are used for testing, to investigate if the model behaves as expected on a dataset which has not been used in the training at all.

To maximise classification power, it is necessary to select only the events which best describe the signal. To suppress combinatorial background from signal events, only the

events where the reconstructed boosted jet matches the generated Z boson are included in the training. This is done by requiring that the opening angle ΔR between the generated Z boson and the boosted jet be smaller than 0.2.

9.2 Input Variables

For the training of the model for the 1b category, 30 variables were used, 34 variables were used for the model for the 2b category. These include both high-level and low-level variables and were chosen from a larger set of variables based on their impact on the final training, shown in section 9.4 and due to their good agreement with the data, shown in section 11. Comparisons of the distributions of each variable for signal and background are shown in figures 9.1 - 9.5.

- **Variables related to the boosted jet:**

ZvsQCD This variable is provided by the ParticleNet tagger, described in section 4.3.3. It describes the probability that a boosted jet originates from a Z boson rather than a superposition of QCD jets. It is calculated as the ratio of the sum of all Z boson output classes and the sum of all QCD output classes as:

$$ZvsQCD = \frac{Z(bb + cc + qq)}{QCD}$$

The tagger is trained in such a way that this ratio results in an output between 0 and 1. Jets originating from a boosted Z boson ideally have a value close to 1, QCD jets close to 0.

Softdrop mass Mass of the boosted jet, reconstructed with the Softdrop algorithm [121]. Boosted jets from background have a steeply falling mass spectrum, while the Z boson spectrum peaks at the Z mass.

fatjet p_T The transverse momentum of the boosted jet.

- **Variables regarding the event without the boosted jet:**

Jet multiplicity The number of AK4 jets in the event. The signal process is expected to yield more extra jets compared to $t\bar{t}$ background events.

b jet multiplicity The number of b tagged jets in the event. As this number is always 1 in the first category, this input is only used for the 2b category.

Dilepton p_T The transverse momentum of the dilepton system, i.e. the sum of the four vectors of the two leptons in the event. This input is expected to provide sensitivity due to the different kinematics in the $t\bar{t}$ system when an additional vector boson is present.

$\Delta R_{\ell\ell}$ The opening angle ΔR between the two leptons in the event. As for the dilepton p_T , this input is expected to provide sensitivity due to the different kinematics in the $t\bar{t}$ system.

$\Delta R_{b\bar{b}}$ The ΔR of the two b jets in the event, in case the event has two b jets. In the very rare cases of three or more b jets in the event, the ΔR of the b jets with the highest transverse momentum. This input is only used in the model for the 2b category.

$\Sigma \Delta R$ Min JetLepton For both leptons, the closest AK4 jet (meaning the jet with the smallest ΔR between it and the lepton) is found. This variable is the sum of the ΔR values of the leptons to their respective closest jet.

avg. b jet p_T The sum of the transverse momenta of all b jets in the event divided by the number of b jets. As this is identical to the p_T of the b jet for 1 b events, this input is only used in the model for the 2b category.

Four vectors of analysis objects p_T, η and ϕ of the jet and b jet with the highest transverse momentum, as well as from both leptons in the event. The components of the four vectors are supplied as separate variables. Some of these inputs do not show any separation on their own. They can, however, be useful since the complete information about the four vectors is provided.

- **Variables regarding the complete event:**

$\Sigma \Delta R$ ℓ fatjet The sum of the opening angles ΔR between the first lepton and the boosted jet and between the second lepton and the boosted jet.

avg. ΔR Jet fatjet The sum of the ΔR of each AK4 jet in the event to the boosted jet, divided by the number of AK4 jets.

ΔR b fatjet The ΔR between the b jet with the highest transverse momentum in the event and the boosted jet.

Σ fatjet & b jet p_T The sum of the transverse momenta of the boosted jet and all b jets in the event.

ΔR b ℓ_X fatjet The opening angle ΔR between the boosted jet and the combined system of a lepton and the closest b jet to this lepton. This information as added by two inputs, one for each lepton.

Aplanarity, Sphericity, C Event shape variables as described in section 4.6, as well as the fourth Fox-Wolfram moment $R(4) = \frac{H(4)}{H(0)}$.

MET The missing transverse energy of the event

During the development process of the DNN, many different possible input variables were analysed. Many were rejected due to a lack of separation power and dropped early in

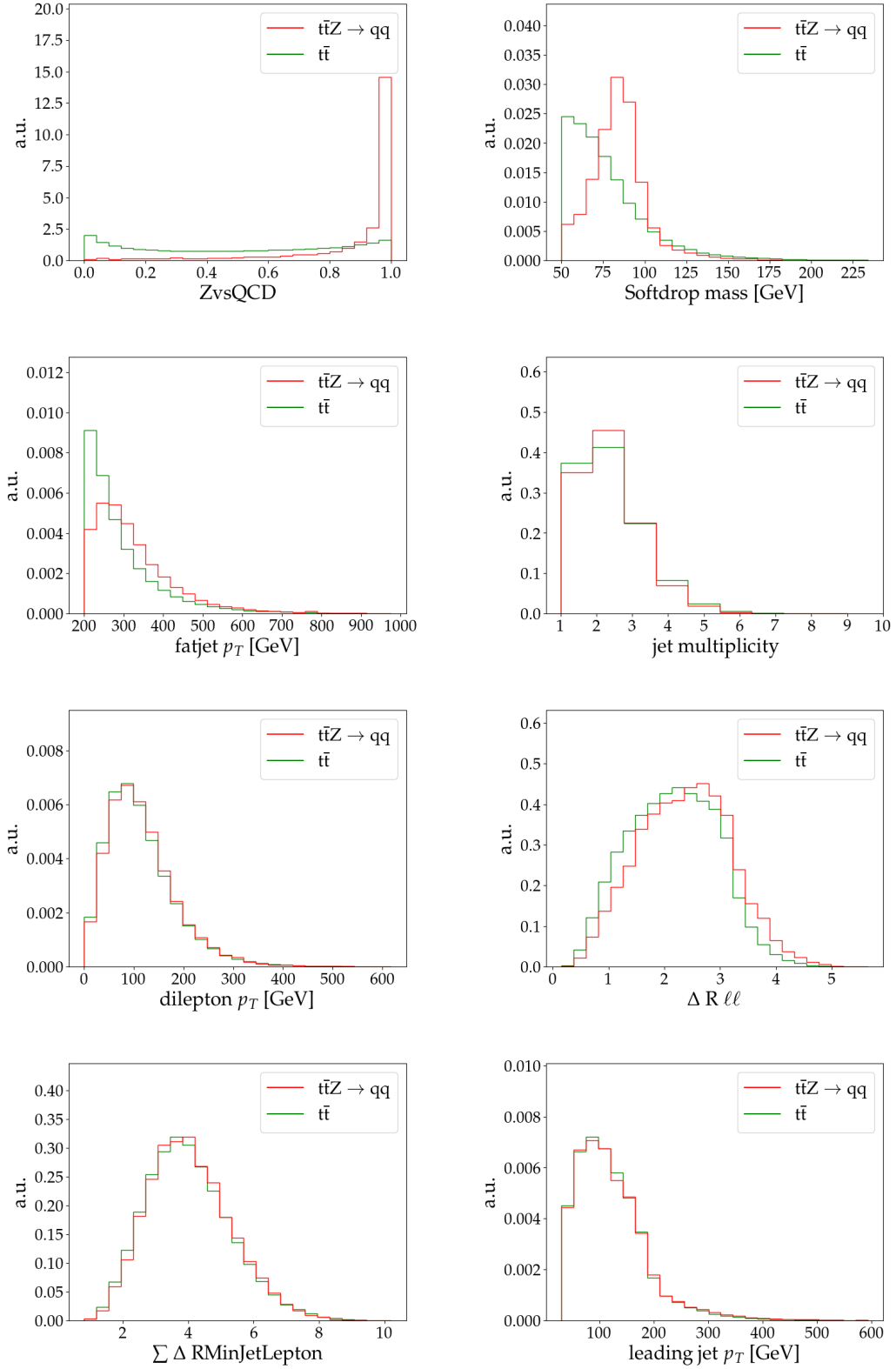


Figure 9.1: Input variables for the training of the DNN classifier: the three variables related to the boosted jet: The value of the $Z_{vs}QCD$ classifier, as well as the p_T of and the Softdrop mass of the boosted jet. In addition, five variables of the second category: The number of jets, the sum of the p_T of the two leptons, the ΔR between the two leptons, the sum of ΔR between each lepton and the respectively closest jet, and the p_T of the leading jet. The signal distribution is displayed in red, the background is shown in green.

the development process. Three inputs that are not in the final model are nevertheless worth mentioning, as they show a high separation power, but had to be excluded due to mismatch between simulation and data. These inputs are:

ParticleNet_ZvsTop Analogous to the ZvsQCD variable, the ParticleNet tagger also offers a binary classifier separating boosted jets from hadronic top quark decays from QCD background (TopvsQCD). The ratio between the two classifiers is used as an input.

Even though neither the analysis signal nor the training background, which is only dileptonic top quark pair production, contains hadronically decaying top quarks, this variable shows good separation power.

ParticleNet_b Like ParticleNet_ZvsTop, this observable is created from ParticleNet outputs. In this case, the raw output values for the QCD output classes are used. The QCD_b output, defined to select jets with a b quark, is divided by the sum of all other QCD output classes. This can provide sensitivity, as many of the non-Z boson boosted jets contain one of the b jets from the top quark decays.

This approach works very well using simulation only. However, this input, as well as the previous one, show bad agreement between data and simulation and therefore cannot be used.

Subjettiness τ_{21} The subjettiness variable τ_N [95] is one of the most basic approaches to analyse boosted jets. It describes the compatibility of a boosted jet with the hypothesis of N subjets. $\tau_{21} = \frac{\tau_2}{\tau_1}$ compares the compatibility with exactly 2 subjets, (expected for hadronic W and Z boson decays), with the compatibility with one subjet (expected for QCD jets).

However, τ_{21} is not expected to provide much additional sensitivity as all the information is also included in the particle cloud input to ParticleNet_ZvsQCD. In addition, a slight discrepancy between data and simulation can be seen for some eras. It was therefore decided to exclude τ_{21} from the final analysis.

The variables used to train the classifiers are not all completely uncorrelated. The correlation matrix for the signal process, displaying all variables for the model for the 1b category, can be seen in figure 9.6. While most variables show little to no correlation, the number of jets and b jets is obviously correlated. The four event shape variables are also highly correlated amongst each other, and the ZvsQCD classifier is not uncorrelated of the Softdrop mass of the boosted jet. This is not problematic, however, as a DNN is able to take correlations into account.

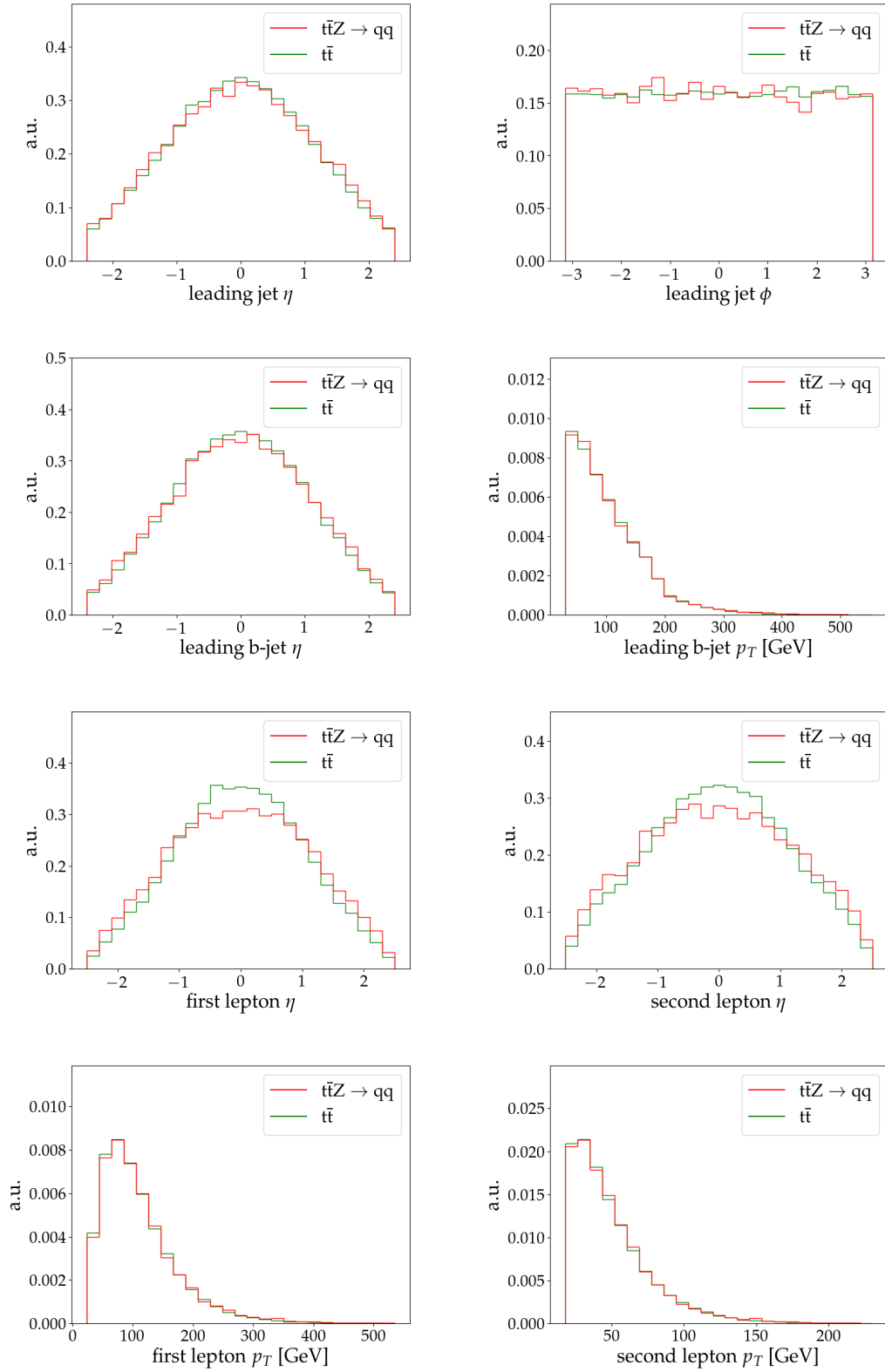


Figure 9.2: Input variables for the training of the DNN classifier: four-vector components p_T and η of jets, b jets and the two leptons. The ϕ distribution is only shown for the first jet, as it is a flat distribution in every case. The signal distribution is displayed in red, the background is shown in green.

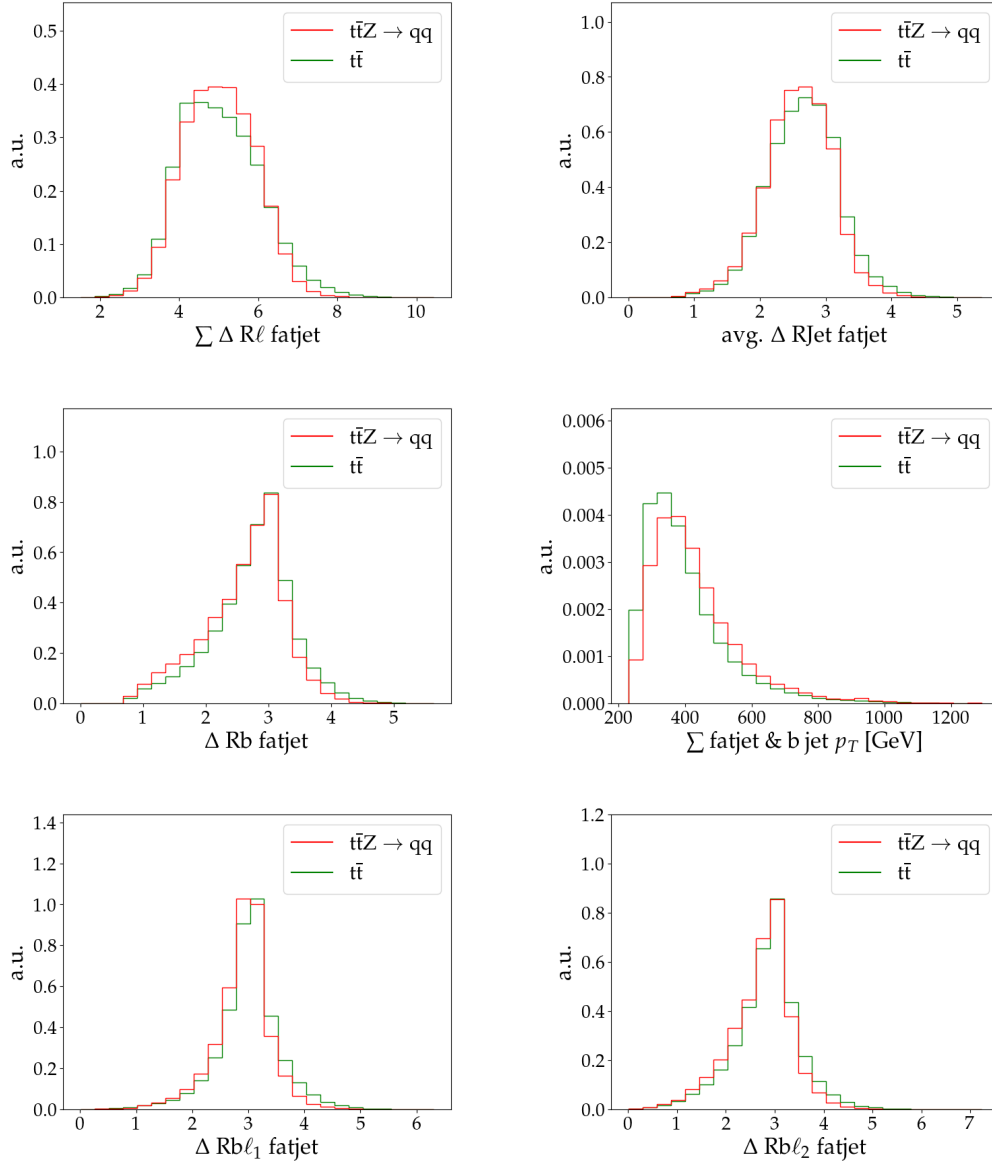


Figure 9.3: Input variables for the training of the DNN classifier: the sum of the ΔR between the leptons and the boosted jet, the average ΔR of an AK4 jet to the boosted jet, the ΔR between the (first) b jet and the boosted jet, the sum of the p_T of all b jets and the boosted jet as well as the ΔR between the b-and-lepton systems and the boosted jet. The signal distribution is displayed in red, the background is shown in green.

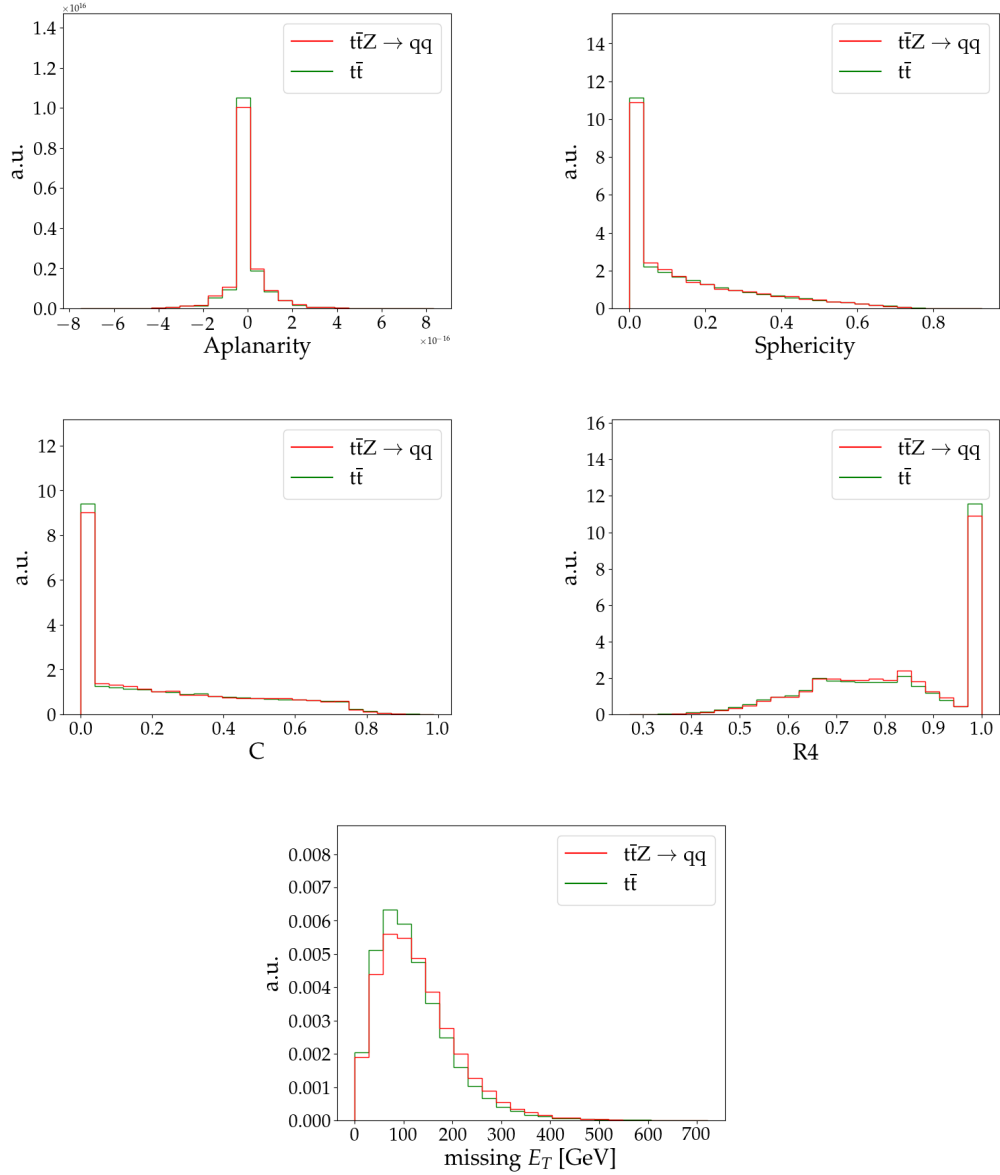


Figure 9.4: Input variables for the training of the DNN classifier: the event shape variables aplanarity, sphericity, C, and R4, as well as the missing transverse energy of the event. The signal distribution is displayed in red, the background is shown in green.

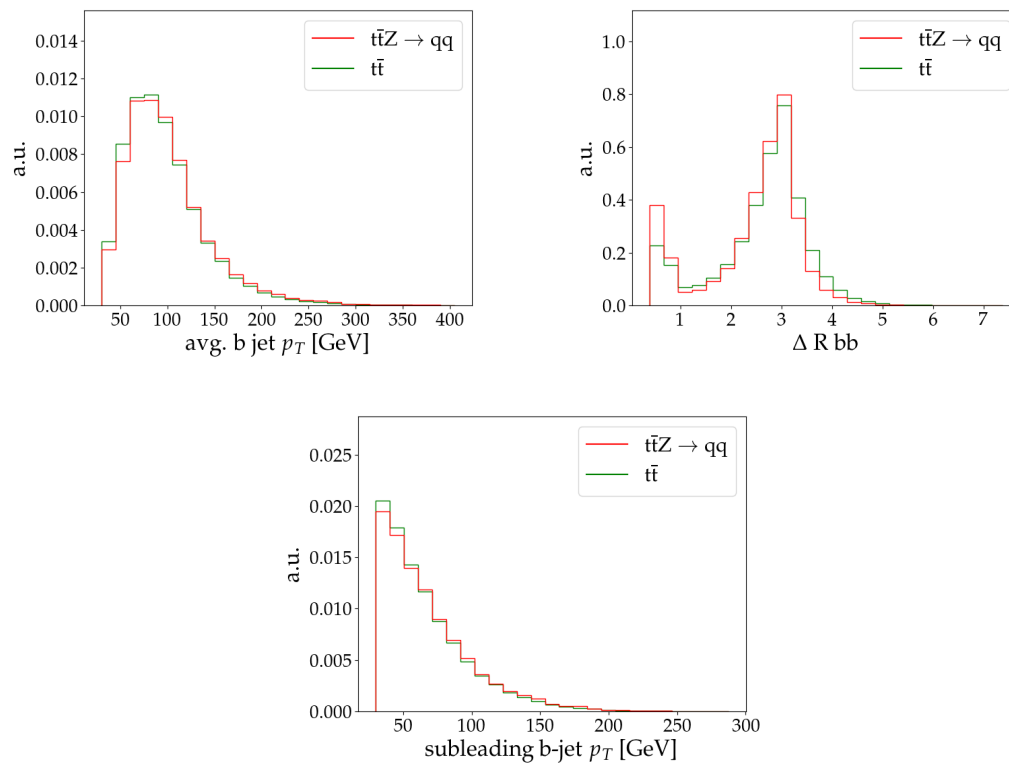


Figure 9.5: Input variables for the training of the DNN classifier, for events with two or more b jets: the average b jet p_T , p_T of the second b jet, and the ΔR between the two b jets. The signal distribution is displayed in red, the background is shown in green.

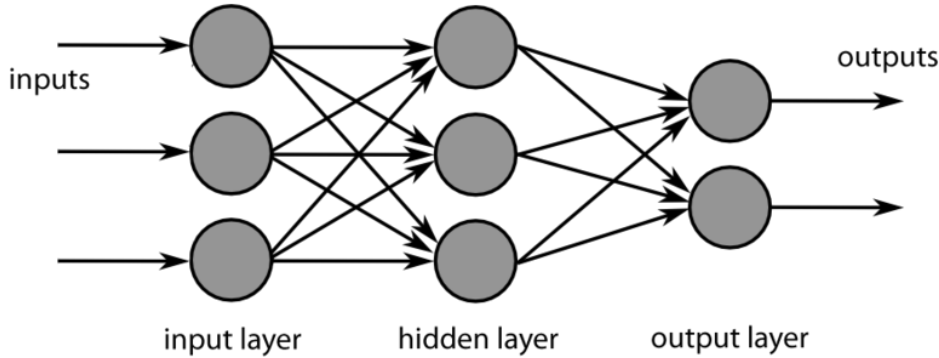


Figure 9.7: Basic structure of a deep neural network architecture. The first layer consists of a node for each input feature, from which the features are propagated through a number of hidden layers (in this case one). The neurons in each layer are connected to each node in the next layer. The final layer describes the output classes. Figure taken from Ref. [143].

9.3 Hyperparameter Optimisation

Hyperparameters describe the configuration for network architecture and training. In order to achieve an optimal separation between signal and background, many different hyperparameters must be optimised. In this section, the choices for the most important hyperparameters are shown. The primary feature that is optimised is the loss of the trained model, as well as its "receiver operator characteristic" (ROC) curve. A lower loss and a lower area under the ROC curve is a measure of how many of the events are classified correctly, and therefore a measure of how well the model separates signal from background. Both values are calculated on the validation dataset.

Another important quality criterion, to verify if the classifier can be used for physics analyses, is the agreement between simulation and data. Theoretical calculations never describe nature with perfect accuracy. Since the model can only be trained on simulation, it should be verified that it describes the data correctly. The data-to-simulation agreement of input variables and final classifier is described in chapter 11.

The network is set up and trained using the TensorFlow framework. Binary cross entropy [141] is used as loss function. For the minimisation of the loss function, the ADAM optimiser [142] is used.

Network Architecture A basic Feed Forward Network, as it is used in this thesis, consists of one input layer, with a node for each input feature, a number of hidden layers as well as an output layer describing the output classes. A depiction of this setup can be seen in figure 9.7.

The number of hidden layers as well as the number of nodes (neurons) per layer defines the complexity of the trained model. While a too simple model may not be able to describe

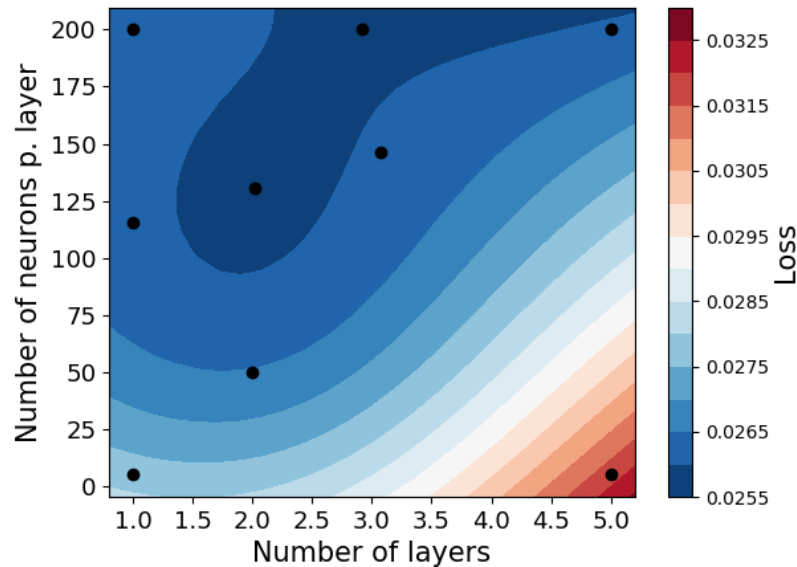


Figure 9.8: 2D contour of the loss as a function of the number of layers and neurons that is achieved in the training. Each of the black dots shows one trained model. The shaded areas denote estimations of the probable loss based on the losses achieved in these models.

the data, highly complex models are more susceptible to overtraining.

In order to choose the appropriate model complexity, nine different networks were trained using the same input data. For each network, a different number of hidden layers (ranging from 1 – 5) and a different number of neurons per layer (ranging from 5 – 200) were chosen. The achieved minimal losses are summarised in a 2D plot in figure 9.8. The shaded areas denote estimations of the loss based on the losses as achieved in the models, denoted by black dots. To avoid overtraining, the model chosen should be as simple as possible. From the optimisation, a model with two hidden layers and 125 neurons per layer is chosen.

Learning Rate The learning rate defines how much the model changes after each iteration (epoch). A too high learning rate can cause the optimisation to exceed the minimum and not converge. However, with too low a learning rate, the optimisation might not find a minimum even after a large amount of epochs or converge to a local minimum instead of the global one.

As for the network architecture, several models were trained to optimise the learning rate. As the ADAM optimiser adjusts the learning rate of the model during the training, no strong dependency on the starting value is expected. This optimisation was done in combination with the batch size. No strong dependency of the two factors is observed. The 2D contour showing the optimisation can be seen in figure 9.9. A good choice for the

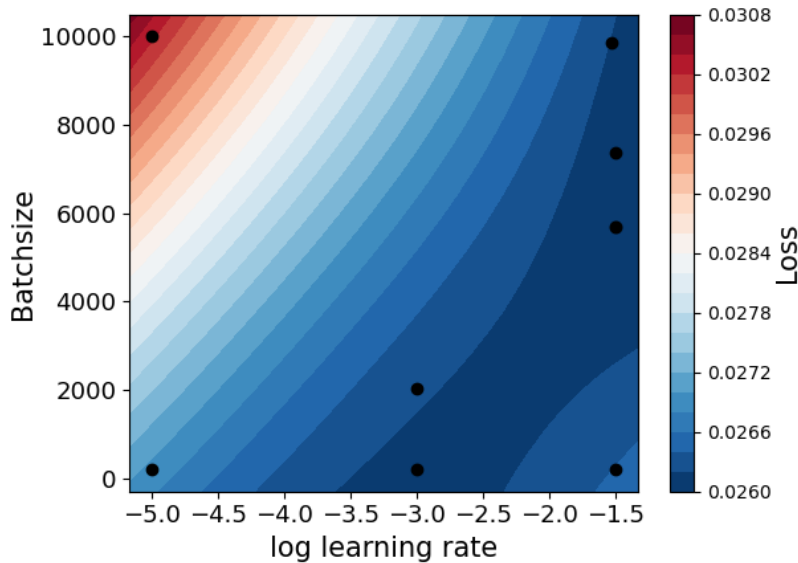


Figure 9.9: 2D contour of the loss as function of batch size and learning rate. Each of the black dots shows one trained model. The shaded areas denote estimations of the probable loss based on the losses achieved in these models.

learning rate ranges between 10^{-2} and 10^{-4} , with little to no differences of the achieved loss observed between these values. For the final training, 10^{-3} was chosen for the learning rate.

Batch size The batch size signifies how many samples of the dataset are used to optimise the loss function in each step. Since the complete training dataset is used for each epoch of the training, a smaller batch size increases the time needed for training the model. In the optimisation, no effect on the achieved loss can be seen when varying the batch size between 200 and 10,000. However, a smaller batch size usually leads to more stable models, with better generalisation ability [144]. Therefore, a relatively small batch size of 500 is chosen to train the final model.

Choice of training areas In order to achieve the best possible result, the data used in the training should behave uniformly across the whole dataset used in the training. However, the training data might display slight differences in the different training samples. Also, the categorisation into 1b and 2b events that is applied in the analysis should be taken into account. It is possible, that one model that it is trained on the complete sample does not lead to as good a result as specialised models for different areas. Splitting in too many training areas however, can lead to statistical limitation, as there are too

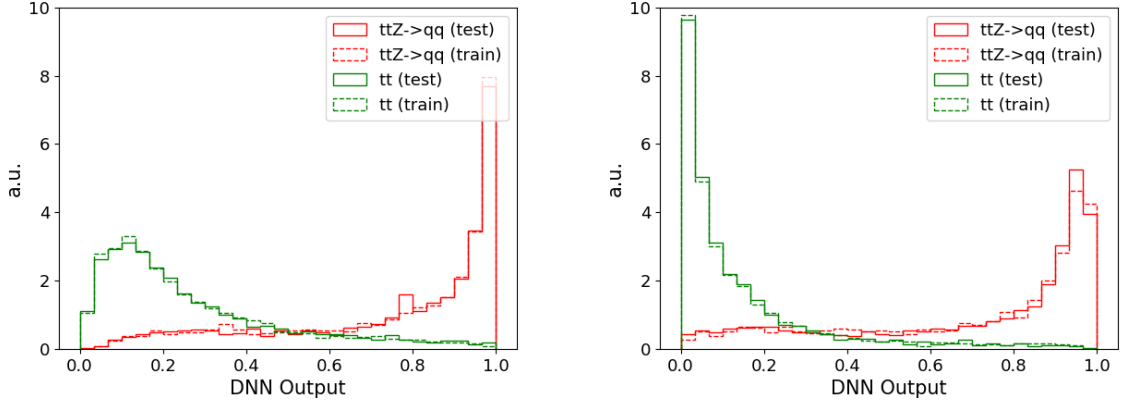


Figure 9.10: Output distributions of the final DNN models: for events with exactly one b jet on the left and for events with two or more b jets on the right. The $t\bar{t}$ background is displayed in green, the $t\bar{t}Z$ signal is displayed in red. Solid lines denote the test samples, dashed lines show the distribution of the training samples.

few events available per area. Both, separate models for the different eras, and separate models for the 1b and $>2b$ categories have been compared to an approach with only one model for the complete dataset.

Training separate models for the different eras leads to very similar results for each model. The area under the ROC curve (AUC) of the separate models are similar or slightly worse than the AUC of a model trained on the complete dataset. Also, no improvement of the data-to-simulation agreement can be observed when training separate models. Therefore, no separation between the eras is applied.

When training models for events with exactly one b jet separate from those events with two or more b jets, the two models display differences. The distributions of signal and background differ in shape, as can be seen in figure 9.10. The AUC for the 1b model is slightly worse than the AUC for the complete model, while the AUC for the 2b model is better. On average, the separation power for the complete dataset is similar. However, the data-to-simulation agreement for separate categories is slightly better than for training with a single dataset. Therefore, for the final training, an approach with two separate DNN models is chosen.

9.4 Training Results

As stated in the previous section, two deep neural network model were trained in order to separate $t\bar{t}$ background events from the $t\bar{t}Z$ signal events. One model is used for events with exactly one b jet (1b model), the second model describes events with two or more b jets (2b model). For both categories, a network with two hidden layers and 125 neurons

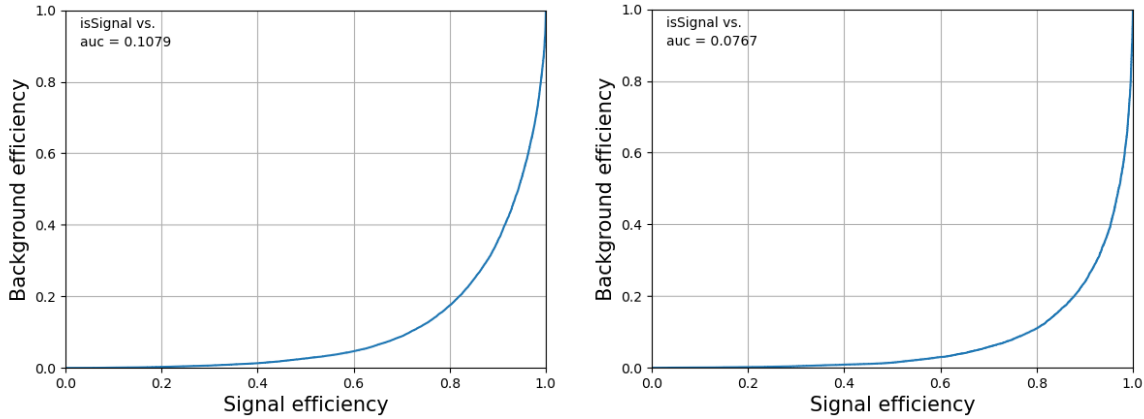


Figure 9.11: ROC curves of the final DNN models: for events with 1 b jet on the left and for events with two or more b jets on the right.

per layer is used, with a batch size of 500 samples and the starting learning rate set to 0.001.

The two networks use a slightly different set of the input variables described in section 9.2. All features that require at least two b jets (b jet multiplicity, $\Delta R_{b\bar{b}}$, p_T of the second b jet) are excluded from the 1b model. The output distributions of both models can be seen in figure 9.10. As expected, the background distributions form a peak at low values, while the signal distribution shows a sharp peak at a value of one. While the two distributions look similar, it can be observed, that for the 2b category the background forms a sharper peak, while the signal distribution is slightly broader than in the 1b category. This behaviour can also be observed in the ROC curves, displayed in figure 9.11.

No overtraining is observed. This can be seen by the fact that the validation loss for the models decreases steadily until it reaches a constant value (blue line in figure 9.12), and also by the fact that the output distributions (figure 9.10) agree between test and training datasets. The relative feature importance, as it was also used in the choice of the final training variables, can be seen in figure 9.13 for the 1b category. The feature importance is calculated via "SHAP" values [145, 146].

As expected, the most important input variable by far is the value of the Z_{vsQCD} classifier. While this is true for both categories, it is more pronounced in the 2b category. The ranking of the other variables is also similar between the two categories. Among the highly ranked variables are the p_T of the boosted jet and the two leptons, as well as the ΔR between the two leptons. The distribution of the final resulting classifier applied to the available simulated samples can be seen in figure 9.14. In this distribution, the events with one b jet are classified by the 1b model, the events with two or more b jets are classified by the 2b model, but both sets of events are displayed in the same distribution, creating one final DNN classifier. It can be seen, that the classifier for events from smaller

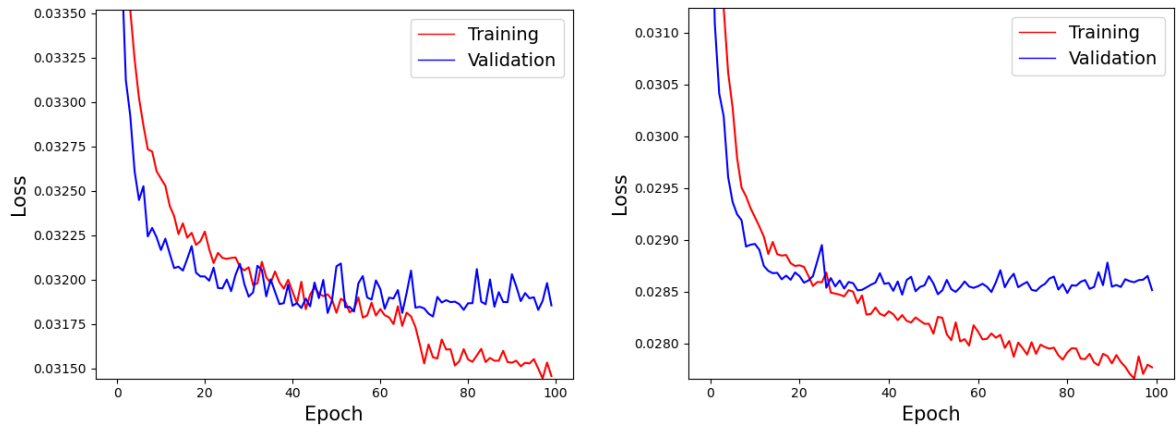


Figure 9.12: Evolution of the loss during training of the final DNN models: for events with exactly one b jet on the left and for events with two or more b jets on the right.

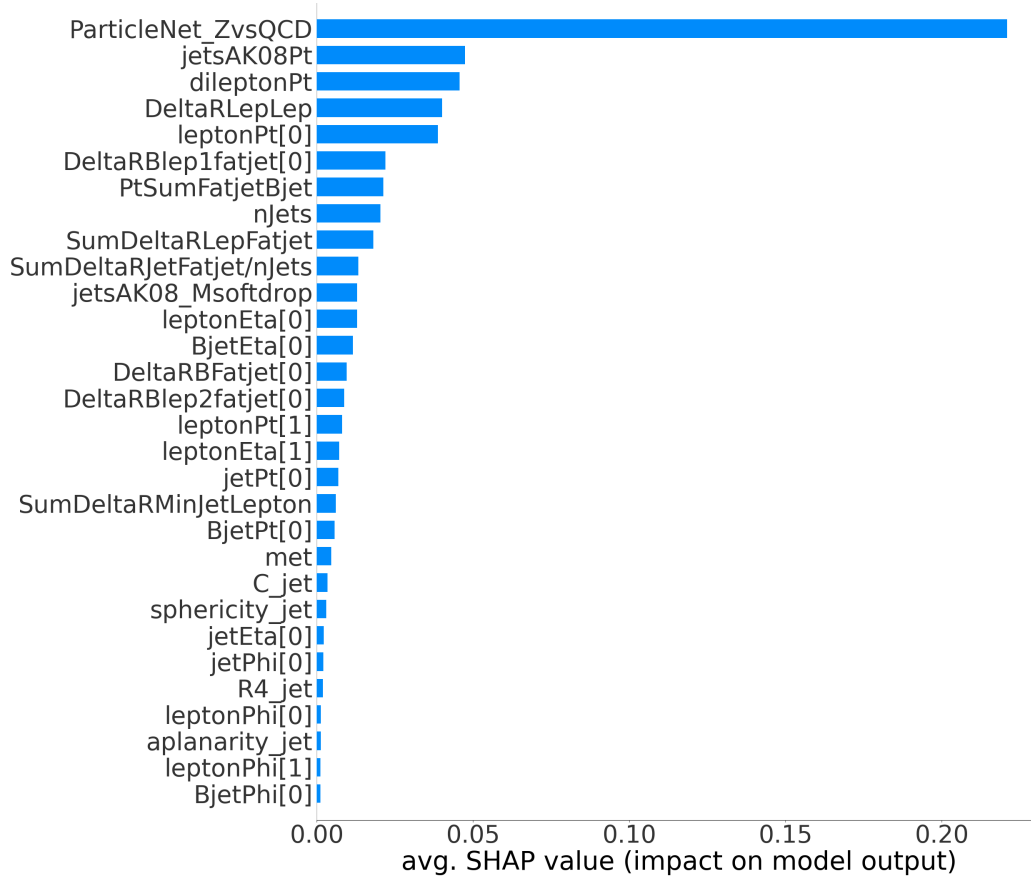


Figure 9.13: Relative feature importance for the 1b model, calculated as SHAP values.

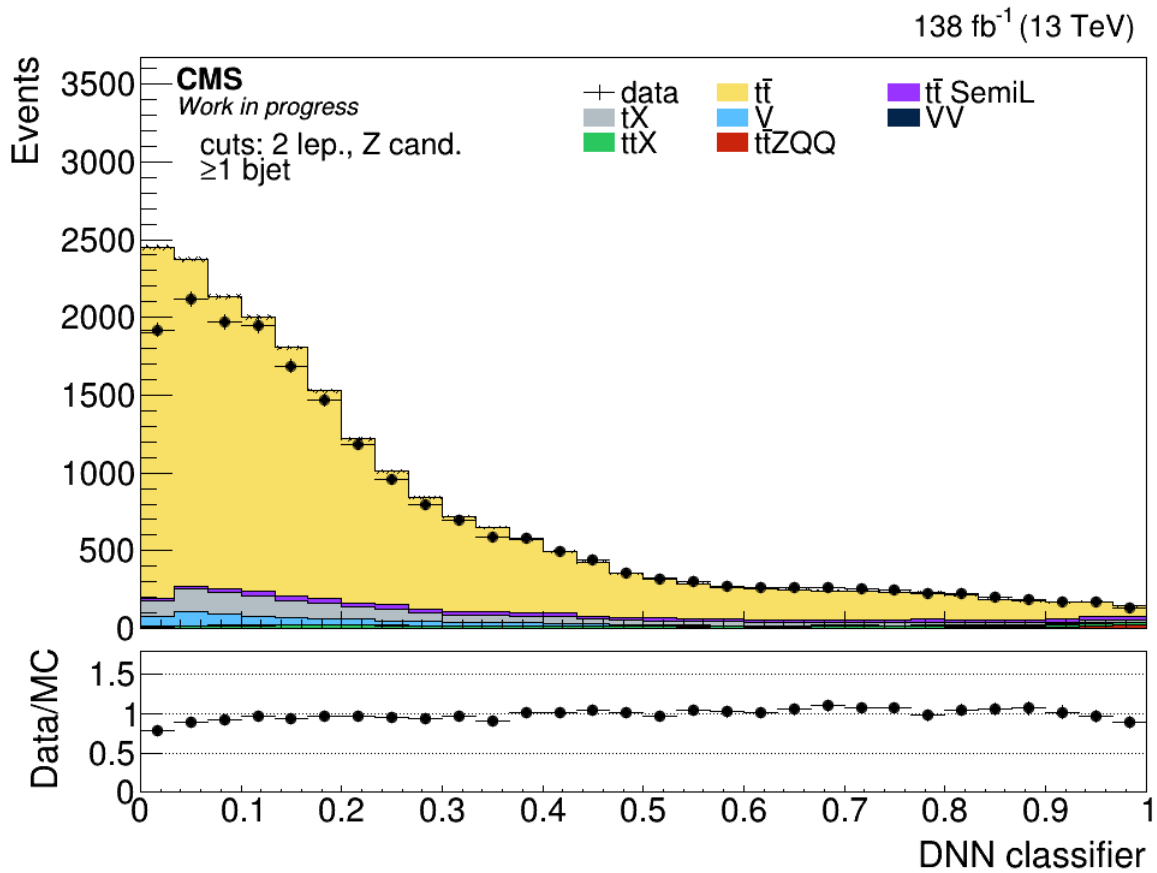


Figure 9.14: Final combined output of the DNN classifiers, applied to all data and simulation samples, for the four data-taking eras. The figure shows the combination of both categories, with exactly one b jet and with two or more b jets.

backgrounds, like Drell-Yan, mostly receive low output values, leading to good separation from the signal. This makes this final classifier a good choice for use as a discriminating variable.

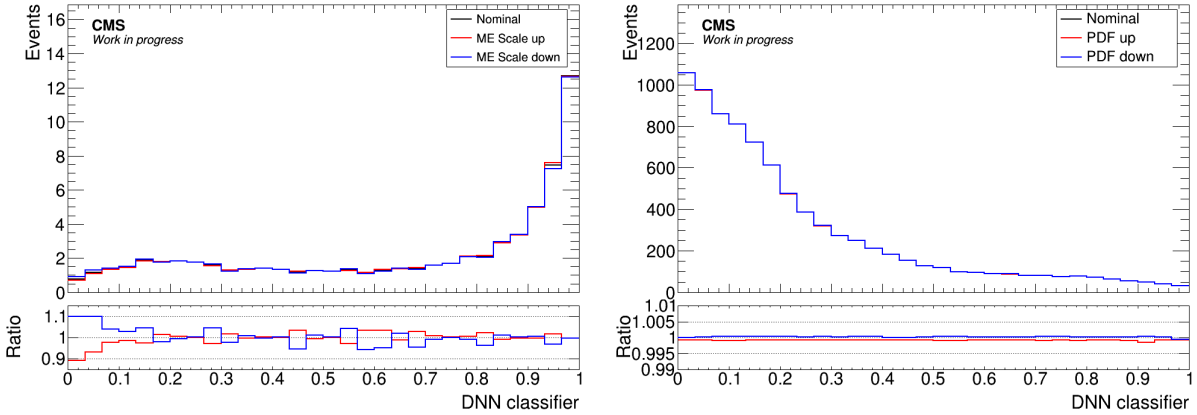
To perform the fit of the standard model simulation to the data to extract the cross section of the $t\bar{t}Z$ process, many systematic uncertainties need to be considered. These uncertainties include theoretical uncertainties, originating from the standard model calculations or the accuracy of the cross section measurements, and various sources of experimental uncertainties. In this section, the various sources of systematic uncertainty are described and quantitative estimates of their size, prior to the fit, are provided.

10.1 Theoretical Uncertainties

Cross section uncertainties for the background

Cross section uncertainties are applied to the total number of events per simulated process. The assumed uncertainties for each process group are chosen as following:

- the $t\bar{t}$ cross section has been measured precisely, with an accuracy of about 5%. It has, however, not been measured in a signal region with the high hadronic energy requirement, as for example necessary to form an additional boosted jet. Therefore, the uncertainty for the $t\bar{t}$ process is assumed to be 10% in this analysis.
- the $t\bar{t}+X$ category includes $t\bar{t}W$, $t\bar{t}\gamma$, $t\bar{t}H$ and $t\bar{t}Z$ with leptonic Z boson decays. As stated in section 8, the $t\bar{t}H$ cross section is only measured with an accuracy of about 30%. However, $t\bar{t}H$ only contributes a relatively small fraction of $t\bar{t}X$ in high bins of the DNN classifier. In that region, $t\bar{t}W$ is the dominant contribution. This cross section is measured with an accuracy of about 15% [42, 43]. This value is therefore used as uncertainty of the process group.
- Other backgrounds: For all other processes (Drell-Yan, single top and diboson) an uncertainty of 10% is assumed.



(a) DNN classifier shapes for simulated signal (b) DNN classifier shapes for simulated $t\bar{t}$ back-events. Varied shapes for the matrix element ground events. Varied shapes for the PDF uncertainty are shown in red and blue. uncertainty are shown in red and blue.

Figure 10.1: Example shapes for theoretical uncertainties. Up variations are shown in red, down variations are shown in blue. The nominal shapes are shown in black. All figures show simulation for the year 2018.

Matrix element scales

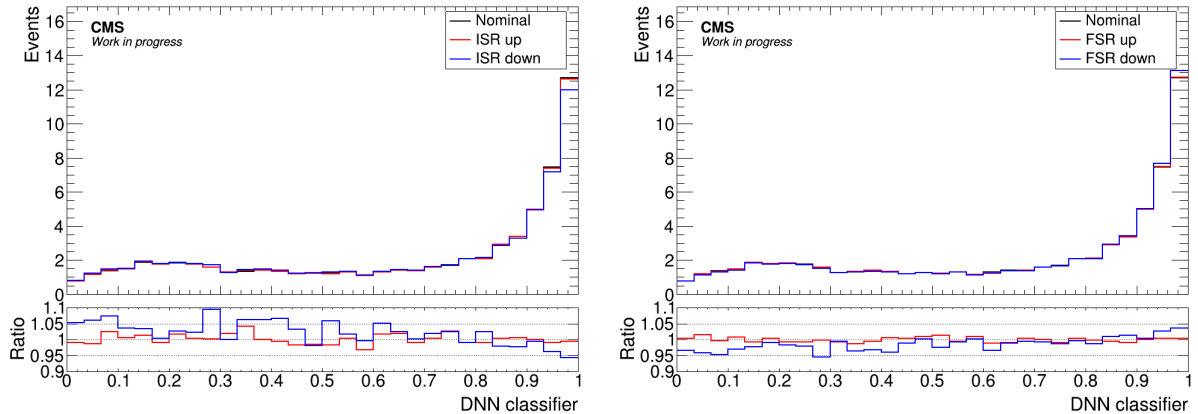
In order to calculate the simulation, renormalisation and factorisation scales need to be chosen ad hoc. As the calculations are done at a finite order in perturbation theory, these choices have an effect on the result. In order to estimate the uncertainty on the simulation created by these choices, the scales are varied by a factor of 0.5 for the downward variation and by a factor of 2 for the upward variation. The varied output distributions are normalised to the nominal cross section, as the quantitative uncertainty from theory is covered by the cross section uncertainty. The normalised distributions are then used as shape based uncertainty histograms.

Renormalisation and factorisation scales are varied in combination. The combined variation is defined as both scales varied in the same direction.

This uncertainty is considered separately for the signal and for the $t\bar{t}$ background. The distributions of the up and down variations compared to the nominal histogram for 2018 for the signal process can be seen in figure 10.1(a).

Parton shower uncertainty

When simulating parton showers, a certain value is assumed for α_s based on the energy scale. This value has a corresponding uncertainty, which is applied by varying the renormalisation scale for QCD emissions in initial-state and final-state radiation (ISR and



(a) DNN classifier shapes for simulated signal events. Varied shapes for the ISR uncertainty are shown in red and blue. (b) DNN classifier shapes for simulated signal events. Varied shapes for the FSR uncertainty are shown in red and blue.

Figure 10.2: Example shapes for uncertainties from parton shower uncertainties. Up variations are shown in red, down variations are shown in blue. The nominal shapes are shown in black. Both figures show simulation for the year 2018.

FSR) [147]. ISR and FSR are applied as two separate uncertainties. Like for the factorisation and renormalisation uncertainties, they are normalised and applied only as shape uncertainties.

ISR and FSR uncertainties are applied to both signal and $t\bar{t}X$ background processes. They are considered fully correlated across the years and processes. Distributions of the DNN classifier varied with respect to the ISR and FSR uncertainties, compared to the nominal signal shapes, can be seen in figure 10.2.

Parton distribution function uncertainty

In order to simulate proton-proton collisions, the parton distribution inside the proton must be accurately known. This distribution is described by the parton distribution functions (PDFs). The PDFs are experimentally determined and are associated with an uncertainty [148]. This uncertainty is applied via weighting each event, resulting in a shape uncertainty. The PDF uncertainty is only applied to the $t\bar{t}$ background. As the same function is used for each era, it is considered fully correlated between the eras. The distributions of the DNN classifier, varied with respect to the PDF uncertainty for 2018 can be seen in figure 10.1(b).

Table 10.1: Correlated and uncorrelated values for the uncertainty on the integrated luminosity in percent. Values taken from Ref. [147].

	2016	2017	2018
Uncorrelated 2016	1.0	0.0	0.0
Uncorrelated 2017	0.0	2.0	0.0
Uncorrelated 2018	0.0	0.0	1.5
Correlated 2016-2017-2018	0.6	0.9	2.0

10.2 Experimental Uncertainties

10.2.1 Trigger efficiency

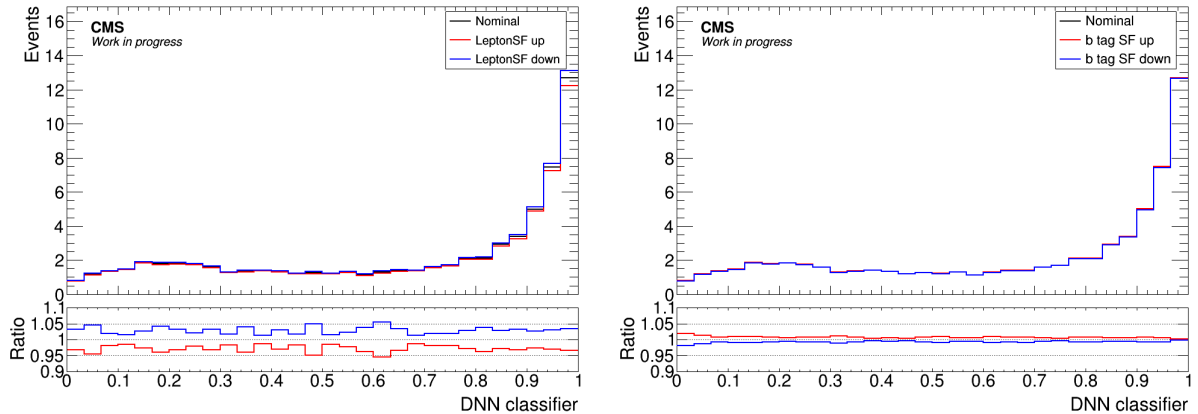
No triggering system is fully efficient. In general, p_T and η dependent inefficiencies can be precisely modelled for each trigger. However, this level of detail is not needed in a statistically limited analysis such as this one. For this analysis, a flat uncertainty of 2% is applied to the number of events. As the trigger settings differ between the years, the trigger efficiency uncertainty is treated as correlated between the two eras of 2016 and uncorrelated between 2016, 2017 and 2018.

10.2.2 Luminosity uncertainty

The measurement of the integrated luminosity is mainly based on the VdM method and the emittance scans, as explained in detail in section 3.2. Corrections and uncertainties of these measurements have been studied in detail in Refs. [76, 114, 115]. Uncertainties on the luminosity measurement originate from various sources. Some of these sources are independent for each year, while others are correlated between the years. The uncertainty on the luminosity is therefore split into an uncorrelated part for each year and a separate correlated part. The values for the different uncertainties on the luminosity can be found in table 10.1.

10.2.3 Scale factor uncertainties

Scale factors for reconstructed objects, correcting differences between data and simulation, as described in sections 4.3.1 and 4.4, come with associated uncertainties. In this analysis, scale factors are applied for b jets and for leptons. They are p_T and η dependent and are applied for every lepton (leptonSF), b jet (btagHF) and non-b jet (btagLF) in the event. For up and down variations, varied scale factors are applied, leading to varied shapes of the DNN classifier, which are then used as shape uncertainties in the fit. Varied shapes for lepton and b tag scale factors for signal for the year 2018 can be seen in figure 10.3.



(a) DNN classifier shapes for simulated signal events. Varied shapes for the lepton scale factor uncertainty are shown in red and blue. (b) DNN classifier shapes for simulated signal events. Varied shapes for the b tag scale factor uncertainty are shown in red and blue.

Figure 10.3: Example shapes for scale factor uncertainties. Up variations are shown in red, down variations are shown in blue. The nominal shapes are shown in black. All figures show signal simulation for the year 2018.

10.2.4 Jet energy corrections

Two different kinds of jet energy corrections (JEC), and systematic variations thereof, are applied: The jet energy scale and the jet energy resolution.

Jet energy scale (JES) corrections take into account for example the detector response to hadrons, pileup or residual differences between data and simulation [89].

Jet energy resolution (JER) corrections describe the uncertainty of the reconstructed jet p_T from detector resolution and quantum effects. It ranges from 5% for high p_T jets to 20% for soft jets.

Unlike the scale factors and their variations, the JEC are not applied to the event weight but directly to the p_T and η of the jets. This can cause b-tagged, non-b-tagged or boosted jets to pass or fail cuts with the varied jet energy scale, and the total amount of events in the signal region can change. Also, variables like the p_T of jets, b jets and boosted jets are inputs to the DNN classifier. Therefore, both the event selection and the DNN classifier evaluation need to be redone to determine varied shapes for the JEC uncertainties.

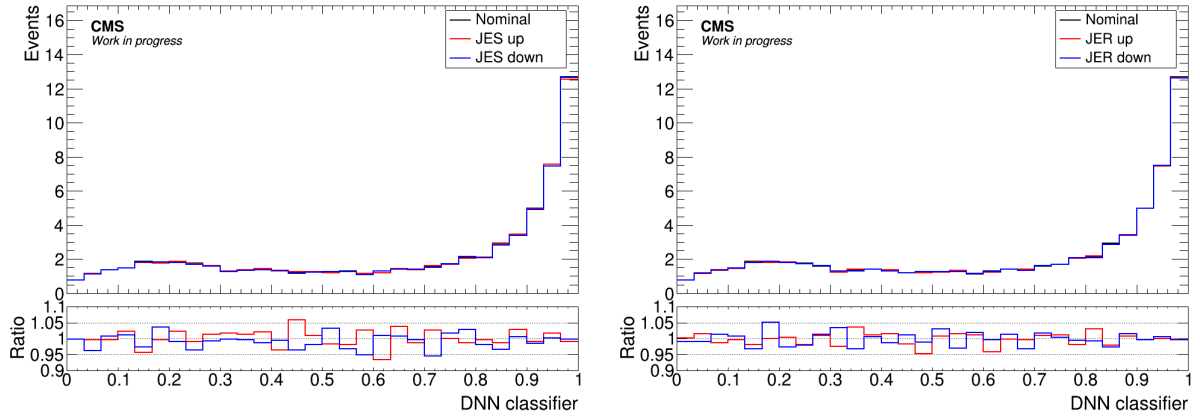
In total, four different uncertainties related to JEC are applied: for jet energy scale and resolution for AK04 jets and separately for jet energy scale and resolution for boosted AK08 jets. Jet energy scale variations are treated as correlated between the years, while the jet energy resolution variations are treated as uncorrelated.

Shapes for the year 2018 of jet energy scale and resolution for AK04 and AK08 jets can be seen in figure 10.4.

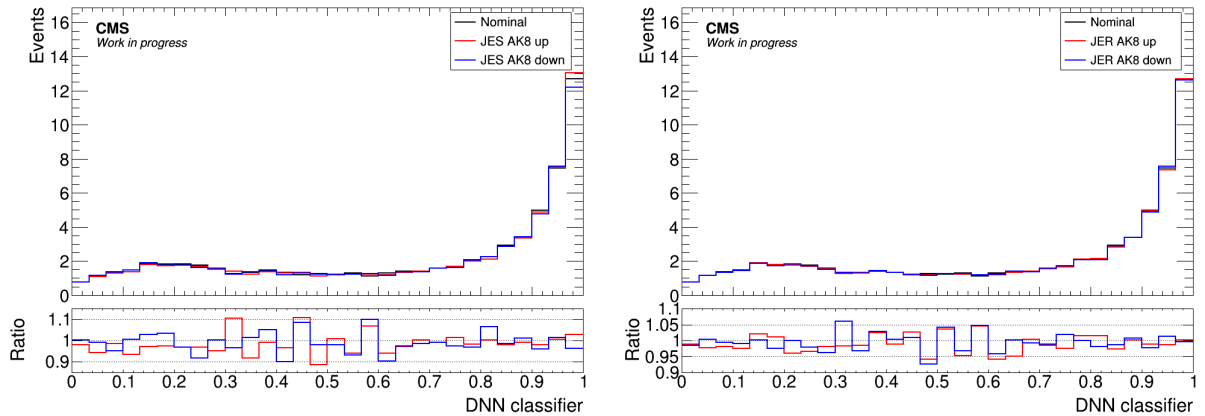
Pileup uncertainty

The distribution of pileup in simulation does not exactly match the distribution seen in data. In order to correct this, every simulated event is weighted to match the pileup distribution in data.

However, the pileup in the data can only be extracted using the total inelastic cross section of proton-proton collisions. This cross section is subject to uncertainty, and therefore, so is the measured pileup distribution. In order to calculate this uncertainty, the total inelastic cross section is shifted by 4.6% in both directions, to create up and down variations.



(a) DNN classifier shapes for simulated signal events. Varied shapes for the jet energy scale uncertainty for AK04 jets are shown in red and blue. (b) DNN classifier shapes for simulated signal events. Varied shapes for the jet energy resolution uncertainty for AK04 jets are shown in red and blue.



(c) DNN classifier shapes for simulated signal events. Varied shapes for the jet energy scale uncertainty for boosted jets are shown in red and blue. (d) DNN classifier shapes for simulated signal events. Varied shapes for the jet energy resolution uncertainty for boosted jets are shown in red and blue.

Figure 10.4: Example shapes for uncertainties from jet energy corrections. Up variations are shown in red, down variations are shown in blue. The nominal shapes are shown in black. All figures show signal simulation for the year 2018.

COMPARISON OF DATA AND SIMULATION

As the measurement of the $t\bar{t}Z$ cross section is done by fitting the observed data to the simulated distributions, it is of profound importance, that the simulation describes the data as accurately as possible. During the analysis process many distributions, separated by different categorisations (by lepton type or by b jets), have been analysed to make sure that the signal region is modelled with sufficient accuracy. In this chapter, the findings of these studies are discussed. Control distributions displaying several input variables of the DNN classifier as well as the classifier itself are shown for the different eras. Due to the large number of figures, only a small selection of the distributions is shown.

In the figures, the simulated samples are shown in a stacked distribution. The signal process is displayed in red, $t\bar{t}X$ processes are shown in green, diboson is shown in dark blue, Drell-Yan is shown in light blue and single top quark processes are shown in grey. Events from $t\bar{t}$ production are separated into the semi-leptonic channel, shown in purple and the dileptonic channel, shown in yellow. The shaded area on the stack distribution denotes the statistical errors of the simulated samples. The data is shown as black dots. Below the stacked distribution, the ratio between data and simulation is shown.

The agreement differs between the eras, and the eras are discussed separately below. The eras 2017 and 2018 are treated together in section 11.1. Section 11.2 discusses the data-to-simulation agreement in the first part of 2016 and section 11.3 shows the latter part. In section 11.4 the agreement for the full Run 2 dataset is shown, also discussing several input distributions of the DNN classifier.

11.1 Data Recorded in 2017 and 2018

The agreement between data and simulation is similar for the eras 2017 and 2018. For both years, there is sufficient data to keep statistical fluctuations of the data points at a low level. Also, the simulated samples are large and the statistical uncertainty from the number of simulated events is low. Very few mismodellings can be observed.

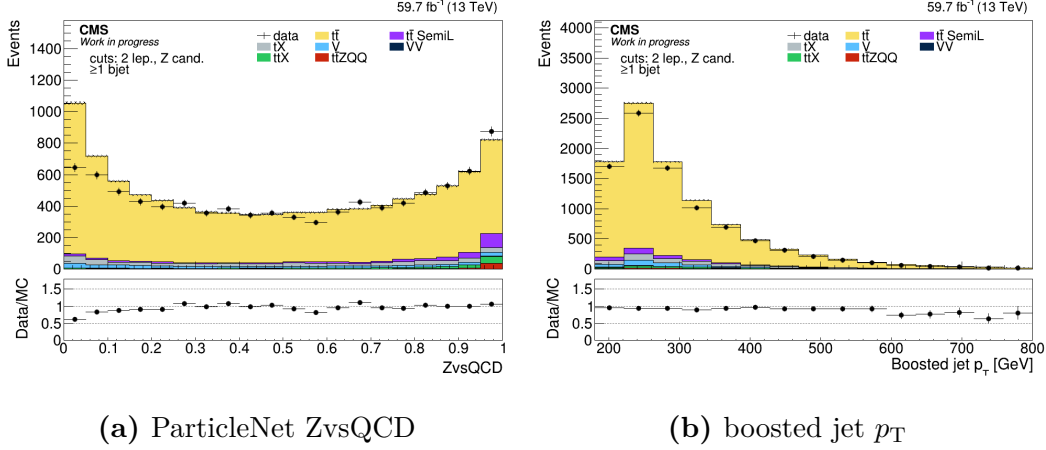


Figure 11.1: Example stack distributions for the era 2018.

As an example for the overall agreement, the distribution for the p_T of the boosted jet can be seen in figure 11.1(b) for the era 2018. It can be seen that the data matches the stack distribution of the simulated samples well and that the ratio between the two is flat. Only for boosted jets with a p_T of above 500 GeV, a slight excess of the simulation can be seen. However, this area only includes very few events, making this mismatch insignificant. A more significant mismodelling can be seen in the ParticleNet discriminator ZvsQCD, shown in 11.1(a) for the era 2018. While the agreement is good for bins above a value of 0.25, below that an excess of simulation above data can be seen. As ZvsQCD is the most relevant input variable of the DNN classifier, this discrepancy propagates through the network and a slight excess of simulation at low values can also be seen in the classifiers, shown in the third line of figure 11.4 for the era 2017 and in the fourth line for the era 2018, however to a much smaller extent. As it only affects the first 3 out of 30 bins of the classifier histogram, where no signal contribution is expected, this discrepancy is considered unproblematic, for the overall agreement. It can, however, cause problems in the multidimensional fit used to perform the calculation of the $t\bar{t}Z$ cross section. Therefore, to perform further calculations, the first three bins of the classifier distribution are disregarded.

11.2 Data Recorded in the First Part of 2016

For the first part of 2016, in general the behaviour of data and simulation is similar to 2017 and 2018, however, with only 19.3 fb^{-1} of data, the statistical fluctuations are much higher. This can be observed comparing the two distributions of 2018 in figure 11.1 with the same distributions for 2016 preVFP in figure 11.2 and also by comparing the

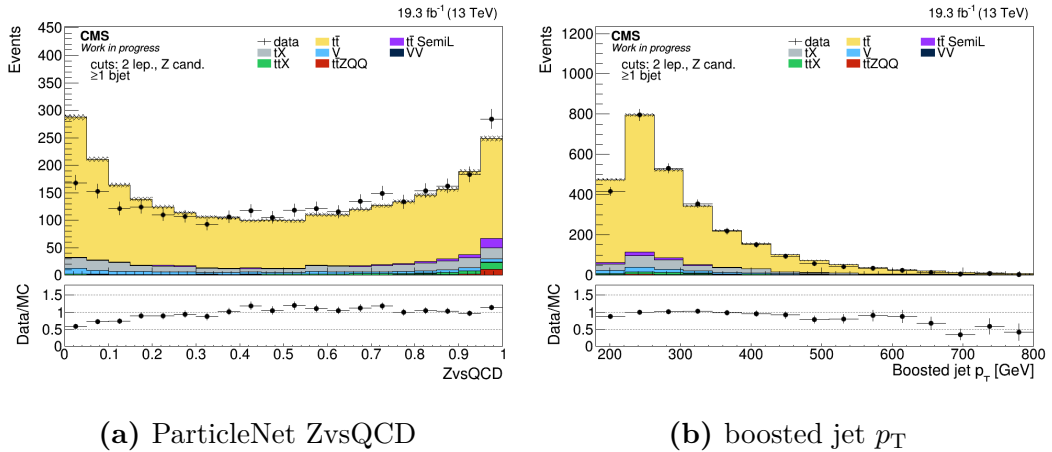


Figure 11.2: Example stack distributions for the era 2016 preVFP.

DNN classifier distributions (first line in figure 11.4 for 2016 preVFP). While the overall agreement looks similarly good, more up and down variations can be seen in the ratio. The mismodelling in the first bins of ZvsQCD and the DNN classifier are also visible and in the same order of magnitude. It can therefore be concluded that no additional measures need to be taken for 2016 preVFP and that, despite the much lower number of events, the same strategies and methods as in the eras with a greater number of events can be used. This includes the exclusion of the first three bins of the classifier distributions, and multidimensional fits with the events split into the two categories.

11.3 Data Recorded in the Second Part of 2016

For the second part of 2016 (2016 postVFP), the data-to-simulation agreement is more problematic. Despite the with 16.6 fb^{-1} , similar amount of data compared to 2016 preVFP, the fluctuations are stronger compared to 2016 preVFP, as it can be seen in the distributions for ParticleNet ZvsQCD and the p_T of the boosted jet for this era, shown in figure 11.3. Especially the region with two or more b jets shows significant mismodelling, as it can be seen in the distribution for the DNN classifiers in the second line of figure 11.4. While the stack distribution for events with one b jet still describes the data more or less, the agreement for events with two or more b jets is far off in many bins. Statistical and systematic uncertainties cannot cover the disagreement. The simulated distribution does not describe the data and therefore cannot be used in the multidimensional fit.

In order to mitigate this, the separation between the 1b and 2b categories is dropped for 2016 postVFP. As the 2b category only includes about 20% of the total events in the signal region, the combined DNN classifier is mainly dominated by the 1b events. The distribution of the combined DNN classifier, shown in figure 11.3(c), describes the data

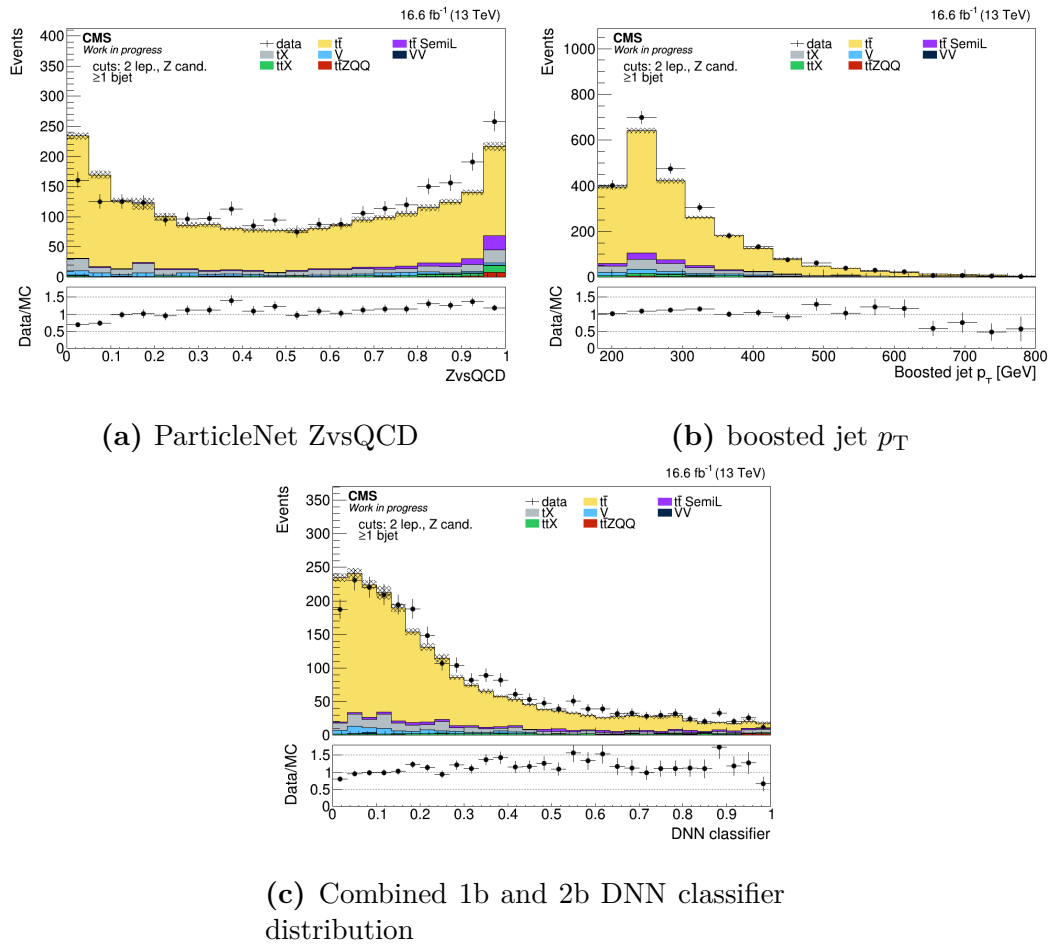


Figure 11.3: Example stack distributions for the era 2016 postVFP.

well enough to be used to calculate the $t\bar{t}Z$ cross section. As for the other eras, the first three bins are excluded, due to the mismodelling in that region, that is also present here, as it is in the other eras.

11.4 The Full Run 2 Dataset

In this section, the data-to-simulation agreement for the full Run 2 dataset with 138 fb^{-1} is shown. While these distributions are not used anywhere in the analysis process, they are a good measure to judge the overall data-to-simulation agreement, as independently as possible from statistical fluctuations. The eight distributions that are shown in figure 11.5 include the most important input variables for the DNN classifier, as well as the distribution of the number of b jets. While this distribution is not important as an input, it is of profound importance as it is the source of the categorisation of events.

All eight stack distributions (namely Z_{vsQCD} , the number of jets and b jets, the p_{T} and Softdrop mass of the boosted jet, the ΔR between the two leptons, as well as the p_{T} and mass of the dilepton system) show good agreement with the corresponding data. Other than the already mentioned discrepancy in the first bins of ParticleNet Z_{vsQCD} other discrepancies can only be seen in regions with very few events present, such as for a p_{T} of the boosted jet above 500 GeV or a Softdrop mass of above 180 GeV. The discrepancies observed in 2016 only play a minor role, as only about 12% of the data originate from the problematic 2016 postVFP. In total, a slight excess of simulation over data can be seen. This excess is flat for most distributions, but is concentrated in the first bins of Z_{vsQCD} and from there carried over to the DNN classifier. Due to the magnitude of the effect, it is most likely that the source is a mismodelling in the dileptonic $t\bar{t}$ events. This observation is considered when estimating the cross section uncertainty for that process (see previous chapter).

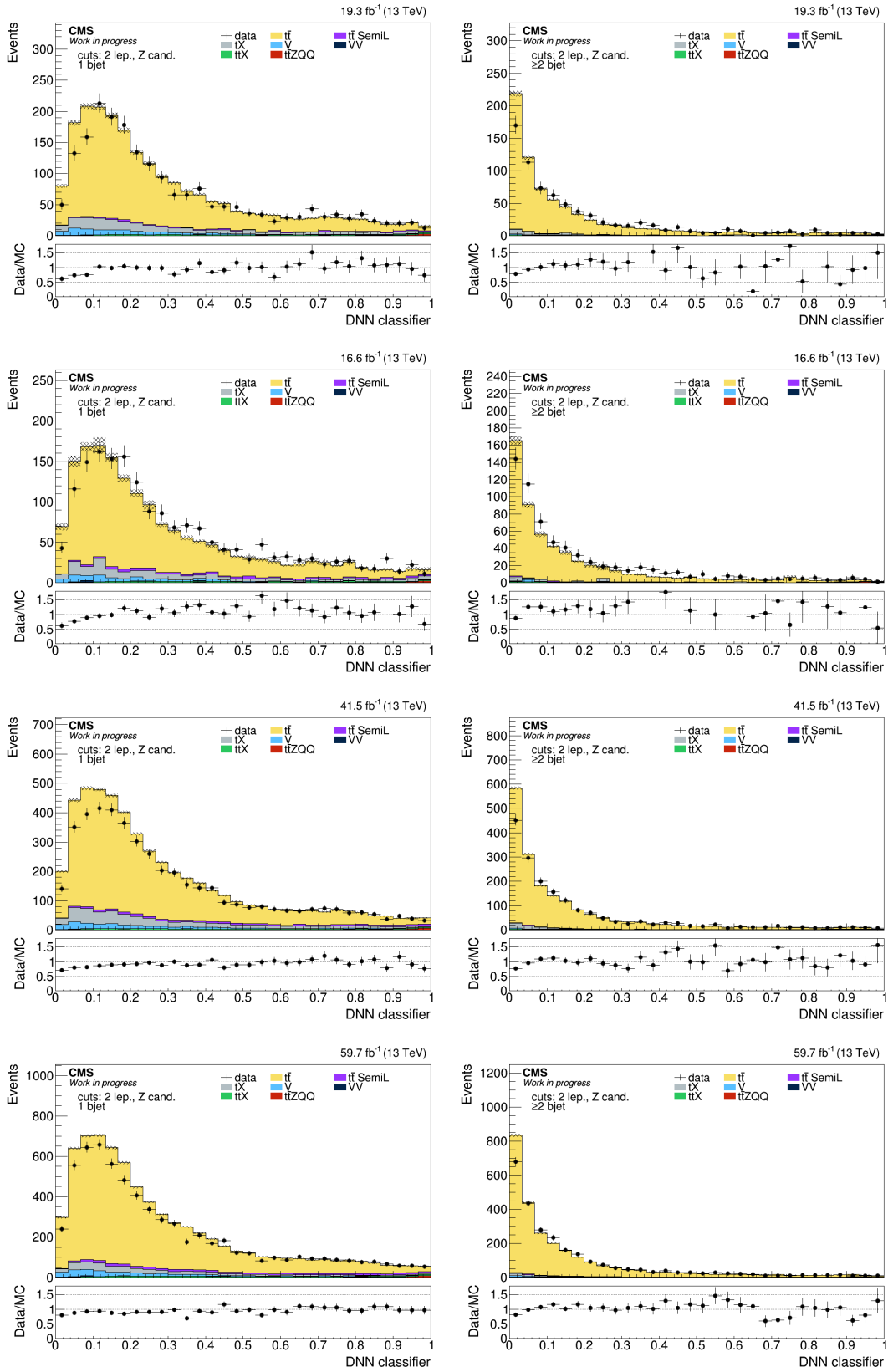


Figure 11.4: Stack distributions of the DNN classifiers. The 1b classifier is shown on the left, the 2b classifier is shown on the right. First row: 2016 preVFP, second row: 2016 postVFP, third row: 2017, last row: 2018.

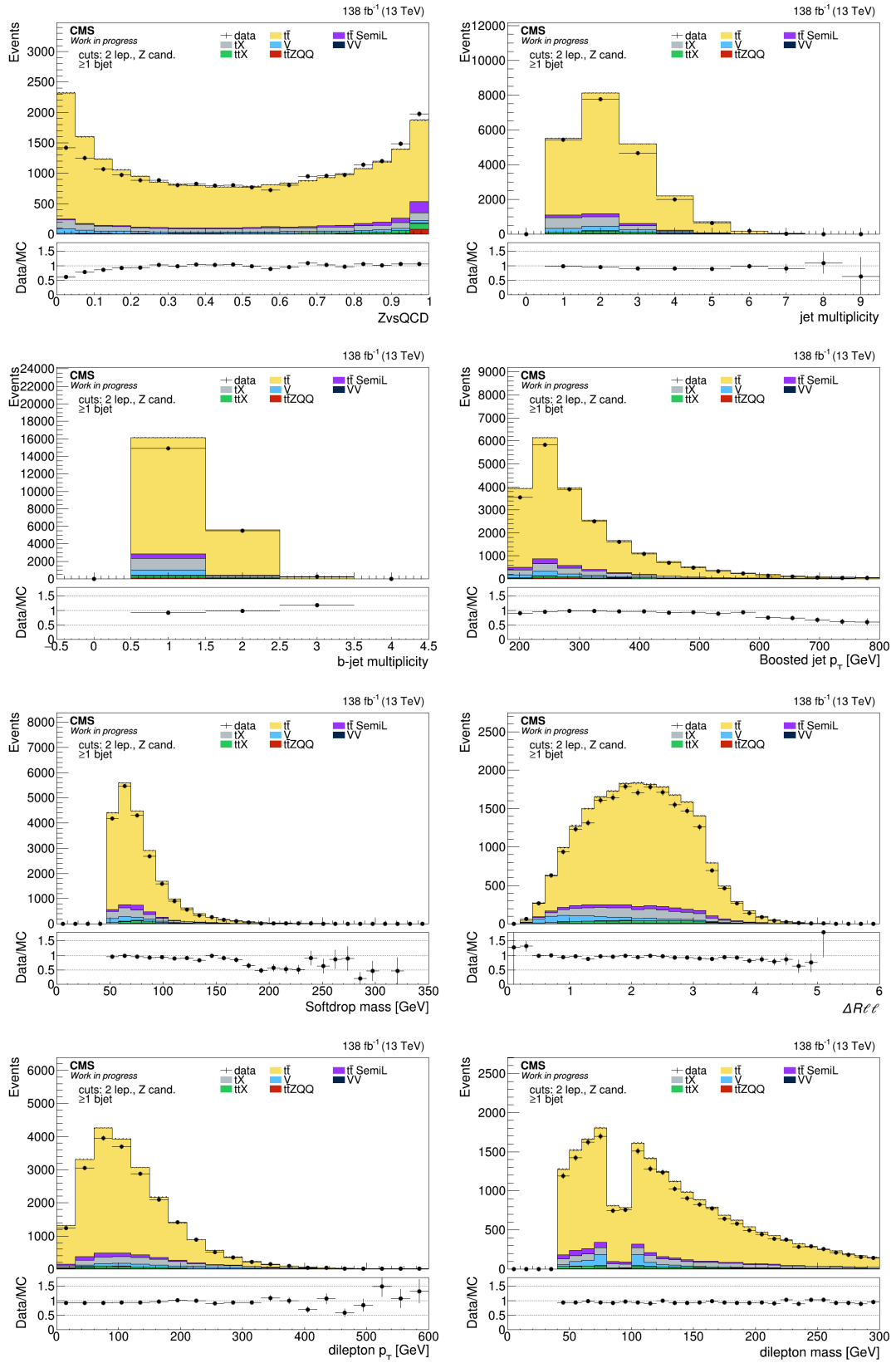


Figure 11.5: Stack distributions of input distributions of the DNN classifier. From top left to bottom right: $Z_{vs}QCD$, the number of jets and b jets, the p_T and Softdrop mass of the boosted jet, the ΔR between the two leptons and the p_T and mass of the dilepton system.

OPTIMISATION STUDIES USING SIMULATED EVENTS

In order to achieve the highest possible sensitivity in the analysis, the different analysis steps are optimised. In this section several optimisation steps are shown, comparing the expected upper limit on the cross section, calculated with simulated events only. These exclusion limits show the maximum allowed cross section at which the background only hypothesis is valid at 95% confidence level. If the signal is present, a limit of one time the standard model would signify an expected significance of two σ .

One possible source for optimisation is the choice of the cuts for the definition of the signal region. The cuts on the leptons and the b jet are designed to select $t\bar{t}$ pairs, and thus do not make a difference for the ratio of signal and background, as both the $t\bar{t}Z$ signal and the main background contain a $t\bar{t}$ pair. A possible optimisation of the cuts can be found in the definition of the boosted jet, namely the minimum mass and p_T cuts to select the boosted jet. Three different working points for each of the two cuts have been explored.

12.1 Choice of the Minimum Transverse Momentum

The three working points for the cut on the minimum p_T of the boosted jet are 200 GeV, 220 GeV and 250 GeV. The cut at 200 GeV is the minimum possible p_T cut, as boosted jets only occur at a vector boson p_T of above 180 GeV, and threshold effects are to be avoided. This cut therefore has the highest possible signal contribution. However, since boosted jets from overlapping QCD jets are expected to have a lower p_T than signal boosted jets, it may well be the case, that the signal to background ratio is better using a higher cut value.

The distribution of the p_T of the boosted jet, starting at 200 GeV, can be seen in figure 12.1. The cut at 250 GeV is indicated by a black vertical line. It can be seen that, while indeed mostly background is cut off at a higher cut value, also a significant part of the signal is lost. In figure 12.2 two expected distributions of the DNN classifier with cuts applied at 200 and 250 GeV can be seen. The lower number of events at higher cut values

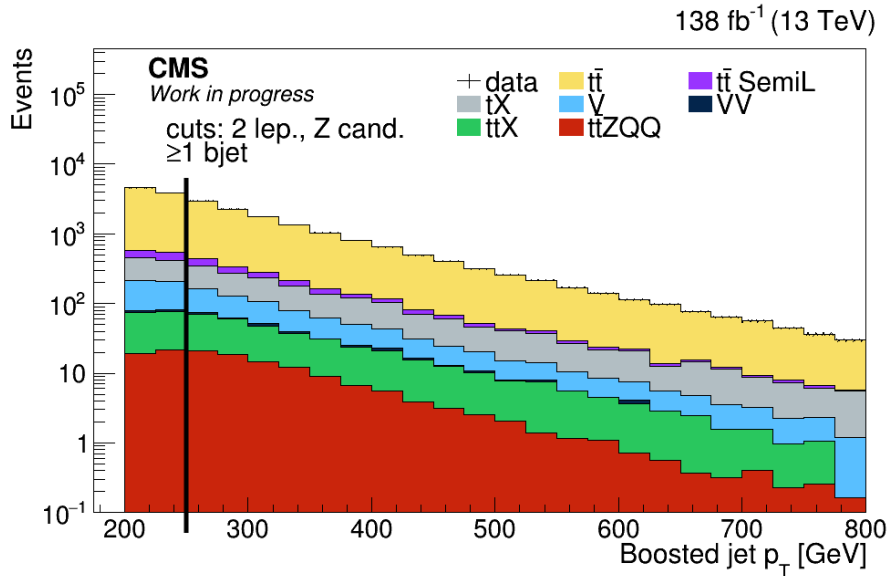


Figure 12.1: p_T of the boosted jet on a logarithmic scale. Only simulation is shown. The distribution starts at a minimum p_T of 200 GeV. The vertical black line indicates a higher possible cut-off value at 250 GeV.

affects mostly the normalisation of the distribution, while barely any effect on the shape or the purity in the highest bin can be seen.

The expected limits calculated for each of the three distributions can be seen in figure 12.3. The achieved limits are similar, with a slight degradation towards the higher cut values. The cut on the p_T of the boosted jet is therefore chosen to be made at 200 GeV.

12.2 Minimum Mass of the Boosted Jet

Another criterion for the definition of the boosted jet is the minimum mass of the jet. Unlike the p_T of the boosted jet, the signal is centred around the Z mass window and raising the threshold leads to a loss of only a few signal events, while the backgrounds get reduced by a far larger margin. However, the mass of the boosted jet, calculated by the Softdrop algorithm, is an important input feature in the DNN and events with a boosted jet with a low mass are centred at a low output value. This effect outweighs the reduction of background, as can be seen in the expected limits, shown in figure 12.4. Limits were calculated with a minimum Softdrop mass of the boosted jet set to 40, 50 and 60 GeV. Even though the total number of expected events is vastly different (about 30k for 40 GeV and about 19k for 60 GeV), barely any change in the expected limit can be seen. The minimum Softdrop mass of the boosted jet is chosen to be 50 GeV.

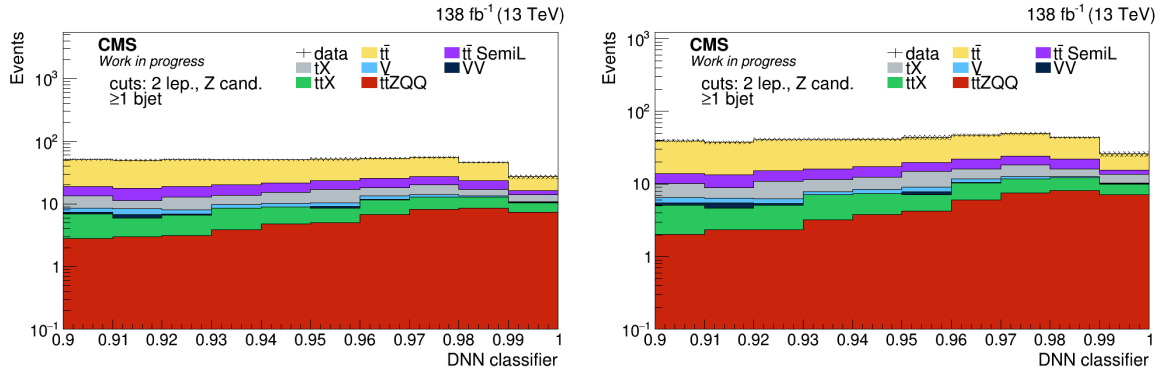


Figure 12.2: Logarithmic distributions of the highest values of the DNN classifier between 0.9 and 1. Different minimal p_T cuts of the boosted jet are applied: 200 GeV (left), and 250 GeV (right).

12.3 Categorisation

Another option, other than the ideal choice of the signal region, is categorisation. Splitting the events in the signal region into a low purity and a high purity category can make use of a better signal-to-background ratio in the latter while not losing any statistical significance. However, too few events in one of the categories can lead to problems with the maximum likelihood fit that determines the measurement, and reduce the overall limit or significance.

The categorisation chosen for this analysis is the categorisation by the number of b jets. All events with one b jet are part of the low purity category, the events with two or more b jets form the high purity category. This categorisation was already chosen to train the DNN, as explained in section 9. In order to test if this categorisation is also profitable for the limit setting, the fit is run both with and without the split into categories applied. The categorisation in the DNN training however, is applied for both fits, as this was done solely to improve the agreement between data and simulation, and has no influence on the fit, as the outputs from both DNN classifiers are filled into the same histogram. For the categorised approach, the categorisation is only applied to three of the four eras, as the fit for the 2b region of 2016 postVFP did not lead to a valid fit result, due to a lack of agreement between data and simulation. This is also shown in section 11.3.

The results of these calculations can be seen in figure 12.5. As expected, the categorised fit results in a clearly better result, with the expected limit improved by close to 20% and a lower uncertainty of the limit.

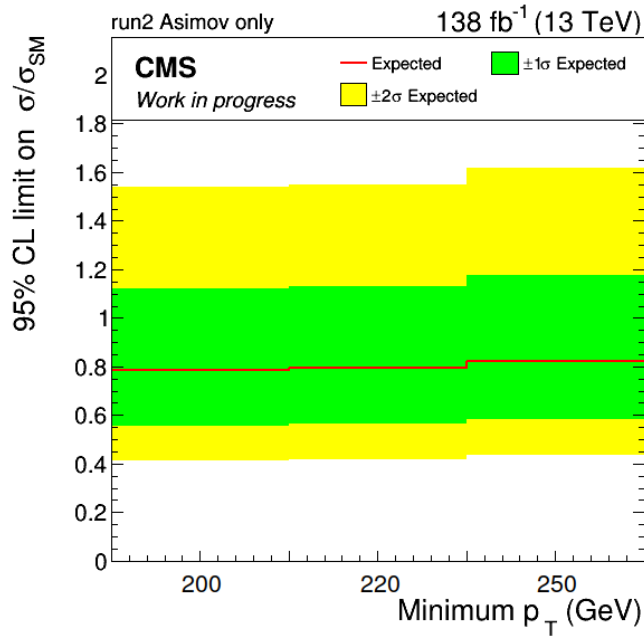


Figure 12.3: Expected limits with different minimal p_T cuts for the boosted jet. Although only slightly, the expected limit deteriorates with tighter cuts applied.

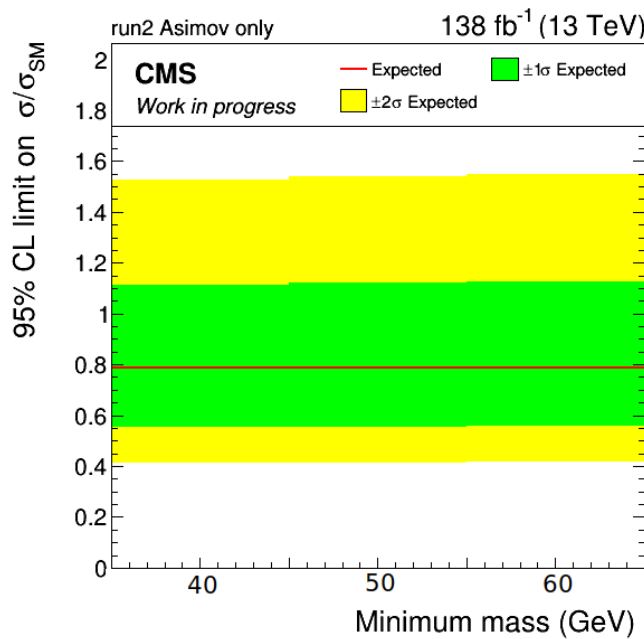


Figure 12.4: Expected limits with different minimum Softdrop mass for the boosted jet. The expected limits change only insignificantly with the different selections.

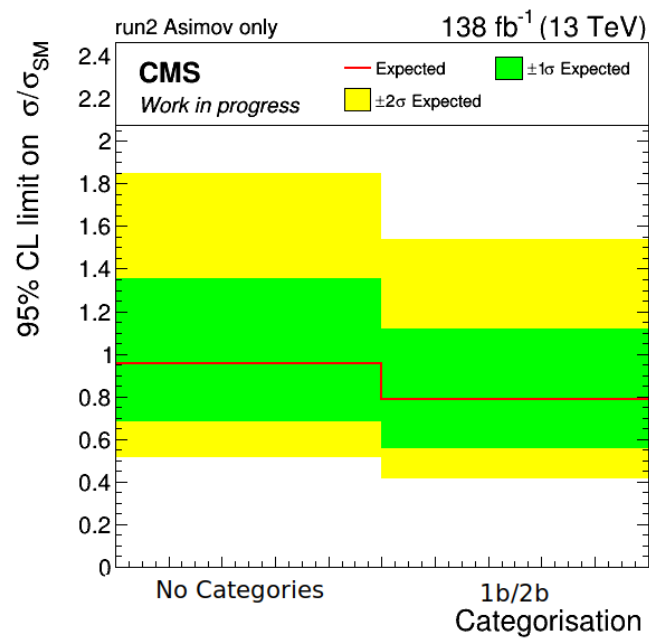


Figure 12.5: Expected limits without (left) and with categorisation into events with 1 b jet and with 2 or more b jets. The categorisation improves the expected limit and also reduces the uncertainty.

In this chapter, the results of the measurement of the $t\bar{t}Z$ production cross section are presented. Apart from the measurements themselves, the fit results are presented by comparing prefit and postfit distributions. The impacts of the different uncertainties discussed in section 10 are discussed in section 13.2.

13.1 Maximum Likelihood Fit

To measure the cross section, binned maximum likelihood fits are performed for each of the input distributions of the DNN classifier (shown in chapter 9). The input distributions have 27 bins each and are divided into one distribution with events with one b jet and one distribution with events with two or more b jets. This split is done for the data-taking eras 2016 preVFP, 2017 and 2018. Due to a non-ideal agreement between data and simulation (shown in chapter 11) for 2016 postVFP a combined distribution is used for that era.

In the fit, the signal strength parameter r , as well as all nuisance parameters (chapter 10) describing the systematic variations are optimised to maximise the likelihood of the simulated samples (summarised in chapter 8) to describe the data. The measured cross section is extracted via the best fit value of r . In figure 13.1 the prefit and postfit distributions for the year 2018 are shown. One can see that the postfit distributions match the data well. While the $t\bar{t}$ cross section is scaled down to mitigate a slight excess of the simulation at lower values of the DNN classifier, the cross section of the $t\bar{t}X$ processes is scaled up to match the loss at higher values. This can be seen in the summary of the impacts of the uncertainties. Both scale adjustments are within their respective uncertainties.

13.2 Impacts of Uncertainties

Figure 13.2 shows a list of the leading systematic uncertainties, ordered by their impact on the final result. The leading uncertainty is the uncertainty on the cross section of

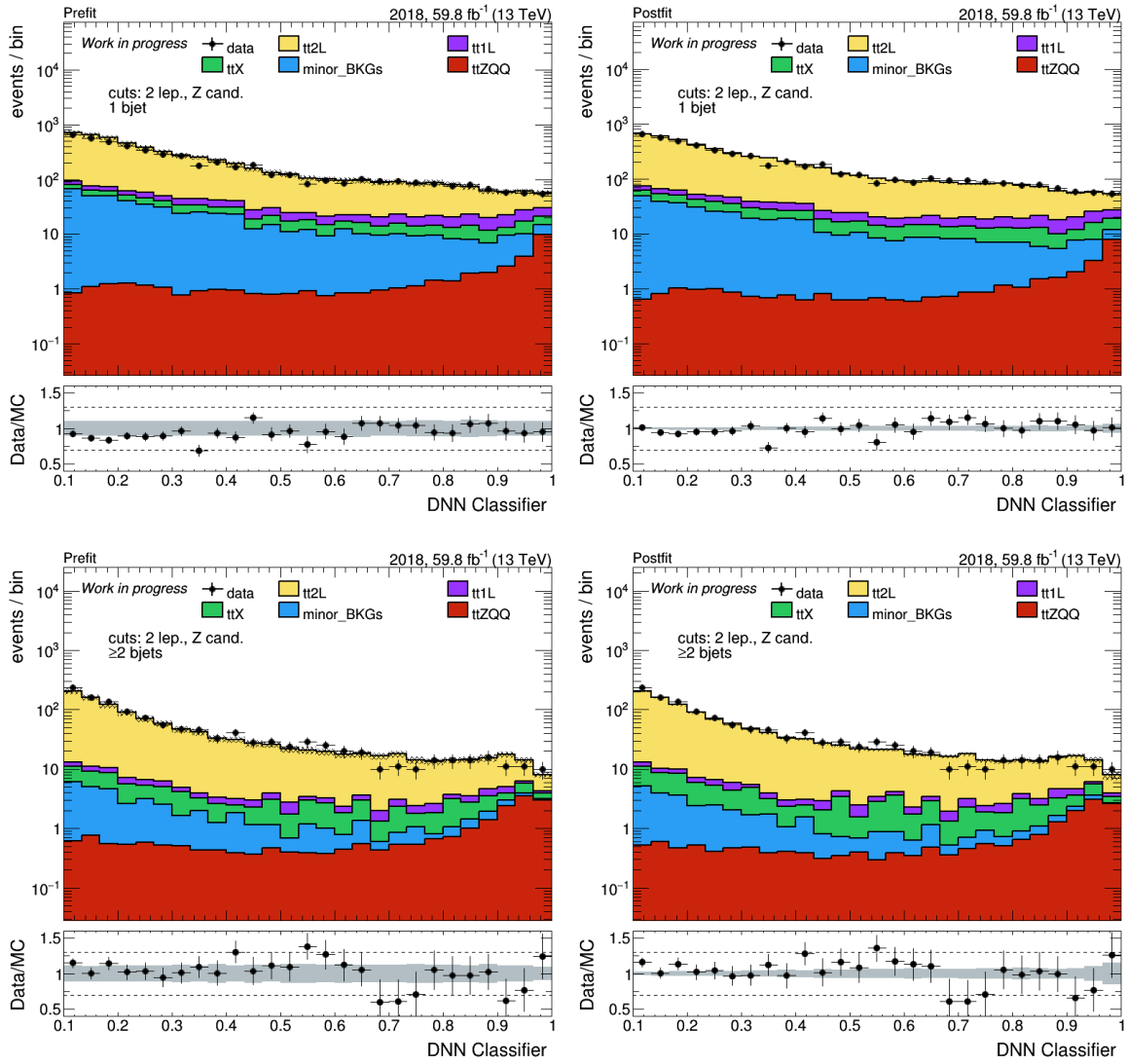


Figure 13.1: Prefit and postfit distributions for the year 2018.

the $t\bar{t}+X$ processes (named "ScalettX" in figure 13.2), with a symmetric impact of about 0.05 on the final uncertainty of the measurement. This can be explained by the large contribution of $t\bar{t}X$ processes in the last, most significant, bin of the DNN classifier. It is followed by the jet energy correction uncertainty for AK8 jets, which has a similar impact on the result, and the uncertainties on the lepton scale factors. The shape-based theoretical uncertainties for initial and final state radiation (ISR and FSR) also are among the leading uncertainties. Both show a one-sided impact. This can be explained by the shape of the uncertainty distributions, shown in chapter 10 (figure 10.2). At low values of the DNN classifier, the down variation for ISR (FSR) is below (above), respectively, and vice versa at high DNN values. Overall, this leads to an upward (downward) effect for ISR (FSR), respectively.

Uncertainties with a smaller but non-negligible impact include uncertainties due to the finite size of the simulated samples (called 'prop_bin...') or the b tagging scale factor uncertainties. Most other uncertainties as the jet energy corrections and resolution for AK4 jets only show smaller impacts. The large impact of the $t\bar{t}X$ cross section uncertainty implies that this measurement is only valid in case the other $t\bar{t}X$ processes also fit the standard model predictions, as a large upward deviation of either $t\bar{t}W$ or $t\bar{t}H$ could also explain the data distribution. This assumption is so far reasonable, as previous measurements of the processes agree with the standard model [41, 42, 128]. However, all measurements still have large uncertainties, and especially in the high boson p_T regime, the statistical power is very low. Therefore, this measurement should be reevaluated with new data and when new measurements of the $t\bar{t}W$ and the $t\bar{t}H$ cross sections are available.

13.3 Cross Section Measurement

The final measurements of the $t\bar{t}Z$ production cross section can be seen in figure 13.4. The figure shows the inclusive cross section calculated from the best fit value of r . The measurements for each of the four eras are shown, as well as the combined final measurement. The statistical uncertainty is shown in orange, the total error, including the systematic uncertainties, are shown in teal. The signal region only represents a small part of the $t\bar{t}Z$ process phase space, thus reflecting a small fraction of the total cross section. Therefore, to be precise, only the cross section in this region is measured. The branching fractions of $t\bar{t}$ to leptons and Z to hadrons are precisely measured quantities and not considered. What is measured therefore is the fiducial cross section for $t\bar{t}Z$ with $p_T(Z) > 200$ GeV. This represents 20.7% of the total cross section (based on the simulated samples). According to the standard model, the inclusive cross section is [149]:

$$\sigma_{t\bar{t}Z_{SM}} = 859^{+8.6\%+2.3\%}_{-9.5\%-2.3\%} \text{ fb.} \quad (13.1)$$

The predicted fiducial cross section of $t\bar{t}Z$ with $p_T(Z) > 200$ GeV therefore is:

$$\sigma_{t\bar{t}Z_{SM, \text{fid.}}} = 178^{+8.6\%+2.3\%}_{-9.5\%-2.3\%} \text{ fb.} \quad (13.2)$$

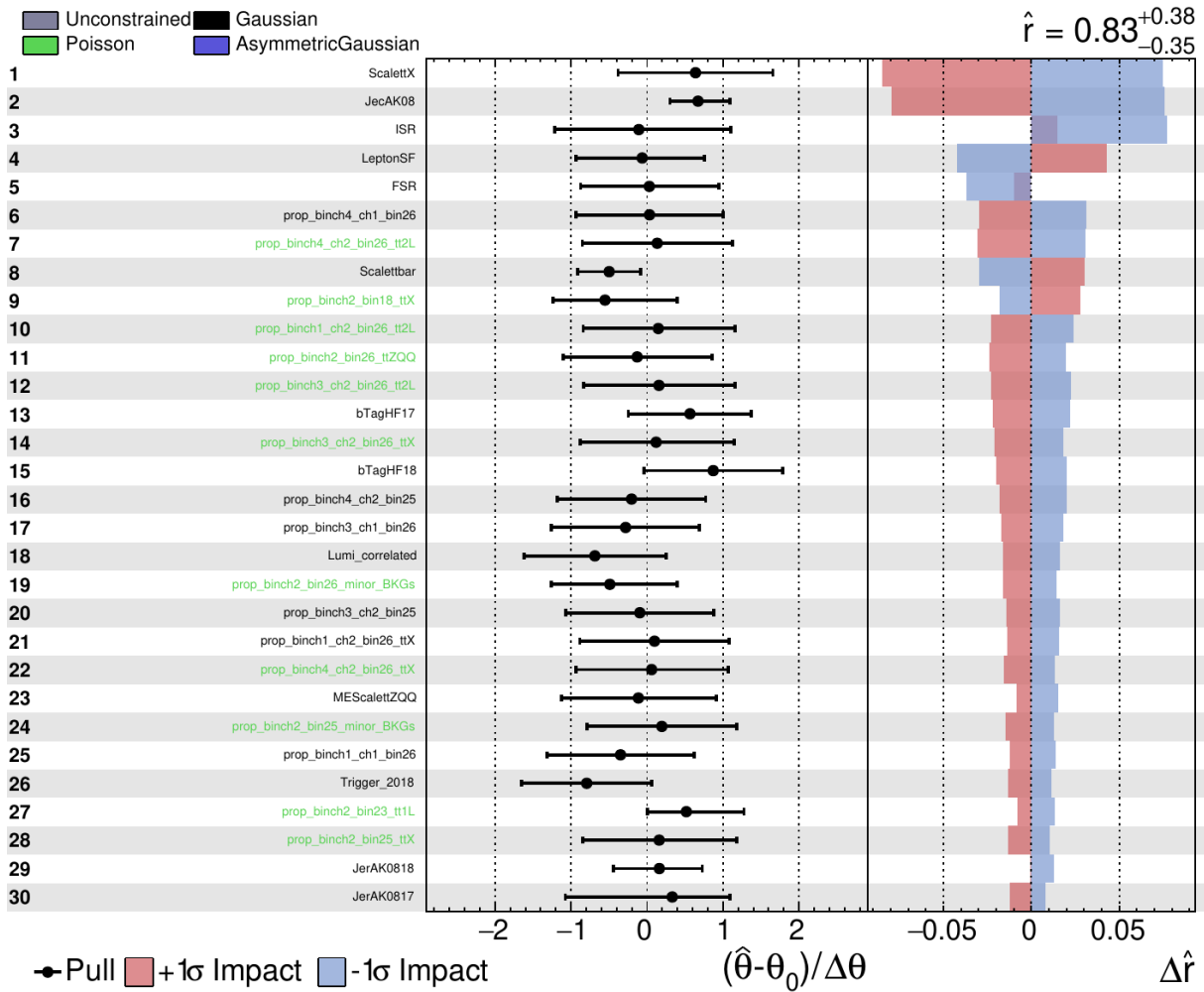


Figure 13.2: The 30 leading uncertainties for the measurement of the $t\bar{t}Z$ cross section, using the full Run 2 data set, ordered by their impact on the final result. The first column shows the name of the uncertainty. Black script indicates Gaussian constrained nuisance parameters, green script indicates Poisson constrained nuisance parameters. The second column shows the pull the fit applies to each nuisance parameter with the respective uncertainty in multiples of the standard deviation. The third column shows the impact on the cross section measurement.

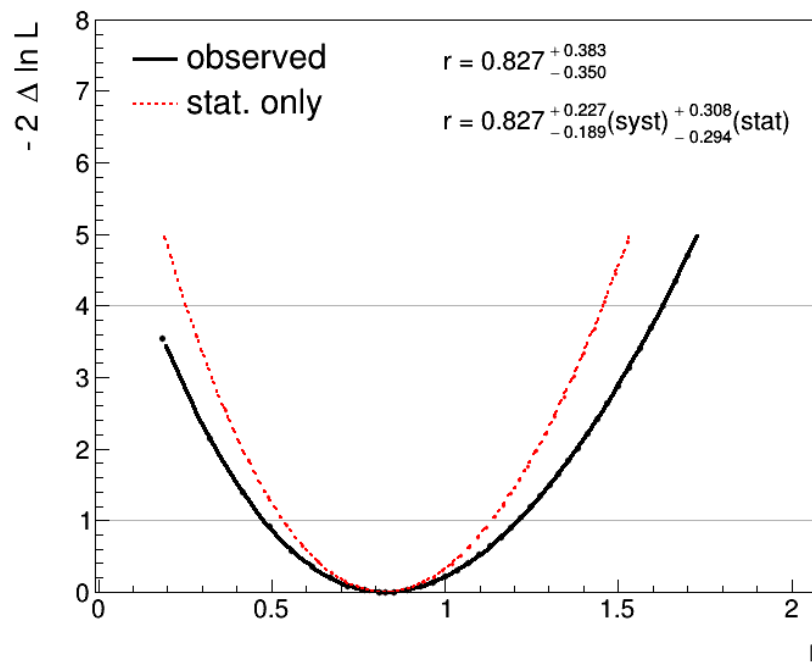


Figure 13.3: Profile likelihood scan of the cross section measurement. The double negative logarithmic likelihood ratio is shown as a function of the signal strength parameter r . The fit with only statistical uncertainties is shown in red, the fit with all nuisance parameters is shown in black.

The measurement of the fiducial cross section with the data from the four eras results in a cross section of:

$$\sigma_{\text{ttZ}_{\text{fid.}}} = 147_{-61.9}^{+67.8} \text{ fb}, \quad (13.3)$$

in agreement with the standard model. Projected to the inclusive cross section this would result in

$$\sigma_{\text{ttZ}_{\text{incl.}}} = 710_{-299}^{+327} \text{ fb}. \quad (13.4)$$

A profile likelihood scan for the measurement can be seen in figure 13.3. The figure shows the double negative logarithmic likelihood ratio ($-2\Delta \ln L$) as a function of the signal strength parameter r . The minimum of the parabola indicates the best fit value. The fit with only statistical uncertainties is shown in red, the fit with all nuisance parameters is shown in black. The final uncertainty bounds of the measurement can be taken from the likelihood parabola. One standard deviation error bounds are reached when the likelihood parabola reaches a value of one, two standard deviation bounds when a value of 4 is reached.

The significance of the measurement is 2.47σ , which excludes the background-only hypothesis at 99.3%. However, the milestone of 3σ , which is enough to be considered evidence, is not reached yet. It will be made possible by adding another analysis channel, for example with semi-leptonic $\text{t}\bar{\text{t}}$ events, and/or when more data is collected at Run 3 of the LHC.

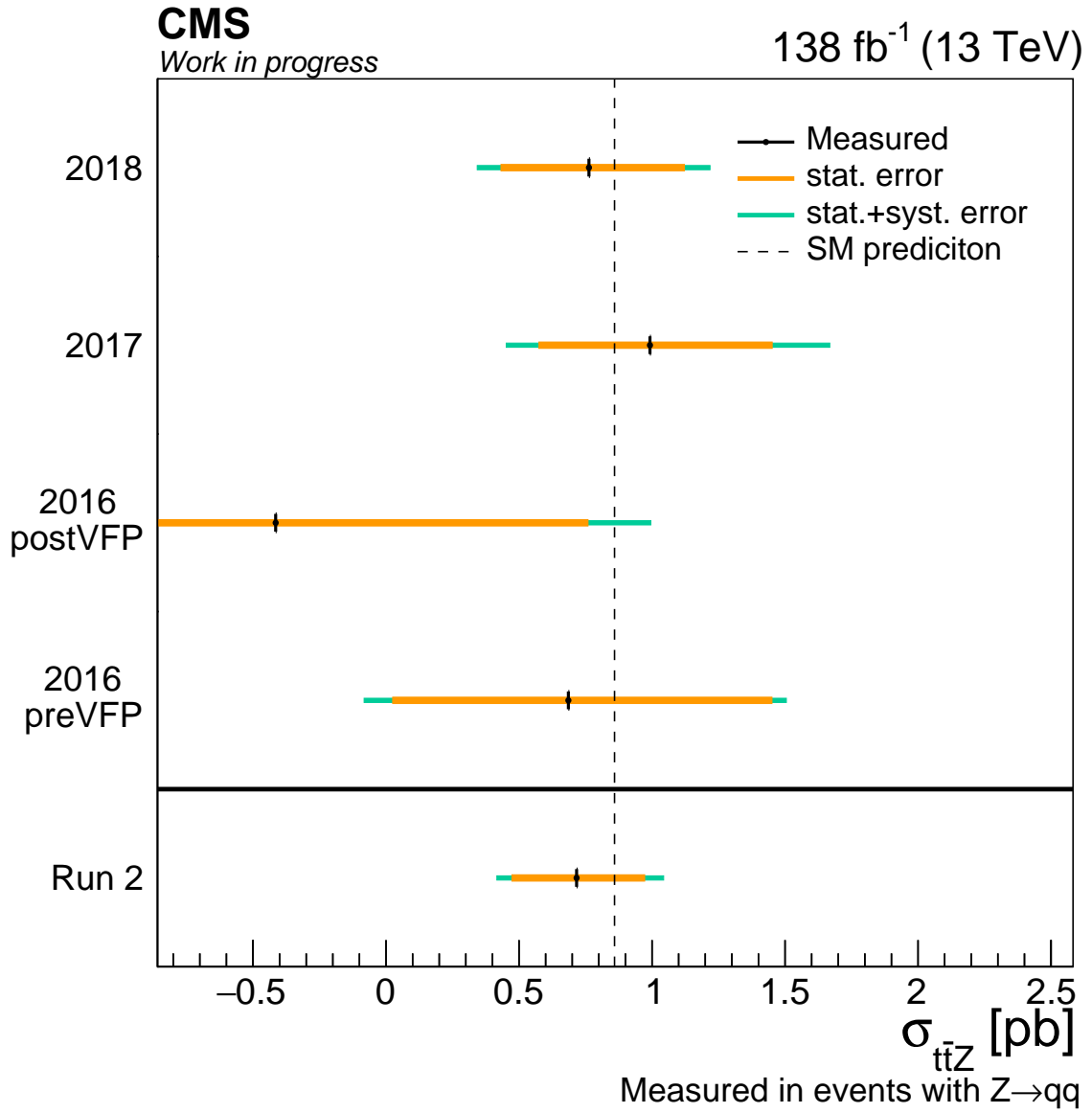


Figure 13.4: Measurements of the production cross section of $t\bar{t}Z$, extrapolated to the inclusive cross section. The error bars denote the 68% confidence intervals. The statistical uncertainties are shown in orange, the total uncertainty is shown in teal. The standard model prediction of the $t\bar{t}Z$ production cross section is shown as a dotted line. All measurements are within the standard model expectation.

Using hadronically decaying Z bosons to measure the $t\bar{t}Z$ process has a lot of promise beyond the analysis shown in this thesis. The precision of the presented result is mostly limited by the amount of data currently available. A logical next step is the inclusion of the semi-leptonic channel, which includes a much higher number of events.

Analyses of this channel have been done in Ref. [150], using resolved Z boson decays, and in Ref. [151] for boosted Z bosons. Both analyses only use $Z \rightarrow b\bar{b}$ decays, which only include about 20% of all hadronic Z boson decays.

Measuring the $t\bar{t}Z$ production cross section in the semi-leptonic channel using all hadronic Z bosons has so far not been attempted. A first study using the same approach as the one presented for the dileptonic channel has shown promise, however, also difficulties.

For this study, the same analysis setup is used as for the dileptonic channel. The signal region is modified to describe semi-leptonic events and a new DNN is trained to separate $t\bar{t}$ from $t\bar{t}Z$. For the signal region only one lepton with at least 30 GeV is required, and the minimum number of AK4 jets is increased to three. The requirements for one b jet and one boosted jet stay the same as in the dileptonic channel. Distributions of a DNN classifier for semi-leptonic events can be seen in figure 14.1. Figure 14.1(a) shows the normalised output distributions for signal and background, and in figure 14.1(b) the full output distribution with simulated events is shown. The separation power does not reach the results of the dileptonic channel. As a result, the number of background events in the last bins of the DNN classifier is very high.

The main reason for the lack of separation power of the classifier and the resulting high limit has been found to be the presence of hadronically decaying W bosons in the hadronic top quark decay. These W bosons are also often boosted, creating vector boson jets, very similar to those from the Z boson. Therefore, simply selecting one boosted jet is an unsuitable approach for the semi-leptonic decay channel. An analysis studying the semi-leptonic channel would need to find a way to take the boosted W bosons into account. This could for example be attempted through flavour tagging of the boosted jet.

Another possibility to further study the dileptonic decay channel is the inclusion of more data. However, data from LHC Run 3 will be taken at a higher centre-of-mass energy

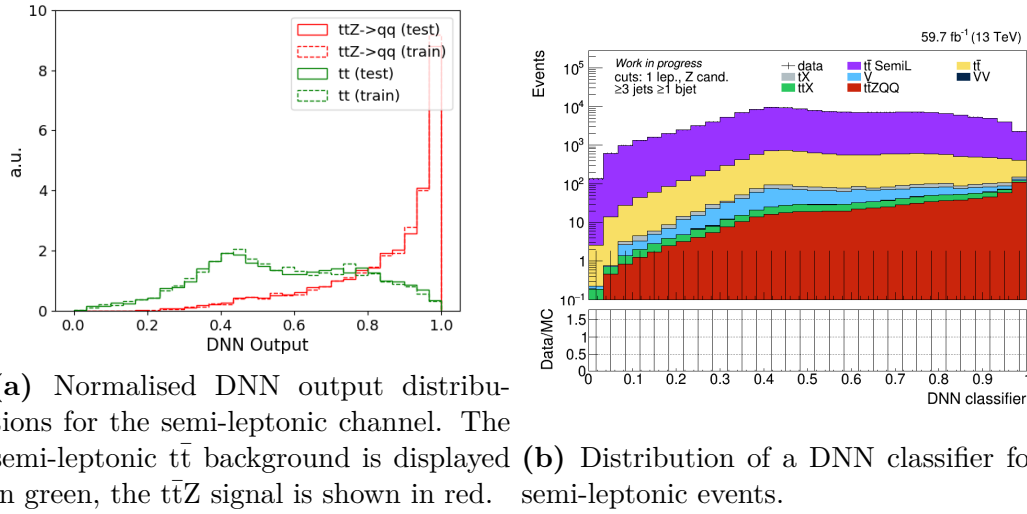


Figure 14.1: DNN output distributions for the semileptonic channel for the year 2018. It has to be noted, that these distributions can only be considered an estimate, as not all necessary scale factors are applied.

of 13.6 TeV. Therefore, a possible new measurement cannot be directly combined with this one. A new measurement providing evidence or even discovery of the process can therefore only be expected when a significantly higher amount of data than the already available 138 fb^{-1} is collected.

In this thesis, two analyses, the calibration of the BCM1F detector and the measurement of the $t\bar{t}Z$ production cross section using hadronically decaying Z bosons, have been presented.

The BCM1F detector is one of the luminosity measurement systems of the CMS experiment at the LHC. In order to calibrate the luminosity measurement, several corrections have been developed and applied: non-linearity effects, making the detector hit rate dependent on the luminosity, filling-scheme dependent corrections to this non-linearity as well as ageing and annealing effects in the detector material and read-out. With all corrections applied, the luminosity measurement is reasonably stable as a function of time, and in 2018, the ratio with respect to nominally the best luminosity measurement ranges between 1 and 1.02.

In the main analysis of the thesis, the measurement of the production cross section of a top quark-antiquark pair in association with a Z boson has been presented. For this measurement, data from the CMS experiment at the LHC has been used. The data was collected during LHC Run 2 and corresponds to an integrated luminosity of 138 fb^{-1} .

The cross section has been measured in the phase space with the $t\bar{t}$ pair decaying dileptonically and the Z boson decaying hadronically. Only Z bosons with a transverse momentum greater than 200 GeV are considered. Due to the strong boost, the two jets of these hadronically decaying Z bosons form a single, boosted jet, which can be used to identify the Z boson.

In order to separate the signal process from the main background, which is top quark-antiquark production, a deep neural network classifier has been developed. The output distribution of the classifier is used to perform a maximum likelihood fit to extract the cross section.

Systematic uncertainties have been considered and are included in the fit as nuisance parameters. Studies on the agreement of data and simulation have been performed on each of the four data-taking eras to ensure the validity of the measurement. To maximise the sensitivity, several studies have been done to ensure a good choice for the cuts defining the signal region. A separation of the signal region into two analysis categories with either

exactly one or two or more b jets was found to improve the sensitivity. The cross section of the $t\bar{t}Z$ process is measured to be

$$\sigma_{t\bar{t}Z_{\text{incl.}}} = 710^{+327}_{-299} \text{ fb.} \quad (15.1)$$

This measurement is in agreement with the standard model prediction. The uncertainty of the measurement is mainly of statistical nature. Improvements can therefore be achieved by analysing additional channels, such as the semi-leptonic channel. A feasibility study using the methodology developed for the dileptonic channel has been discussed.

For the dileptonic channel, the analysis would profit from more precise measurements of the other $t\bar{t}+X$ processes, the uncertainty on these cross sections is the leading systematic uncertainty. Due to the statistical limitation, however, significant improvements can only be expected with a much greater amount of data.

BIBLIOGRAPHY

- [1] P M Watkins. Discovery of the W and Z bosons. *Contemp. Phys.*, 27:291–324, 1986.
- [2] A. Abdesselam et al. Precise determination of the CKM matrix element $|V_{cb}|$ with $\bar{B}^0 \rightarrow D^{*+} \ell^- \bar{\nu}_\ell$ decays with hadronic tagging at Belle. 2 2017.
- [3] The CMS Collaboration. Observation of a New Boson at a Mass of 125 GeV with the CMS Experiment at the LHC. *Phys. Lett. B*, 716:30–61, 2012.
- [4] Bogdan Povh, Klaus Rith, Christoph Scholz, Frank Zetsche, and Werner Rodejohann. *Teilchen und Kerne*. 01 2014.
- [5] H Burkhardt and Jack Steinberger. Tests of the electroweak theory at the Z resonance. *Annu. Rev. Nucl. Part. Sci.*, 41:55–96. 31 p, Mar 1991.
- [6] The Standard Model of Elementary Particles. https://commons.wikimedia.org/wiki/File:Standard_Model_of_Elementary_Particles.svg. Public domain, Accessed Nov. 2021.
- [7] R. P. Feynman and M. Gell-Mann. Theory of the Fermi Interaction. *Phys. Rev.*, 109:193–198, Jan 1958.
- [8] Steven Weinberg. A Model of Leptons. *Phys. Rev. Lett.*, 19:1264–1266, 1967.
- [9] Abdus Salam. Weak and Electromagnetic Interactions. *Conf. Proc.*, C680519:367–377, 1968.
- [10] S. L. Glashow. Partial Symmetries of Weak Interactions. *Nucl. Phys.*, 22:579–588, 1961.
- [11] J. Schwichtenberg. *Physics from Symmetry*. Undergraduate Lecture Notes in Physics. Springer International Publishing, 2018.
- [12] P. Achard et al. Measurement of the running of the electromagnetic coupling at large momentum-transfer at LEP. *Phys. Lett. B*, 623:26–36, 2005.
- [13] P.A. Zyla et al. Review of Particle Physics. *PTEP*, 2020(8):083C01, 2020.

-
- [14] Nicola Cabibbo. Unitarity, symmetry and leptonic decays (Reprinted from *Phys Rev Lett*, vol 10, pg 531, 1963). *La Rivista del Nuovo Cimento*, 34:749–751, 01 2011.
- [15] Makoto Kobayashi and Toshihide Maskawa. CP-Violation in the Renormalizable Theory of Weak Interaction. *Progress of Theoretical Physics*, 49(2):652–657, 02 1973.
- [16] Peter W. Higgs. Broken Symmetries and the Masses of Gauge Bosons. *Phys. Rev. Lett.*, 13:508–509, Oct 1964.
- [17] F. Englert and R. Brout. Broken Symmetry and the Mass of Gauge Vector Mesons. *Phys. Rev. Lett.*, 13:321–323, Aug 1964.
- [18] John Ellis. Higgs Physics. pages 117–168. 52 p, Dec 2013. 52 pages, 45 figures, Lectures presented at the ESHEP 2013 School of High-Energy Physics, to appear as part of the proceedings in a CERN Yellow Report.
- [19] The CMS Collaboration. Combined measurements of Higgs boson couplings in proton–proton collisions at $\sqrt{s} = 13$ TeV. *The European Physical Journal C*, 79(5), May 2019.
- [20] The CMS Collaboration. Search for $t\bar{t}H$ production in the $H \rightarrow b\bar{b}$ decay channel with leptonic $t\bar{t}$ decays in proton-proton collisions at $\sqrt{s} = 13$ TeV. *JHEP*, 03:026, 2019.
- [21] The CMS Collaboration. Search for $t\bar{t}H$ production in the all-jet final state in proton-proton collisions at $\sqrt{s} = 13$ TeV. *Journal of High Energy Physics*, 2018(6), Jun 2018.
- [22] The CMS Collaboration. Evidence for associated production of a Higgs boson with a top quark pair in final states with electrons, muons, and hadronically decaying τ leptons at $\sqrt{s} = 13$ TeV. *Journal of High Energy Physics*, 2018(8), Aug 2018.
- [23] The CMS Collaboration. Evidence for the Higgs boson decay to a bottom quark–antiquark pair. *Physics Letters B*, 780:501–532, May 2018.
- [24] The CMS Collaboration. Observation of the Higgs boson decay to a pair of τ leptons with the CMS detector. *Physics Letters B*, 779:283–316, Apr 2018.
- [25] The CMS Collaboration. Search for the Higgs Boson Decaying to Two Muons in Proton-Proton Collisions at $\sqrt{s} = 13$ TeV. *Physical Review Letters*, 122(2), Jan 2019.

- [26] The CMS Collaboration. Measurements of properties of the Higgs boson decaying to a W boson pair in pp collisions at $\sqrt{s} = 13$ TeV. *Phys. Lett. B*, 791:96, 2019.
- [27] The CMS Collaboration. Measurements of properties of the Higgs boson decaying into the four-lepton final state in pp collisions at $\sqrt{s} = 13$ TeV. *JHEP*, 11:047, 2017.
- [28] E. D. Bloom, D. H. Coward, H. DeStaebler, J. Drees, G. Miller, L. W. Mo, R. E. Taylor, M. Breidenbach, J. I. Friedman, G. C. Hartmann, and H. W. Kendall. High-Energy Inelastic $e - p$ Scattering at 6° and 10° . *Phys. Rev. Lett.*, 23:930–934, Oct 1969.
- [29] David J. Gross and Frank Wilczek. Ultraviolet Behavior of Non-Abelian Gauge Theories. *Phys. Rev. Lett.*, 30:1343–1346, Jun 1973.
- [30] F.J. Hasert et al. Observation of neutrino-like interactions without muon or electron in the gargamelle neutrino experiment. *Physics Letters B*, 46(1):138–140, 1973.
- [31] G. Arnison et al. Experimental observation of lepton pairs of invariant mass around 95 GeV/c² at the CERN SPS collider. *Physics Letters B*, 126(5):398–410, 1983.
- [32] P. Bagnaia, M. Banner, R. Battiston, Ph. Bloch, F. Bonaudi, K. Borer, M. Borghini, J.-C. Chollet, A.G. Clark, C. Conta, P. Darriulat, L. Di Lella, and J. Dines-Hansen et al. Evidence for $Z^0 \rightarrow e^+e^-$ at the CERN pp collider. *Physics Letters B*, 129(1):130–140, 1983.
- [33] F. Abe, H. Akimoto, A. Akopian, M. G. Albrow, S. R. Amendolia, D. Amidei, J. Antos, C. Anway-Wiese, S. Aota, G. Apollinari, and et al. Observation of Top Quark Production in p^-p Collisions with the Collider Detector at Fermilab. *Physical Review Letters*, 74(14):2626–2631, Apr 1995.
- [34] S. Abachi, B. Abbott, M. Abolins, B. S. Acharya, I. Adam, D. L. Adams, M. Adams, S. Ahn, H. Aihara, J. Alitti, and et al. Observation of the Top Quark. *Physical Review Letters*, 74(14):2632–2637, Apr 1995.
- [35] The ATLAS Collaboration. Measurement of the $t\bar{t}$ production cross-section in the lepton+jets channel at $\sqrt{s} = 13$ TeV with the ATLAS experiment. *Phys. Lett. B*, 810:135797, 2020.
- [36] The CMS Collaboration. Measurement of differential $t\bar{t}$ production cross sections in the full kinematic range using lepton+jets events from proton-proton collisions at $\sqrt{s} = 13$ TeV. 8 2021.
- [37] Stefano Catani, Simone Devoto, Massimiliano Grazzini, Stefan Kallweit, Javier Mazzitelli, and Hayk Sargsyan. Top-quark pair hadroproduction at next-to-next-to-leading order in QCD. *Phys. Rev. D*, 99(5):051501, 2019.

-
- [38] Nazar Bartosik. $t\bar{t}$ decay channels. https://commons.wikimedia.org/wiki/File:Ttbar_decay_channels.png. Licensed under Creative Commons Attribution 4.0 International (CC BY 4.0), Accessed Nov. 2021.
- [39] The CMS Collaboration. Measurement of the inclusive and differential $t\bar{t}\gamma$ cross sections in the dilepton channel and effective field theory interpretation in proton-proton collisions at $\sqrt{s} = 13$ TeV. *JHEP*, 05:091, 2022.
- [40] The ATLAS Collaboration. Measurements of inclusive and differential fiducial cross-sections of $t\bar{t}\gamma$ production in leptonic final states at $\sqrt{s} = 13$ TeV in ATLAS. *Eur. Phys. J. C*, 79(5):382, 2019.
- [41] The CMS Collaboration. Measurement of the cross section for top quark pair production in association with a W or Z boson in proton-proton collisions at $\sqrt{s} = 13$ TeV. *Journal of High Energy Physics*, 2018(8), Aug 2018.
- [42] The ATLAS Collaboration. Measurement of the $t\bar{t}Z$ and $t\bar{t}W$ cross sections in proton-proton collisions at $\sqrt{s} = 13$ TeV with the ATLAS detector. *Physical Review D*, 99(7), Apr 2019.
- [43] The CMS Collaboration. Measurement of top quark pair production in association with a Z boson in proton-proton collisions at $\sqrt{s} = 13$ TeV. *Journal of High Energy Physics*, 2020(3), Mar 2020.
- [44] The ATLAS Collaboration. Measurements of the inclusive and differential production cross sections of a top-quark-antiquark pair in association with a Z boson at $\sqrt{s} = 13$ TeV with the ATLAS detector. *Eur. Phys. J. C*, 81:737, 2021.
- [45] The CMS Collaboration. Probing effective field theory operators in the associated production of top quarks with a Z boson in multilepton final states at $\sqrt{s} = 13$ TeV. *JHEP*, 12:083, 2021.
- [46] Achilleas Lazopoulos, Thomas McElmurry, Kirill Melnikov, and Frank Petriello. Next-to-leading order QCD corrections to $t\bar{t}Z$ production at the LHC. *Phys. Lett. B*, 666:62–65, 2008.
- [47] Achilleas Lazopoulos, Kirill Melnikov, and Frank John Petriello. NLO QCD corrections to the production of $t\bar{t}Z$ in gluon fusion. *Phys. Rev. D*, 77:034021, 2008.
- [48] Adam Kardos, Zoltan Trocsanyi, and Costas Papadopoulos. Top quark pair production in association with a Z-boson at NLO accuracy. *Phys. Rev. D*, 85:054015, 2012.

-
- [49] M. V. Garzelli, A. Kardos, C. G. Papadopoulos, and Z. Trocsanyi. $t\bar{t}W^{+-}$ and $t\bar{t}Z$ Hadroproduction at NLO accuracy in QCD with Parton Shower and Hadronization effects. *JHEP*, 11:056, 2012.
- [50] S. Frixione, V. Hirschi, D. Pagani, H. S. Shao, and M. Zaro. Electroweak and QCD corrections to top-pair hadroproduction in association with heavy bosons. *JHEP*, 06:184, 2015.
- [51] Anna Kulesza, Leszek Motyka, Daniel Schwartländer, Tomasz Stebel, and Vincent Theeuwes. Associated top quark pair production with a heavy boson: differential cross sections at NLO + NNLL accuracy. *The European Physical Journal C*, 80(5), May 2020.
- [52] Raoul Röntsch and Markus Schulze. Probing top-Z dipole moments at the LHC and ILC. *Journal of High Energy Physics*, 2015(8), Aug 2015.
- [53] Ewa Lopienska. The CERN accelerator complex, layout in 2022. Complexe des accélérateurs du CERN en janvier 2022. Feb 2022. General Photo.
- [54] The ATLAS Collaboration. The ATLAS Experiment at the CERN Large Hadron Collider. *Journal of Instrumentation*, 3(08):S08003–S08003, aug 2008.
- [55] The CMS Collaboration. The CMS Experiment at the CERN LHC. *JINST*, 3:S08004, 2008.
- [56] The ALICE Collaboration. The ALICE experiment at the CERN LHC. *Journal of Instrumentation*, 3(08):S08002–S08002, aug 2008.
- [57] The LHCb Collaboration. The LHCb Detector at the LHC. *Journal of Instrumentation*, 3(08):S08005–S08005, aug 2008.
- [58] Jean-Luc Caron. Cross section of LHC dipole. Dipole LHC: coupe transversale. AC Collection. Legacy of AC. Pictures from 1992 to 2002., May 1998.
- [59] Jean-Luc Caron. Magnetic field induced by the LHC dipole’s superconducting coils. Champ magnetique cree par les bobines superconductrices des aimants dipolaires du LHC. AC Collection. Legacy of AC. Pictures from 1992 to 2002., Mar 1998.
- [60] H Burkhardt and P Grafström. Absolute Luminosity from Machine Parameters. Technical report, 2007.
- [61] Lyndon R Evans and Philip Bryant. LHC Machine. *JINST*, 3:S08001. 164 p, 2008. This report is an abridged version of the LHC Design Report (CERN-2004-003).

-
- [62] J. T. Boyd. LHC Run-2 and Future Prospects. In *2019 European School of High-Energy Physics*, 1 2020.
- [63] The CMS Collaboration. Public luminosity results. <https://twiki.cern.ch/twiki/bin/view/{CMS}Public/LumiPublicResults>. Accessed: Jun. 2021.
- [64] S van der Meer. Calibration of the effective beam height in the ISR. Technical report, CERN, Geneva, 1968.
- [65] Joscha Knolle. *Measuring luminosity and the $t\bar{t}Z$ production cross section with the CMS experiment*. Dissertation, Universität Hamburg, Hamburg, 2020. Dissertation, Universität Hamburg, 2020.
- [66] CMS BRIL group. VdM Framework. <https://gitlab.cern.ch/bril/VdMFramework>.
- [67] The CMS Collaboration. *CMS Physics: Technical Design Report Volume 1: Detector Performance and Software*. Technical design report. CMS. CERN, Geneva, 2006.
- [68] David Barney. CMS Detector Slice. CMS Collection., Jan 2016.
- [69] A Dominguez et al. CMS Technical Design Report for the Pixel Detector Upgrade. Technical report, Sep 2012.
- [70] A Benaglia. The CMS ECAL performance with examples. *Journal of Instrumentation*, 9(02):C02008–C02008, feb 2014.
- [71] The CMS Collaboration. Performance of the CMS muon detector and muon reconstruction with proton-proton collisions at $\sqrt{s} = 13$ TeV. *Journal of Instrumentation*, 13(06):P06015–P06015, Jun 2018.
- [72] The CMS Collaboration. The CMS trigger system. *JINST*, 12(01):P01020, 2017.
- [73] A Tapper and Darin Acosta. CMS Technical Design Report for the Level-1 Trigger Upgrade. Technical report, Jun 2013. Additional contacts: Jeffrey Spalding, Fermilab, Jeffrey.Spalding@cern.ch Didier Contardo, Universite Claude Bernard-Lyon I, didier.claude.contardo@cern.ch.
- [74] Tai Sakuma. Cutaway diagrams of CMS detector. May 2019.
- [75] The CMS Collaboration. The Phase-2 Upgrade of the CMS Beam Radiation, Instrumentation, and Luminosity Detectors: Conceptual Design. Technical report, CERN, Geneva, Jan 2020.

-
- [76] The CMS Collaboration. Precision luminosity measurement in proton-proton collisions at $\sqrt{s} = 13$ TeV in 2015 and 2016 at CMS. *Eur. Phys. J. C*, 81(9):800, 2021.
- [77] Absolute Calibration of the Luminosity Measurement at CMS: Winter 2012 Update. Technical report, CERN, Geneva, 2012.
- [78] Paul Lujan. Performance of the Pixel Luminosity Telescope for Luminosity Measurement at CMS during Run 2. In *Proceedings of The European Physical Society Conference on High Energy Physics — PoS(EPS-HEP2017)*, volume 314, page 504, 2017.
- [79] Moritz Guthoff. The new Fast Beam Condition Monitor using poly-crystalline diamond sensors for luminosity measurement at CMS. *Nuclear Instruments and Methods in Physics Research Section A: Accelerators, Spectrometers, Detectors and Associated Equipment*, 936:717–718, 2019. Frontier Detectors for Frontier Physics: 14th Pisa Meeting on Advanced Detectors.
- [80] The CMS Collaboration. Description and performance of track and primary-vertex reconstruction with the CMS tracker. *Journal of Instrumentation*, 9(10):P10009–P10009, Oct 2014.
- [81] Pierre Billoir. Progressive track recognition with a Kalman-like fitting procedure. *Computer Physics Communications*, 57(1):390–394, 1989.
- [82] Muon tracking performance in the CMS Run-2 Legacy data using the tag-and-probe technique. Jul 2020.
- [83] R Frühwirth, Wolfgang Waltenberger, and Pascal Vanlaer. Adaptive Vertex Fitting. Technical report, CERN, Geneva, Mar 2007.
- [84] Jet algorithms performance in 13 TeV data. Technical report, CERN, Geneva, 2017.
- [85] The CMS Collaboration. Particle-flow reconstruction and global event description with the CMS detector. *Journal of Instrumentation*, 12(10):P10003–P10003, Oct 2017.
- [86] Matteo Cacciari, Gavin P Salam, and Gregory Soyez. The anti- k_t jet clustering algorithm. *JHEP*, 04(arXiv:0802.1189. LPTHE-07-03):063. 12 p, Feb 2008.
- [87] Gavin P Salam and Grégory Soyez. A practical seedless infrared-safe cone jet algorithm. *Journal of High Energy Physics*, 2007(05):086–086, May 2007.
- [88] Pileup Removal Algorithms. Technical report, CERN, Geneva, 2014.

-
- [89] The CMS Collaboration. Jet energy scale and resolution in the CMS experiment in pp collisions at 8 TeV. *Journal of Instrumentation*, 12(02):P02014–P02014, Feb 2017.
- [90] Emil Bols, Jan Kieseler, Mauro Verzetti, Markus Stoye, and Anna Stakia. Jet Flavour Classification Using DeepJet. *JINST*, 15(12):P12012, 2020.
- [91] The CMS Collaboration. Algorithms for b Jet identification in CMS. Technical report, CERN, Geneva, Jul 2009.
- [92] The CMS Collaboration. Identification of heavy-flavour jets with the CMS detector in pp collisions at 13 TeV. *Journal of Instrumentation*, 13(05):P05011–P05011, May 2018.
- [93] Steven Schramm. Searches for new physics using jet substructure in ATLAS and CMS. Technical report, CERN, Geneva, Nov 2018.
- [94] Daniele Bertolini, Philip Harris, Matthew Low, and Nhan Tran. Pileup per particle identification. *Journal of High Energy Physics*, 2014(10), Oct 2014.
- [95] Jesse Thaler and Ken Van Tilburg. Identifying Boosted Objects with N-subjettiness. *JHEP*, 03:015, 2011.
- [96] Machine learning-based identification of highly Lorentz-boosted hadronically decaying particles at the CMS experiment. Technical report, CERN, Geneva, 2019.
- [97] Identification of double-b quark jets in boosted event topologies. Technical report, CERN, Geneva, 2016.
- [98] Huilin Qu and Loukas Gouskos. Jet tagging via particle clouds. *Physical Review D*, 101(5), Mar 2020.
- [99] The CMS Collaboration. Identification of heavy, energetic, hadronically decaying particles using machine-learning techniques. *JINST*, 15(06):P06005, 2020.
- [100] Identification of highly Lorentz-boosted heavy particles using graph neural networks and new mass decorrelation techniques. Jan 2020.
- [101] Performance of electron and photon reconstruction in Run 2 with the CMS experiment. Jul 2020.
- [102] The CMS Collaboration. Electron and photon reconstruction and identification with the CMS experiment at the CERN LHC, 2020.
- [103] Muon identification and isolation efficiencies with 2017 and 2018 data. Jul 2018.

-
- [104] John Ellis, J.S. Hagelin, D.V. Nanopoulos, K. Olive, and M. Srednicki. Supersymmetric relics from the big bang. *Nuclear Physics B*, 238(2):453–476, 1984.
- [105] The CMS Collaboration. Performance of missing transverse momentum reconstruction in proton-proton collisions at $\sqrt{s} = 13$ TeV using the CMS detector. *JINST*, 14(07):P07004, 2019.
- [106] Torbjörn Sjöstrand, Stephen Mrenna, and Peter Skands. PYTHIA 6.4 physics and manual. *Journal of High Energy Physics*, 2006(05):524, May 2006.
- [107] Geoffrey C. Fox and Stephen Wolfram. Event shapes in $e+e-$ annihilation. *Nuclear Physics B*, 149(3):413–496, 1979.
- [108] The CMS Collaboration. Upcoming BCM1F paper. 2023.
- [109] Olena Karacheban and Yusuf Can Cekmecelioglu. Emittance Scans for CMS Luminosity Calibration in Run 2. *PoS*, EPS-HEP2019:193, 2020.
- [110] Moritz Guthoff. Overview of CMS luminosity-determination methodology in Run-2. Technical report, CERN, Geneva, Oct 2019.
- [111] The ATLAS Collaboration. Measurement of the $t\bar{t}W$ and $t\bar{t}Z$ production cross sections in pp collisions at $\sqrt{s} = 8$ TeV with the ATLAS detector. *Journal of High Energy Physics*, 2015(11), Nov 2015.
- [112] The CMS Collaboration. Observation of top quark pairs produced in association with a vector boson in pp collisions at $\sqrt{s} = 8$ TeV. *Journal of High Energy Physics*, 2016(1), Jan 2016.
- [113] D. de Florian et al. Handbook of LHC Higgs Cross Sections: 4. Deciphering the Nature of the Higgs Sector. 2/2017, 10 2016.
- [114] The CMS Collaboration. CMS luminosity measurement for the 2017 data-taking period at $\sqrt{s} = 13$ TeV. 2018.
- [115] The CMS Collaboration. CMS luminosity measurement for the 2018 data-taking period at $\sqrt{s} = 13$ TeV. 2019.
- [116] The CMS Collaboration. Precise determination of the mass of the Higgs boson and tests of compatibility of its couplings with the standard model predictions using proton collisions at 7 and 8 TeV. *Eur. Phys. J. C*, 75(5):212, 2015.
- [117] Glen Cowan, Kyle Cranmer, Eilam Gross, and Ofer Vitells. Asymptotic formulae for likelihood-based tests of new physics. *The European Physical Journal C*, 71(2), Feb 2011.

-
- [118] Roger Barlow and Christine Beeston. Fitting using finite Monte Carlo samples. *Computer Physics Communications*, 77(2):219–228, 1993.
- [119] J. S. Conway. Incorporating Nuisance Parameters in Likelihoods for Multisource Spectra, 2011.
- [120] The CMS Collaboration. Performance of the CMS muon detector and muon reconstruction with proton-proton collisions at $\sqrt{s} = 13$ TeV. *Journal of Instrumentation*, 13(06):P06015–P06015, Jun 2018.
- [121] Andrew J. Larkoski, Simone Marzani, Gregory Soyez, and Jesse Thaler. Soft Drop. *JHEP*, 05:146, 2014.
- [122] J. Alwall, R. Frederix, S. Frixione, V. Hirschi, F. Maltoni, O. Mattelaer, H. S. Shao, T. Stelzer, P. Torrielli, and M. Zaro. The automated computation of tree-level and next-to-leading order differential cross sections, and their matching to parton shower simulations. *JHEP*, 07:079, 2014.
- [123] Torbjorn Sjöstrand et al. An Introduction to PYTHIA 8.2. *Comput. Phys. Commun.*, 191:159–177, 2015.
- [124] S. Agostinelli et al. GEANT4: A Simulation toolkit. *Nucl. Instrum. Meth.*, A506:250, 2003.
- [125] Paolo Nason. A New method for combining NLO QCD with shower Monte Carlo algorithms. *JHEP*, 11:040, 2004.
- [126] Stefano Frixione, Paolo Nason, and Carlo Oleari. Matching NLO QCD computations with Parton Shower simulations: the POWHEG method. *JHEP*, 11:070, 2007.
- [127] Simone Alioli, Paolo Nason, Carlo Oleari, and Emanuele Re. A general framework for implementing NLO calculations in shower Monte Carlo programs: the POWHEG BOX. *JHEP*, 06:043, 2010.
- [128] The CMS Collaboration. Measurement of the Higgs boson production rate in association with top quarks in final states with electrons, muons, and hadronically decaying tau leptons at $\sqrt{s} = 13$ TeV. *Eur. Phys. J. C*, 81(4):378, 2021.
- [129] The ATLAS Collaboration. Observation of Higgs boson production in association with a top quark pair at the LHC with the ATLAS detector. *Phys. Lett. B*, 784:173–191, 2018.
- [130] The ATLAS Collaboration. Measurement of Higgs boson decay into b -quarks in associated production with a top-quark pair in pp collisions at $\sqrt{s} = 13$ TeV with the ATLAS detector. 11 2021.

-
- [131] Measurement of the inclusive and differential $t\bar{t}\gamma$ cross section and EFT interpretation in the dilepton channel at $\sqrt{s} = 13$ TeV. 2021.
- [132] The CMS Collaboration. Measurement of the inclusive and differential $t\bar{t}\gamma$ cross sections in the single-lepton channel and EFT interpretation at $\sqrt{s} = 13$ TeV. *JHEP*, 12:180, 2021.
- [133] The CMS Collaboration. Measurement of the differential Drell-Yan cross section in proton-proton collisions at $\sqrt{s} = 13$ TeV. *JHEP*, 12:059, 2019.
- [134] The CMS Collaboration. Measurement of differential cross sections and charge ratios for t-channel single top quark production in proton-proton collisions at $\sqrt{s} = 13$ TeV. *Eur. Phys. J. C*, 80(5):370, 2020.
- [135] The CMS Collaboration. Observation of tW production in the single-lepton channel in pp collisions at $\sqrt{s} = 13$ TeV. *JHEP*, 11:111, 2021.
- [136] The CMS Collaboration. W^+W^- boson pair production in proton-proton collisions at $\sqrt{s} = 13$ TeV. *Phys. Rev. D*, 102(9):092001, 2020.
- [137] The CMS Collaboration. Measurement of the inclusive and differential WZ production cross sections, polarization angles, and triple gauge couplings in pp collisions at $\sqrt{s} = 13$ TeV. 10 2021.
- [138] The CMS Collaboration. Measurements of $pp \rightarrow ZZ$ production cross sections and constraints on anomalous triple gauge couplings at $\sqrt{s} = 13$ TeV. *Eur. Phys. J. C*, 81(3):200, 2021.
- [139] Martín Abadi, Ashish Agarwal, Paul Barham, Eugene Brevdo, Zhifeng Chen, Craig Citro, Greg S. Corrado, Andy Davis, Jeffrey Dean, Matthieu Devin, Sanjay Ghemawat, Ian Goodfellow, Andrew Harp, Geoffrey Irving, Michael Isard, Yangqing Jia, Rafal Jozefowicz, Lukasz Kaiser, Manjunath Kudlur, Josh Levenberg, Dandelion Mané, Rajat Monga, Sherry Moore, Derek Murray, Chris Olah, Mike Schuster, Jonathon Shlens, Benoit Steiner, Ilya Sutskever, Kunal Talwar, Paul Tucker, Vincent Vanhoucke, Vijay Vasudevan, Fernanda Viégas, Oriol Vinyals, Pete Warden, Martin Wattenberg, Martin Wicke, Yuan Yu, and Xiaoqiang Zheng. TensorFlow: Large-Scale Machine Learning on Heterogeneous Systems, 2015. Software available from tensorflow.org.
- [140] Francois Chollet et al. Keras, 2015.
- [141] Christopher M. Bishop. *Pattern Recognition and Machine Learning (Information Science and Statistics)*. Springer-Verlag, Berlin, Heidelberg, 2006.

-
- [142] Diederik P. Kingma and Jimmy Ba. Adam: A Method for Stochastic Optimization, 2017.
- [143] MultiLayerNeuralNetwork. https://commons.wikimedia.org/wiki/File:MultiLayerNeuralNetworkBigger_english.png. Licenced under Creative Commons Attribution-Share Alike 3.0 Unported, Accessed Feb. 2022.
- [144] Ian Goodfellow, Yoshua Bengio, and Aaron Courville. *Deep Learning*. MIT Press, 2016.
- [145] Scott Lundberg and Su-In Lee. A Unified Approach to Interpreting Model Predictions, 2017.
- [146] Scott M. Lundberg and Su-In Lee. Consistent feature attribution for tree ensembles, 2018.
- [147] TOP Systematic Uncertainties (Run2) . <https://twiki.cern.ch/twiki/bin/view/{CMS}/TopSystematics>. Accessed March 2022.
- [148] Jon Butterworth et al. PDF4LHC recommendations for LHC Run II. *J. Phys. G*, 43:023001, 2016.
- [149] Anna Kulesza, Leszek Motyka, Daniel Schwartländer, Tomasz Stebel, and Vincent Theeuwes. Associated top quark pair production with a heavy boson: differential cross sections at NLO + NNLL accuracy. *The European Physical Journal C*, 80(5), May 2020.
- [150] Jan van der Linden. Limit on $tt+Z$ production in the $Z \rightarrow b\bar{b}$ channel at the CMS experiment. Master's thesis, Karlsruhe Institute of Technology (KIT), 2019.
- [151] Search for new physics using top quark pairs produced in associated with a boosted Z or Higgs boson in effective field theory. 2022.